Scattering Resonances in the Extreme Quantum Limit

A thesis presented
by

Jesse Shines Hersch

to
The Department of Physics
in partial fulfillment of the requirements
for the degree of
Doctor of Philosophy
in the subject of

Physics

Harvard University
Cambridge, Massachusetts
August 1999

For my parents,
Steve and Janice

Abstract

This thesis addresses topics in low energy scattering in quantum mechanics, in particular, resonance phenomena. Hence the title: the phrase "extreme quantum limit" refers to the situation when the wavelengths of the particles in the system are larger than every other scale, so that the behavior is far into the quantum regime. A powerful tool in the problems of low energy scattering is the point scatterer model, and will be used extensively throughout the thesis. Therefore, we begin with a thorough introduction to this model in Chapter 2. As a first application of the point scatterer model, we will investigate the phenomenon of the proximity resonance, which is one example of strange quantum behavior appearing at low energy. Proximity resonances will be addressed theoretically in Chapter 3, and experimentally in Chapter 4. Threshold resonances, another type of low energy scattering resonance, are considered in Chapter 5, along with their connection to the Efimov and Thomas effects, and scattering in the presence of an external confining potential. Although the point scatterer model will serve us well in the work presented here, it does have its limitations. These limitations will be removed in Chapter 6, where we describe how to extend the model to include higher partial waves. In Chapter 7, we extend the model one step further, and illustrate how to treat vector wave scattering with the model. Finally, in Chapter 8 we will depart from the topic of low energy scattering and investigate the influence of diffraction on an open quantum mechanical system, again both experimentally and theoretically.

Acknowledgments

This thesis would not exist without the help of my advisor, Eric Heller. In 1997, with three years of experience in an experimental group already behind me, he gave me a chance to try my hand at theoretical physics. Had I not been given that chance, I am quite sure that I would have left physics altogether. Furthermore, he gave me the freedom to pursue my experimental tendencies, which resulted in two successful experimental demonstrations of theories presented in this thesis. Finally, I thoroughly enjoyed the countless discussions in his office and elsewhere, which were instrumental in shaping my understanding of quantum physics.

As a student in Rick's group, I have been blessed by being surrounded by a fabulous group of students and postdocs. I enjoyed countless late night discussions with Areez Mody, a student in Rick's group. Michael Haggerty, a postdoc, has been my teacher in semiclassical methods; the last chapter of this thesis is due to our collective work. I enjoyed many discussions about topics as varied as electromagnetism and the Hammond organ with Alex Barnett, also a student. For the first two years of my study in Rick's group, I shared an office with Adam Lupu-Sax, a former student, who taught me much about scattering theory in our time together. In addition, I wish to thank the numerous other past and present Heller group members for useful feedback on this and other work: Bill Bies, Jonathan Edwards, Greg Fiete, Allison Kalben, Natasha Lepore, Neepa Maitra, Scot Shaw, Manny Tannenbaum, Jiri Vanicek (students), Doron Cohen, Lev Kaplan, and Martin Naraschewski (postdocs).

Sarah Pohlen has been a good friend to me throughout my studies, and I consider myself lucky to include her in the circle of my closest friends.

This thesis certainly would not have been written without the undying love and support of my parents, Steve and Janice. At a very early age, they instilled and nurtured in me a natural curiosity about all things, which led me eventually to a Ph.D. in theoretical physics.

Citations to Previously Published Work

Parts of this thesis have been previously published:

- "Observation of Proximity Resonances in a Parallel-Plate Waveguide," J. S. Hersch and E. J. Heller, *Physical Review Letters* **81**, 3059 (1998).
- "Threshold Resonances in a Double Well System," J. S. Hersch and E. J. Heller, *Physics Letters A* **254**, 72 (1999).
- "Diffractive Orbits in an Open Microwave Billiard," J. S. Hersch, M. R. Haggerty, and E. J. Heller, submitted to *Physical Review Letters*.

Contents

List of Figures

List of Tables

Chapter 1

Introduction and Outline of the Thesis

1.1 Introduction

In recent years, a terrific amount of progress has been made in the trapping and manipulation of atoms. Clouds of atoms have been produced which are so cold and dense that the de Broglie wavelength of the atoms is often larger than every other scale in the system. In parallel with the experimental advances, theoretical work in the theory of ultra-cold atom interactions has advanced considerably in the last few years. This brings us to the primary topic of this thesis: the scattering of particles at extremely low energy, when the wavelengths of the interacting particles are longer than every other length scale in the system. In this limit, we are deep into the quantum mechanical regime where many strange properties can emerge, defying our classical intuition.

Throughout this thesis and without exception, we will use atomic units such that $\hbar = m = c = 1$.

1.2 Outline of the thesis

In Chapter 2, we will present a useful theory for modeling the scattering of particles at very long wavelengths, called the point scatterer model. This model is useful in that it reduces the integral equations of multiple scattering theory to matrix equations which can be easily solved numerically. This theory will be used in Chapters 3 and 5, and extended in Chapters 6 and 7. In addition, we explain in Chapter 2 why the delta function potential does not scatter in dimensions higher than one.

In Chapter 3, we will discuss the phenomenon of proximity resonances, which occur when two resonant scatterers are placed very close to one another. Here, “close” means that each scatterer is placed so that the on-resonance single scatterer s-wave cross sections overlap. Here we expect strange effects to occur: if the incident wave hits one scatterer, in some sense it cannot avoid hitting the other scatterer, since the cross sections are overlapping. This situation can lead to extremely long lived resonances.

In Chapter 4, we present experimental results on the scattering of electromagnetic waves by dielectric cylinders in a parallel-plate waveguide. These results are the first experimental observation of proximity resonances. Also presented is an efficient numerical method for solving the multiple scattering of two separated piecewise-constant potentials. The method may easily be extended to include more than two potentials.

In Chapter 5, we discuss another type of resonance that occurs at long wavelengths: the threshold resonance. Such a resonance occurs when a bound state of a system is released to the continuum as a parameter of the system is varied. When this release occurs, the bound state becomes a scattering resonance at zero energy. Hence the name “threshold” resonance.

In Chapter 6, we present a method for extending the point scatterer model to include higher partial waves. In the past, the model has been used to model only s-wave scattering. This has limited the energies to which the model may be applied to extremely low energies, where the wavelength of the scattering particle is much longer than every other scale. However, we know that as the energy increases, p- and higher partial-waves are scattered by the potential. Using the extension presented, we may treat with matrix methods the multiple scattering problem of any number of finite range potentials, properly including any number of scattered partial waves from each potential.

In Chapter 7, we extend the point scatterer model in a different direction, to treat the scattering of a *vector* wave by any number of dipole scatterers. This has application to the problem of light scattering by a dense cloud of atoms, such as are produced in atom traps. For resonant scatterers, we find proximity resonance-like features.

In Chapter 8, we depart from the main theme of the thesis to consider the role of diffraction in determining the spectrum and wavefunctions of an open quantum mechanical system. We present experimental results that, for the first time, show the effect of diffractive orbits on both the spectrum and the wavefunctions of an open system. A semiclassical theory for including diffractive orbits into the trace formula is described, and a comparison between an analogous closed system is made.

Chapter 2

Zero range potentials

2.1 Point scatterer model

The point scatterer model is very useful for studying the scattering of particles at low energy, when the wavelength is much larger than an other scale. This model will be used at various points throughout this thesis. Therefore, we begin by learning a bit about this model. Point scatterers are variously referred to in the literature as zero range potentials, point interactions, and regularized pseudopotentials. See, e.g. [4, 8, 22, 37].

The t-matrix for a potential V is defined by the operator equation,

$$T\phi = V\psi, \tag{2.1}$$

where ϕ is the wave incident on the scattering potential, and ψ is the full wave function, $\psi = \phi + \psi_s$. Here ψ_s is the scattered wave. If the t-matrix is known, this is equivalent to knowledge of the full wave function, as is obvious from the Lippmann-Schwinger equation:

$$\begin{aligned}
\psi(\boldsymbol{r}) &= \phi(\boldsymbol{r}) + \int d^3\boldsymbol{r}' G(\boldsymbol{r},\boldsymbol{r}')V(\boldsymbol{r}')\psi(\boldsymbol{r}') \\
&= \phi(\boldsymbol{r}) + \iint d^3\boldsymbol{r}' d^3\boldsymbol{r}'' G(\boldsymbol{r},\boldsymbol{r}')T(\boldsymbol{r}',\boldsymbol{r}'')\phi(\boldsymbol{r}'') \qquad (2.2)
\end{aligned}$$

Now, for a point scatterer, the t-matrix takes on the simple form,

$$t_i(k) = s(k)\left|\boldsymbol{r}_i\right\rangle\left\langle\boldsymbol{r}_i\right|, \tag{2.3}$$

where $s(k)$ is an energy dependent amplitude, and $\boldsymbol{r}_i$ is the location of the scatterer. The form of $s(k)$ is determined by the potential that we are interested in modeling, as we shall see below. In the position representation the t-matrix takes on the form,

$$t_i(\boldsymbol{r},\boldsymbol{r}') = s(k)\delta(\boldsymbol{r}_i - \boldsymbol{r})\delta(\boldsymbol{r}_i - \boldsymbol{r}'). \tag{2.4}$$

If we substitute this t-matrix into Eq. 2.2, we find,

$$\begin{aligned}\psi(\boldsymbol{r}) &= \phi(\boldsymbol{r}) + \iint d^3\boldsymbol{r}'d^3\boldsymbol{r}''G(\boldsymbol{r},\boldsymbol{r}')s(k)\delta(\boldsymbol{r}_i - \boldsymbol{r}')\delta(\boldsymbol{r}_i - \boldsymbol{r}'')\phi(\boldsymbol{r}'') \\ &= \phi(\boldsymbol{r}) + s(k)G(\boldsymbol{r},\boldsymbol{r}_i)\phi(\boldsymbol{r}_i). \end{aligned} \tag{2.5}$$

The integration has been trivially performed with the help of the delta functions. Now, the Green function appropriate with the asymptotic boundary condition on ψ is the outgoing Green function. Therefore we recognize the second term in Eq. 2.5 as the scattered wave, and it is apparent that the amplitude $s(k)$ will be related to the s-wave scattering amplitude $f(k)$. We can find this relationship, which depends on the space dimension, by substituting the appropriate outgoing Green function into Eq. 2.5 and taking the asymptotic limit, $r \gg r_i$, requiring correspondence with the boundary condition at infinity:

$$\psi(\boldsymbol{r}) \to \phi(\boldsymbol{r}) + e^{i(\boldsymbol{k}_0 - \boldsymbol{k})\cdot\boldsymbol{r}_i} f(k)\frac{e^{ikr}}{r^{(D-1)/2}}, \tag{2.6}$$

where $\boldsymbol{r}_i$ is the location of the scatterer, $\boldsymbol{k}_0$ is the wave vector in the direction of the incident wave, $\boldsymbol{k}$ is the wave vector in the direction of the scattered wave, and D is the space dimension (here 2 or 3). Note that the phase $e^{i\boldsymbol{k}_0 - \boldsymbol{k})\cdot\boldsymbol{r}_i}$ is not present if the scatterer is located at the origin, or if the incident direction is the same as the direction of observation. This is related to the fact that there is always a bright spot in the forward direction in X-ray crystallography. Forward scattered waves are *always* in phase with each other.

Let's determine the relationship between $s(k)$ and $f(k)$ for the case $D = 3$ first. For the outgoing Green function we have,

$$G(\boldsymbol{r},\boldsymbol{r}') = -\frac{1}{4\pi}\frac{e^{ik|\boldsymbol{r}-\boldsymbol{r}'|}}{|\boldsymbol{r}-\boldsymbol{r}'|}. \tag{2.7}$$

Substitution of this into Eq. 2.5 yields,

$$\begin{aligned}\psi(\boldsymbol{r}) &= \phi(\boldsymbol{r}) - \frac{s(k)}{4\pi}\frac{e^{ik|\boldsymbol{r}-\boldsymbol{r}_i|}}{|\boldsymbol{r}-\boldsymbol{r}_i|}\phi(\boldsymbol{r}_i) \\ &\to \phi(\boldsymbol{r}) - \frac{s(k)}{4\pi}e^{i(\boldsymbol{k}_0-\boldsymbol{k})\cdot\boldsymbol{r}_i}\frac{e^{ikr}}{r}, \end{aligned} \tag{2.8}$$

where we have taken $\phi(\boldsymbol{r}_i)$ to be a plane wave, $e^{i\boldsymbol{k}_0\cdot\boldsymbol{r}}$. Comparing Eq. 2.8 with Eq. 2.6 we find,

$$s(k) = -4\pi f(k). \tag{2.9}$$

In two dimensions, the procedure is identical. The outgoing Green function is,

$$G(\boldsymbol{r},\boldsymbol{r}') = -\frac{i}{4}H_0^{(1)}(k|\boldsymbol{r}-\boldsymbol{r}'|), \tag{2.10}$$

and we find,

$$s(k) = -\sqrt{8\pi k}\; e^{-i\pi/4} f(k). \tag{2.11}$$

Here the relation is dependent on energy, which is an artifact of the low energy divergence of the s-wave cross section in two dimensions.

So we see that, given a suitable $f(k)$, the point scatterer will exactly mimic the s-wave part of any finite range potential one might care to model. The real advantage, however, comes when we wish to calculate multiple scattering of many potentials, which may be identical or different.

2.2 Multiple scattering

Now imagine two or more non-overlapping, finite range potentials. How would we approach the scattering problem? The Lippmann-Schwinger equation Eq. 2.2 is still valid, but now the potential is different:

$$\begin{aligned}\psi(\boldsymbol{r}) &= \phi(\boldsymbol{r}) + \int d^3\boldsymbol{r}' G(\boldsymbol{r},\boldsymbol{r}')V(\boldsymbol{r}')\psi(\boldsymbol{r}') \\ &= \phi(\boldsymbol{r}) + \sum_i \int d^3\boldsymbol{r}' G(\boldsymbol{r},\boldsymbol{r}')V_i(\boldsymbol{r}')\psi(\boldsymbol{r}'). \end{aligned} \tag{2.12}$$

The potential V is now made up of a sum of potentials located at different positions $\{\boldsymbol{r}_i\}$. Eq. 2.12 would be very difficult to solve in practice. It is an integral equation with many integral terms! We can reduce the difficulty considerably by using point scatterer t-matrices. This step, however, truncates the exact potentials V_i, which scatter all partial waves in general, into potentials which only scatter s-waves[1]. Therefore we expect the following approximation to work only at sufficiently low energy of the incident particle. We rewrite the Lippmann-Schwinger equation with t-matrices as,

$$\begin{aligned}\psi(\boldsymbol{r}) &= \phi(\boldsymbol{r}) + \sum_i \iint d^3\boldsymbol{r}' d^3\boldsymbol{r}'' G(\boldsymbol{r},\boldsymbol{r}') s_i \delta(\boldsymbol{r}_i-\boldsymbol{r})\delta(\boldsymbol{r}_i-\boldsymbol{r}')\psi_i(\boldsymbol{r}'') \\ &= \phi(\boldsymbol{r}) + \sum_i s_i G(\boldsymbol{r},\boldsymbol{r}_i)\psi_i(\boldsymbol{r}_i). \end{aligned} \tag{2.13}$$

---

[1] In Chapter 6 we will show how the point scatterer model can be extended to include higher partial waves.

The $\psi_i(\boldsymbol{r})$ are defined by,

$$\psi_i(\boldsymbol{r}) = \phi(\boldsymbol{r}) + \sum_{j \neq i} s_j G(\boldsymbol{r}, \boldsymbol{r}_j) \psi_j(\boldsymbol{r}_j). \tag{2.14}$$

Let's pause and reflect on what this means. If there were only one scatterer, then $\psi_i(\boldsymbol{r})$ would just be the incident wave, $\phi(\boldsymbol{r})$. So $\psi_i(\boldsymbol{r})$ is something like an incident wave. Also included, however, are all the little "wavelets" scattered from all the other scatterers, $j \neq i$, which bounce around and eventually hit i. This is apparent in Eq. 2.14. So one can say that $\psi_i(\boldsymbol{r})$ is the wave incident on scatterer i in the presence of all the other scatterers. In fact, included in $\psi_i(\boldsymbol{r})$ are waves which hit i, leave, and at some time later come back and hit i again. The *only* part of the full solution not included in $\psi_i(\boldsymbol{r})$ is that which leaves the system of scatterers and *never* comes back to hit i.

We can evaluate Eq. 2.14 at $\boldsymbol{r}_i$ to obtain a matrix equation relating $\psi_i(\boldsymbol{r}_i)$ and $\phi(\boldsymbol{r}_i)$. This equation can be inverted for $\psi_i(\boldsymbol{r}_i)$, which is then substituted into Eq. 2.13, and we have the solution. In this way, point scatterer t-matrices reduce the complicated multiple scattering integral equation Eq. 2.12 to a matrix inversion problem. This method will be used in the next chapter for solving the scattering problem of two nearby s-wave scatterers.

2.3 Why delta functions do not scatter in $D > 1$ dimensions

One may well wonder what sort of potentials the t-matrices introduced in the previous sections represent. An obvious guess would be something like the Dirac delta function. This guess, however, is wrong. It turns out, that in dimensions higher than one, the delta function potential does not scatter *at all.* It is effectively invisible to incident waves of all energies. This has to do with the fact that the bound states of the delta function potential all have infinite binding energy; they are infinitely far from threshold and therefore do not couple to the $E > 0$ incident wave. This will be discussed in detail later in this chapter. At this point, we will show explicitly that the scattering phase shift approaches zero in the limit of a square well becoming a delta function, first for the three dimensional case, and then for two dimensions.

2.4 Disappearance of the s-wave phase shift: 3D case

The square well potential in 3D is defined by,

$$V(\boldsymbol{r}) = \begin{cases} -U & r < a \\ 0 & r > a \end{cases} \tag{2.15}$$

where U is the depth of the well and a is the well radius. To make a delta function potential, we will let $a \to 0$ and $U \to \infty$ such that,

$$\int V(\boldsymbol{r})\ d^3\boldsymbol{r} = -\xi = \text{constant}. \tag{2.16}$$

This implies,

$$U(a) = \frac{3\xi}{4\pi a^3}. \tag{2.17}$$

The s-wave phase shift for a 3D square well is given by (see, e.g. [5]),

$$\tan\delta_0 = \frac{ka\tan\kappa a - \kappa a\tan ka}{\kappa a + ka\tan ka\tan\kappa a}, \tag{2.18}$$

where $k = \sqrt{2E}$, $\kappa = \sqrt{2(E+U)}$, and E is the energy of the incident wave. We wish to investigate the behavior of this phase shift as $a \to 0$. We have,

$$ka = \sqrt{2E}\ a, \tag{2.19}$$

which vanishes with a, so that ka can be treated everywhere as a small quantity. For κa we have,

$$\begin{aligned} \kappa a &= \sqrt{2(E+U)}\ a \\ &= \sqrt{2\left(E + \frac{3\xi}{4\pi a^3}\right)}\ a \\ &\approx \sqrt{\frac{3\xi}{2\pi a}}. \end{aligned} \tag{2.20}$$

Substituting this approximation into the formula for the phase shift, we have,

$$\begin{aligned} \tan\delta_0 &\approx \frac{ka\tan\sqrt{\frac{3\xi}{2\pi a}} - \sqrt{\frac{3\xi}{2\pi a}}\tan ka}{\sqrt{\frac{3\xi}{2\pi a}} + ka\tan ka\tan\sqrt{\frac{3\xi}{2\pi a}}} \\ &\approx \frac{ka\tan\sqrt{\frac{3\xi}{2\pi a}} - ka\sqrt{\frac{3\xi}{2\pi a}}}{\sqrt{\frac{3\xi}{2\pi a}} + (ka)^2\tan\sqrt{\frac{3\xi}{2\pi a}}} \\ &\approx -ka. \end{aligned} \tag{2.21}$$

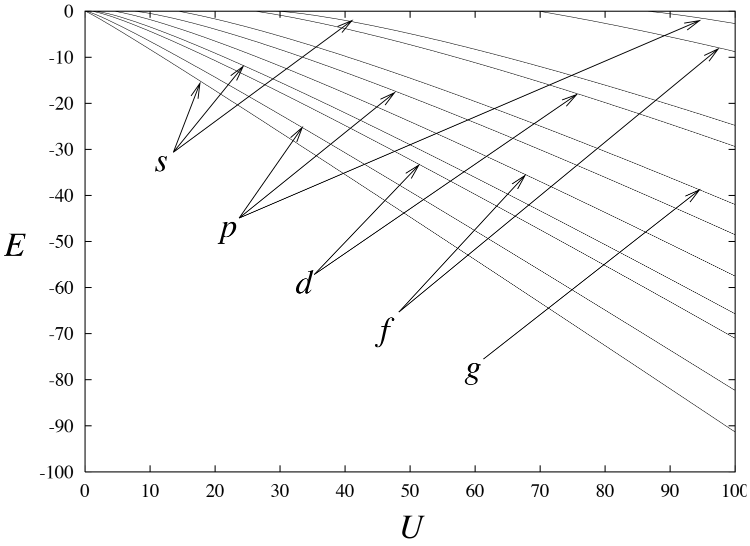

Figure 2.1: Bound states of a square well in three dimensions, as the delta function limit is taken. The depth U is taken to infinity as the range goes to zero in such a way that the volume of the well is a constant. Note that new levels appear as the limit is taken, and all the levels approach infinite binding energy as $U \to \infty$. Here we have taken $4\pi a^3 U/3 = \xi = 100$. The angular symmetries of each state are also indicated.

Thus we see that the phase shift, and therefore the cross section, goes to zero as $a \to 0$, even though the potential gets deeper as $1/a^3$. The question remains then, exactly what sort of potential *does* continue to scatter as the range tends to zero? One might guess that such a potential would have to be even *more* singular than a delta function, in the sense that the depth increases with some higher power of $1/a$. This intuition, however, is again incorrect. We shall show that the depth of the potential must actually vary as $1/a^2$ in order to keep the cross section fixed at low energy. This implies the strange but nevertheless true fact that the volume integral for such a potential is *zero*. Thus a collection of any number of such wells would have zero mean potential.

In Fig. 2.1, we plot the energy levels of a square well with $\xi = 100$ as the delta function limit is taken. It is apparent that the levels decrease in energy with the depth U. This means that all the levels will end up at infinite binding energy as $U \to \infty$. This points to an alternative explanation of why the delta function does not scatter in 3D. For low energy scattering, we know that the cross section is determined by the scattering length, α, which is inversely proportional to the square root of the energy of the closest s-wave bound

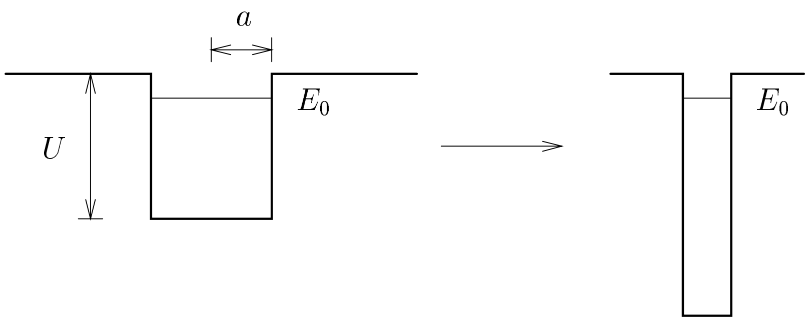

Figure 2.2: Limiting procedure for a square well such that the bound s-level remains at binding energy E_0 as the range of the potential approaches zero.

state to threshold, E_0:

$$\alpha = \frac{1}{\sqrt{2|E_0|}}. \tag{2.22}$$

Now, the delta function maintains all of its levels at infinite binding energy. This implies that the scattering length for such a potential is zero, and therefore does not scatter in the low energy limit. But for a zero range potential, *all* energies are effectively low energy, because the wavelength is always much larger than the range of the potential. Therefore there is no scattering at all energies. Note that many of the levels indicated in Fig. 2.1 are degenerate because of spherical symmetry. For instance, each p-level is 3-fold degenerate because we have $l = 1$, $m = 0, \pm 1$.

We will now find the limiting form of a zero range potential which possesses a single s-wave bound state at fixed binding energy $E_0 < 0$ below threshold. The limiting process is depicted in Fig. 2.2. This implies a s-wave cross section,

$$\sigma_0 = 4\pi\alpha^2, \tag{2.23}$$

with the scattering length given by,

$$\alpha = \frac{1}{\sqrt{2|E_0|}}. \tag{2.24}$$

The bound states of a spherical square well are given by,

$$\frac{k}{\kappa} k_l(\kappa a) j_l'(ka) = k_l'(\kappa a) j_l(ka), \tag{2.25}$$

where $j_l(x)$ is a spherical Bessel function, $k_l(x)$ is a modified spherical Bessel function, and

$$\begin{aligned} k &= \sqrt{2(E_0 + U)} \\ \kappa &= \sqrt{2|E_0|}. \end{aligned} \tag{2.26}$$

We are interested in the case of a bound s-level near threshold, so that $l = 0$ and $|E_0| \ll U$. For $l = 0$, the condition reduces to,

$$ka \cot ka = -\kappa a. \tag{2.27}$$

Now, since κa approaches zero from above in the zero range limit, we are looking for solutions of $ka \cot ka \to 0$ from below. Such solutions will be found near $ka = \pi/2$, So we expand the cotangent near this point and find,

$$\begin{aligned} -\kappa a &= ka \cot ka \\ &\approx ka \left(\frac{\pi}{2} - ka \right). \end{aligned} \tag{2.28}$$

We solve this quadratic equation for ka to find,

$$\begin{aligned} ka &= \frac{\pi}{4} \left(1 \pm \sqrt{1 + \frac{16\kappa a}{\pi}} \right) \\ &\approx \frac{\pi}{4} \left(1 + \left(1 + \frac{8\kappa a}{\pi} \right) \right) \\ &= \frac{\pi}{2} + \frac{2\kappa a}{\pi}, \end{aligned} \tag{2.29}$$

where we have taken the positive root because ka must remain finite as $a \to 0$. Now we can substitute Eqs. 2.26 to find the depth of the potential as a function of the radius:

$$U(a) = -E_0 + \frac{1}{2} \left(\frac{\pi}{2a} + \frac{\sqrt{8|E_0|}}{\pi} \right)^2. \tag{2.30}$$

This depth indeed goes as $1/a^2$ for small a, so that the volume integral of such a potential vanishes in the zero range limit.

2.5 Disappearance of the s-wave phase shift: 2D case

For the 2D case, we will consider the same potential as in the 3D case:

$$V(\boldsymbol{r}) = \begin{cases} -U & r < a \\ 0 & r > a \end{cases} \tag{2.31}$$

For a square well in 2D, the scattering s-wave phase shift is given by,

$$\tan \delta_0 = \frac{\kappa J_0(ka) J_0'(\kappa a) - k J_0'(ka) J_0(\kappa a)}{\kappa Y_0(ka) J_0'(\kappa a) - k Y_0'(ka) J_0(\kappa a)}, \tag{2.32}$$

where $J_0(x)$ is a zeroth order Bessel funcition, and $Y_0(x)$ is a zeroth order Neumann function. As in the 3D case, k and κ are defined by,

$$\begin{aligned} k &= \sqrt{2E}, \\ \kappa &= \sqrt{2(E+U)}. \end{aligned} \tag{2.33}$$

The delta function limit is defined by,

$$\int V(\boldsymbol{r})\ d^2\boldsymbol{r} = -\xi = \text{constant}, \tag{2.34}$$

which implies,

$$U(a) = \frac{\xi}{\pi a^2}. \tag{2.35}$$

As $a \to 0$, we find $ka \to 0$, whereas $\kappa a \to \sqrt{2\pi/\xi}$, a constant. Thus ka can be treated everywhere as a small quantity. We use the small argument expansions of the Bessel functions:

$$J_0(x) \approx 1 - \frac{x^2}{4} \tag{2.36}$$

$$Y_0(x) \approx \frac{2}{\pi}\left(\gamma + \ln\frac{x}{2}\right) \tag{2.37}$$

$$J_0'(x) = -J_1(x) \approx -\frac{x}{2} \tag{2.38}$$

$$Y_0'(x) = -Y_1(x) \approx -\frac{2}{\pi x} \tag{2.39}$$

where $\gamma = 0.5772\ldots$ is the Euler constant. Using these approximations, the s-wave phase shift becomes,

$$\begin{aligned} \tan\delta_0 &\approx \frac{\sqrt{\frac{2\pi}{\xi}}\left(1-\frac{(ka)^2}{4}\right)J_0'\left(\sqrt{\frac{2\pi}{\xi}}\right)+\frac{(ka)^2}{2}J_0\left(\sqrt{\frac{2\pi}{\xi}}\right)}{\sqrt{\frac{2\pi}{\xi}}J_0'\left(\sqrt{\frac{2\pi}{\xi}}\right)\left(\frac{2\gamma}{\pi}+\frac{2}{\pi}\ln(ka/2)\right)+\frac{2}{\pi}J_0\left(\sqrt{\frac{2\pi}{\xi}}\right)} \\ &\approx \frac{\pi}{2}\frac{1}{\ln(ka/2)}. \end{aligned} \tag{2.40}$$

Thus, for fixed wavenumber k, the s-wave phase shift for the 2D square well approaches zero as $1/\ln a$. One must be careful about the order of limits, however. If one first takes the low energy limit, $k \to 0$, then the s-wave cross section *diverges*, as can be seen from,

$$\sigma_0 = \frac{4}{k}\sin^2\delta_0 \tag{2.41}$$

$$\approx \frac{4}{k}\left(\frac{\pi}{2}\frac{1}{\ln(ka/2)}\right)^2. \tag{2.42}$$

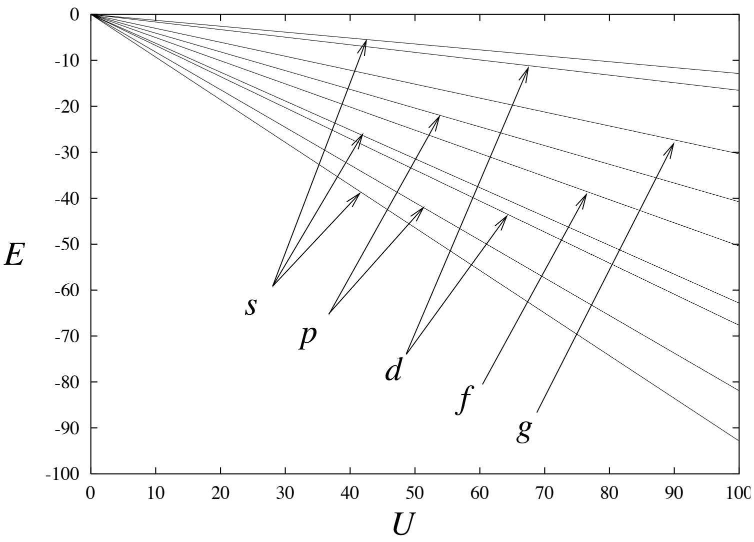

Figure 2.3: Bound states of a square well in two dimensions, as the delta function limit is taken. The depth U is taken to infinity as the range goes to zero in such a way that the volume of the well is constant. Unlike the 3D case, no new levels appear as the limit is taken. However, all the levels approach infinite binding energy as $U \to \infty$. Here we have taken $\pi a^2 U = \xi = 100$. The angular symmetries of each state are also indicated.

So, in taking the delta function limit in 2D, we understand that the energy must be held fixed, and then the range of the well is taken to zero. In this limit, the well ceases to scatter.

In Fig. 2.3 we plot the bound state energies of the square well in 2D, as the delta function limit is taken, with $\xi = 100$. The figure is analogous to Fig. 2.1. In this case, the number of levels stays *constant* as the limit is taken, in contrast to the 3D case, where the number of levels diverges. Other than this feature, the figures are similar. The levels all decrease in energy as the depth increases, so that in the limit all the levels will be infinitely bound. This offers an alternative, intuitive explanation of why the 2D delta function does not scatter: since all the levels are infinitely bound, they do not couple to the $E > 0$ incident wave.

This leads us to the question, what is the proper limit of a 2D well which *does* scatter as its range is taken to zero? Such a potential would possess a s-wave bound state near threshold which would not shift as the limit is taken, as in the 3D case. The s-wave bound states of the well are given by the characteristic equation,

$$kK_0(\kappa a)J_0'(ka) = \kappa K_0'(\kappa a)J_0(ka) \tag{2.43}$$

Where $K_0(x)$ is a zeroth order modified Bessel function. Referring again to Fig. 2.2, we have

$$\begin{aligned} k &= \sqrt{2(E_0 + U)} \\ \kappa &= \sqrt{2|E_0|}. \end{aligned} \tag{2.44}$$

The limiting forms of ka and κa are,

$$\kappa a = \sqrt{2a^2|E_0|} \to 0 \tag{2.45}$$

$$ka = \sqrt{2a^2(E_0 + U)} \to 0, \tag{2.46}$$

where we know that the last equation is true because U must approach infinity more slowly than $1/a^2$. We know this because in the delta function limit, which does not scatter, $U \sim 1/a^2$. Therefore, in the limit of a zero range potential that keeps the level structure near threshold fixed, the depth U must increase more slowly than $1/a^2$. Using the small argument forms for the Bessel functions, we find,

$$\frac{(ka)^2}{2} \approx -\frac{1}{\gamma + \ln(\kappa a/2)} \tag{2.47}$$

Now we use the expressions for ka, κa in Eq. 2.33 to find,

$$U(a) = -E_0 - \frac{1}{a^2\left(\gamma + \ln(\kappa a/2)\right)} \tag{2.48}$$

We see that the depth U approaches infinity only slightly slower than $1/a^2$. This slow singularity is enough, however, to keep the weakly bound s-level unchanged in energy as the limit is taken.

Chapter 3

Proximity Resonances: Theory

3.1 What is a proximity resonance?

Among the many interesting phenomena that appear in low energy scattering is the proximity resonance. As a tangible example, think of two air bubbles in water, of such a size that they resonantly scatter acoustic s-waves at a wavelength that is much larger than their diameter [14]. For air bubbles in water, such a condition is realized for bubbles of radius $r \sim 10^{-2}$ cm. For two such bubbles situated much closer than a wavelength, there will be two resonant modes, as shown in Fig 3.1.

For the s-wave mode, the bubbles grow and decrease in size *in phase.* Since they situated together much closer than a wavelength, the amplitude radiated away from the bubbles adds up nearly in phase everywhere in space. In particular, the amplitude far from

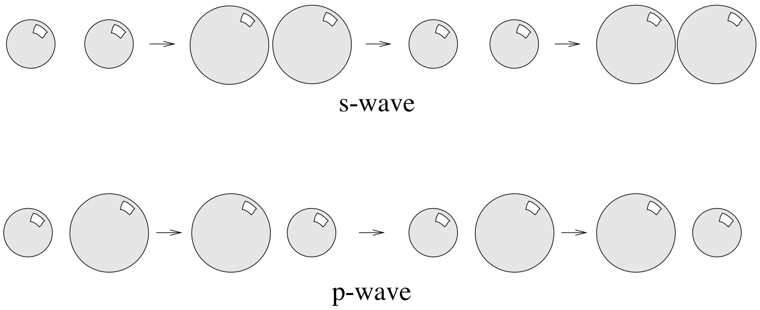

Figure 3.1: Two modes of resonant oscillation for nearby air bubbles in water. The figure is meant to represent a sequence of snapshots of the bubbles over 1.5 periods of oscillation, with time increasing from the left to right.

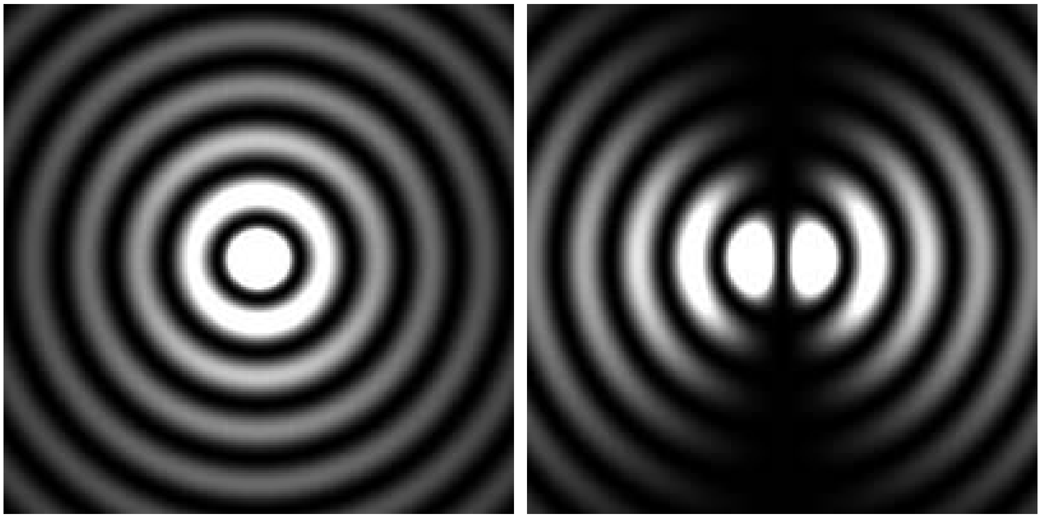

Figure 3.2: The addition of two nearby Bessel functions. In each plot, there are two point sources of amplitude placed $\lambda/2\pi$ apart from each other. On the left, the sources are in phase, and on the right, they are exactly out of phase. The intensity for the p-wave pattern has been multiplied by a factor of 10.

the bubbles will be appreciable. On the other hand, when the p-wave mode is excited, amplitude will combine *destructively* nearly everywhere in space, and the amplitude far from the bubbles will be much reduced from the s-wave case. This idea is demonstrated in Fig. 3.2. We have plotted in two dimensions the intensity of a wave emanating from two point sources, placed a distance $\lambda/2\pi$ apart. When the sources are in phase, the total wave intensity is difficult to distinguish from a pure s-wave source. However, when the two sources are out of phase, the intensity far away is decreased by a factor of 10 because of destructive interference. This interference effect can lead to extremely long lived resonances, as we shall see.

What does this mean for a scattering resonance? We know that the width of the resonance is proportional to the rate at which amplitude escapes from the neighborhood of the scattering system. This rate is proportional to the ratio $|\psi_{\text{far}}/\psi_{\text{near}}|^2$, where ψ_{far} is the far field amplitude and ψ_{near} is the amplitude in the near field. This ratio will remain finite for the in-phase pair of scatterers, and vanish for the out of phase pair, as their separation goes to zero. In this way, the proximity resonance can become extremely narrow as the scatterers are brought close together.

3.2 Proximity resonance: 3D case

We now turn to the problem of two nearby point scatterers. The partial wave expansion for the scattering amplitude of the combined pair will be derived, first in three dimensions, and then in two. The picture to keep in mind is two resonant point scatterers a distance d apart, positioned on the z-axis. The incident wave ϕ is a plane wave with wave vector $\boldsymbol{k}$ that makes an angle θ with the z-axis.

The approach will be the following. Using the single scatterer t-matrix for a point scatterer and the free Green function, we will find an expression for the full scattered wave function $\psi(\boldsymbol{r})$ for two scatterers a distance d apart. From this we will extract the scattering amplitude $F(\theta)$ and then perform a partial wave expansion. This approach will be followed for both the two and three dimensional cases.

As shown in Sec. 2.2, the solution to the multiple scattering problem of a collection of point scatterers is given by,

$$\begin{aligned}\psi(\boldsymbol{r}) &= \phi(\boldsymbol{r}) + \sum_i \iint d^3\boldsymbol{r}' d^3\boldsymbol{r}'' G(\boldsymbol{r},\boldsymbol{r}') s_i \delta(\boldsymbol{r}_i - \boldsymbol{r})\delta(\boldsymbol{r}_i - \boldsymbol{r}')\psi_i(\boldsymbol{r}'') \\ &= \phi(\boldsymbol{r}) + \sum_i s_i G(\boldsymbol{r},\boldsymbol{r}_i)\psi_i(\boldsymbol{r}_i), \qquad (3.1)\end{aligned}$$

and,

$$\psi_i(\boldsymbol{r}) = \phi(\boldsymbol{r}) + \sum_{j\neq i} s_j G(\boldsymbol{r},\boldsymbol{r}_j)\psi_j(\boldsymbol{r}_j). \qquad (3.2)$$

Now let's focus on just two scatterers. Eq. 3.2 becomes,

$$\begin{aligned}\psi_1(\boldsymbol{r}) &= \phi(\boldsymbol{r}) + G(\boldsymbol{r},\boldsymbol{r}_2)s_2\psi_2(\boldsymbol{r}_2) \qquad (3.3)\\ \psi_2(\boldsymbol{r}) &= \phi(\boldsymbol{r}) + G(\boldsymbol{r},\boldsymbol{r}_1)s_1\psi_1(\boldsymbol{r}_1). \qquad (3.4)\end{aligned}$$

We can evaluate ψ_1 at $\boldsymbol{r}_1$ and ψ_2 at $\boldsymbol{r}_2$ and combine the result into a matrix equation. Remember that the Green function is symmetric in $\boldsymbol{r}_1, \boldsymbol{r}_2$!

$$\begin{pmatrix} \phi(\boldsymbol{r}_1) \\ \phi(\boldsymbol{r}_2) \end{pmatrix} = \begin{pmatrix} 1 & -s_2 G(\boldsymbol{r}_1,\boldsymbol{r}_2) \\ -s_1 G(\boldsymbol{r}_1,\boldsymbol{r}_2) & 1 \end{pmatrix} \begin{pmatrix} \psi_1(\boldsymbol{r}_1) \\ \psi_2(\boldsymbol{r}_2) \end{pmatrix}, \qquad (3.5)$$

or, inverting the matrix,

$$\begin{pmatrix} \psi_1(\boldsymbol{r}_1) \\ \psi_2(\boldsymbol{r}_2) \end{pmatrix} = \begin{pmatrix} 1 & -s_2 G(\boldsymbol{r}_1,\boldsymbol{r}_2) \\ -s_1 G(\boldsymbol{r}_1,\boldsymbol{r}_2) & 1 \end{pmatrix}^{-1} \begin{pmatrix} \phi(\boldsymbol{r}_1) \\ \phi(\boldsymbol{r}_2) \end{pmatrix}. \qquad (3.6)$$

This is a matrix equation for the values of ψ_1 and ψ_2 at $\boldsymbol{r}_1$ and $\boldsymbol{r}_2$ respectively. Going back to the integral equation for the full wave function ψ we have,

$$\begin{aligned} \psi(\boldsymbol{r}) &= \phi(\boldsymbol{r}) + s_1\psi_1(\boldsymbol{r}_1)G(\boldsymbol{r},\boldsymbol{r}_1) + s_2\psi_2(\boldsymbol{r}_2)G(\boldsymbol{r},\boldsymbol{r}_2) \\ &= \phi(\boldsymbol{r}) + \begin{pmatrix} s_1G(\boldsymbol{r},\boldsymbol{r}_1) & s_2G(\boldsymbol{r},\boldsymbol{r}_2)\end{pmatrix} \begin{pmatrix} \psi_1(\boldsymbol{r}_1) \\ \psi_2(\boldsymbol{r}_2)\end{pmatrix}. \end{aligned} \tag{3.7}$$

Now plug in result of Eq. 3.6 to get

$$\begin{aligned} \psi(\boldsymbol{r}) &= \phi(\boldsymbol{r}) \\ &+ \begin{pmatrix} s_1G(\boldsymbol{r},\boldsymbol{r}_1) & s_2G(\boldsymbol{r},\boldsymbol{r}_2)\end{pmatrix} \begin{pmatrix} 1 & -s_2G(\boldsymbol{r}_1,\boldsymbol{r}_2) \\ -s_1G(\boldsymbol{r}_1,\boldsymbol{r}_2) & 1 \end{pmatrix}^{-1} \begin{pmatrix} \phi(\boldsymbol{r}_1) \\ \phi(\boldsymbol{r}_2)\end{pmatrix} \\ &= \phi(\boldsymbol{r}) \\ &+ \begin{pmatrix} G(\boldsymbol{r},\boldsymbol{r}_1) & G(\boldsymbol{r},\boldsymbol{r}_2)\end{pmatrix} \begin{pmatrix} s_1 & 0 \\ 0 & s_2 \end{pmatrix} \begin{pmatrix} 1 & -s_2G(\boldsymbol{r}_1,\boldsymbol{r}_2) \\ -s_1G(\boldsymbol{r}_1,\boldsymbol{r}_2) & 1 \end{pmatrix}^{-1} \begin{pmatrix} \phi(\boldsymbol{r}_1) \\ \phi(\boldsymbol{r}_2)\end{pmatrix}. \end{aligned} \tag{3.8}$$

The product of the two matrices appearing above can be thought of as the t-matrix for the two scatterers taken together, because it appears between the Green function and the incident wave to give the scattered wave.

What we really want to get out of this is $F(\theta)$, which is the scattering amplitude. After we have it, we will do a partial wave expansion. So far, we have an expression for $\psi(\boldsymbol{r})$ which is a matrix equation involving the free Green function, the incident wave evaluated at points $\boldsymbol{r}_1, \boldsymbol{r}_2$, and s_1, s_2. As shown in Sec. 2.1, the s_i are related to the single scatterer scattering amplitudes f_i, and the exact relationship depends on the space dimension. In 3D, the relation is

$$s_i = -4\pi f_i. \tag{3.9}$$

The first step toward computing $F(\theta)$ is finding the inverse of the matrix $\boldsymbol{M}$ and plugging into our expression for ψ (with some obvious abbreviations):

$$\boldsymbol{M}^{-1} = \begin{pmatrix} 1 & -s_2G_{12} \\ -s_1G_{12} & 1 \end{pmatrix}^{-1} = \frac{1}{1 - s_1s_2G_{12}^2} \begin{pmatrix} 1 & s_2G_{12} \\ s_1G_{12} & 1 \end{pmatrix}. \tag{3.10}$$

This gives for $\psi(\boldsymbol{r})$

$$\psi(\boldsymbol{r}) = \phi(\boldsymbol{r}) + \frac{G(\boldsymbol{r},\boldsymbol{r}_1)\left[s_1\phi(\boldsymbol{r}_1) + s_1s_2G_{12}\phi(\boldsymbol{r}_2)\right] + G(\boldsymbol{r},\boldsymbol{r}_2)\left[s_2\phi(\boldsymbol{r}_2) + s_1s_2G_{12}\phi(\boldsymbol{r}_1)\right]}{1 - s_1s_2G_{12}^2}. \tag{3.11}$$

This expression is applicable to both the 2D and 3D cases – all that one needs to do at this point is plug in the proper form of the Green function and the s_i's. For general $\boldsymbol{r}_i$ the expression for ψ is quite horrendous, but it simplifies considerably if one makes some reasonable assumptions. First of all, take $\boldsymbol{r}_{1,2} = \pm\frac{d}{2}\hat{z}$. An incident wave $\phi(\boldsymbol{r}) = \exp(i\boldsymbol{k}\cdot\boldsymbol{r})$ is everywhere assumed. Henceforth the single scattering amplitude is assumed to be the same for both scatterers, denoted simply by f. Also, we make the following large r approximation

$$\frac{e^{ik|\boldsymbol{r}-\boldsymbol{r}_i|}}{|\boldsymbol{r}-\boldsymbol{r}_i|} \to \frac{e^{ikr}e^{-ik\hat{\boldsymbol{r}}\cdot\boldsymbol{r}_i}}{r}. \tag{3.12}$$

Making all these substitutions, ψ becomes

$$\psi(\boldsymbol{r}) = e^{i\boldsymbol{k}\cdot\boldsymbol{r}} + F(\theta)\frac{e^{ikr}}{r}, \tag{3.13}$$

where $F(\theta)$ is

$$F(\theta) = \frac{2f\left[\cos\left(\frac{kd}{2}\cos\theta - \frac{k_z d}{2}\right) + \frac{f}{d}e^{ikd}\cos\left(\frac{kd}{2}\cos\theta + \frac{k_z d}{2}\right)\right]}{1 - \frac{f^2}{d^2}e^{2ikd}}. \tag{3.14}$$

Here k_z is the z-component of the incident wave vector $\boldsymbol{k}$. Later in this chapter, we will show that $F(\theta)$ satisfies the optical theorem, as long as f does.

The natural thing to do at this point is a partial wave expansion. At low incident energies, the dominant part of the total scattering cross section comes from the s- and p-wave cross sections, and the higher moments may be effectively ignored. In any case, doing the partial wave expansion allows us to see just how important (or unimportant) higher partial waves are. The expansion is,

$$F(\theta) = \sum_{l=0}^{\infty} F_l(2l+1)P_l(\cos\theta), \tag{3.15}$$

where there is no sum over m because the collection of scatterers has azimuthal symmetry. That is, $m = 0$ in every term of the sum. The partial wave expansion is achieved by multiplying Eq. 3.14 by a Legendre polynomial in $\cos\theta$ and integrating. We will need the orthogonality relations for the Legendre polynomials:

$$\int_{-1}^{1} P_l(\cos\theta)P_{l'}(\cos\theta)\ d(\cos\theta) = \frac{2}{2l+1}\delta_{ll'}. \tag{3.16}$$

The required integrations may be achieved with the help of Gegenbauer's generalization of Poisson's integral representation of the spherical Bessel functions [1, pg. 438]:

$$j_n(z) \quad = \quad \frac{(-i)^n}{2}\int_0^{\pi} e^{iz\cos\theta}P_n(\cos\theta)\sin\theta\ d\theta$$

$$
\begin{aligned}
&= \frac{(-i)^n}{2}\int_{-1}^{1} e^{izx} P_n(x)\ dx \\
&= \frac{i^n}{2}\int_{-1}^{1} e^{-izx} P_n(x)\ dx. \qquad (3.17)
\end{aligned}
$$

The last equation is only true for real z, which is in fact the case (we have $z = kd/2$). After a bit of algebra we find for the partial wave amplitudes:

$$F_l = \frac{2 f j_l\left(\frac{kd}{2}\right)\left[\cos\left(\frac{k_z d}{2} - \frac{\pi l}{2}\right) + \frac{f}{d} e^{ikd} \cos\left(\frac{k_z d}{2} + \frac{\pi l}{2}\right)\right]}{1 - \frac{f^2}{d^2} e^{2ikd}}. \qquad (3.18)$$

If we want to see how this scattering amplitude behaves as a function of energy, say, we need an explicit form for the single scattering amplitude, f. We want to make each scatterer individually resonant, and f must also satisfy the optical theorem. An example of such a f is,

$$f(k) = \frac{\gamma^2}{E_0 - k^2/2 - ik\gamma^2}, \qquad (3.19)$$

where E_0 is the resonance energy, and $\Gamma_0 = 2k\gamma^2$ is the width of the resonance. This f satisfies the optical theorem,

$$\sigma_{tot} = \frac{4\pi}{k}\mathrm{Im}[f(\boldsymbol{k} = \boldsymbol{k}_0)]. \qquad (3.20)$$

In Fig. 3.3 we plot the partial wave cross sections for two nearby resonant scatterers. For comparison, the single scatterer cross section is also shown. One notable feature is the symmetric splitting of the s- and p-wave resonances about the single scatterer resonance. Also apparent is the broadening of the s-wave resonance by a factor of two, and the considerable narrowing of the p-wave resonance.

In Fig. 3.4 we plot the resonance energies and widths, respectively, as a function of the distance between the scatterers. For $k_0 d < 1$, the regime of the proximity resonance, we see that the p-wave resonance is pushed to high energies, and its width decreases quadratically with $k_0 d$. Conversely, the s-wave resonance decreases in energy and broadens to $2\Gamma_0$, twice the width of the single scatterer resonance. In this regime, the resonances energies repel each other according to a Coulomb repulsion. What this means is the following: if the p-wave mode is excited, then the resonance (quasi-bound state) lowers its energy if the scatterers move apart; there is an effective Coulomb repulsion. If the s-wave mode is excited, then the resonance energy is lowered when the scatterers move closer together, with a Coulomb attraction. It will be shown in the next section that the resonance energy dependence on distance is indeed inverse with the scatterer separation.

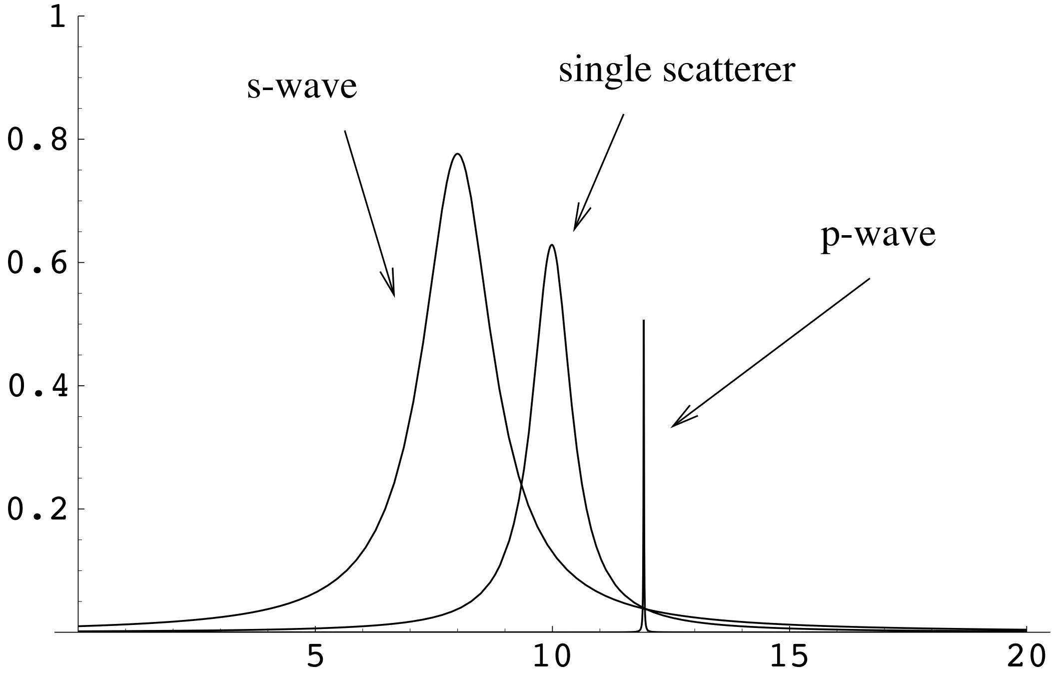

Figure 3.3: Partial wave cross sections for two nearby scatterers. The single scatterer cross section is also shown. The single scatterer parameters were $E_0 = k_0^2/2 = 10, \Gamma_0 = 1$. The distance between the scatterers was given by $k_0 d = 0.1$

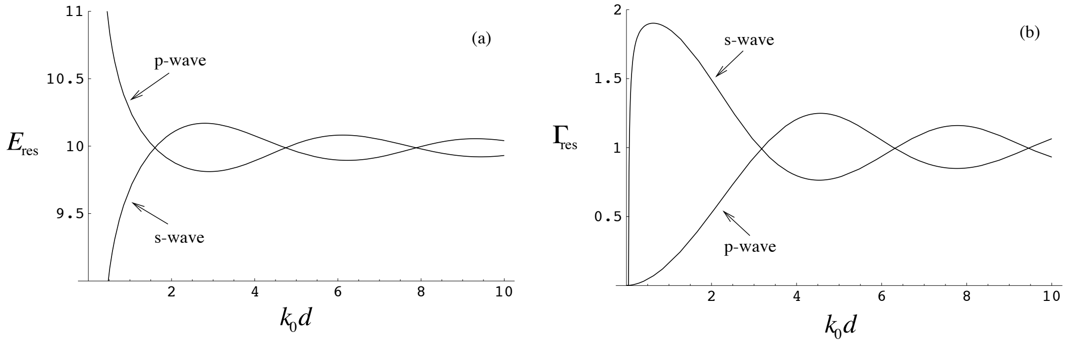

Figure 3.4: Resonance energies (a) and widths (b) for two nearby resonant scatterers in 3D. The single scatterer parameters were $E_0 = k_0^2/2 = 10, \Gamma_0 = 1$.

As the scatterers move farther from each other, the peak positions of each resonance oscillate about E_0, and the widths oscillate about Γ_0. However, this oscillation would be difficult to detect in practice because the widths of the resonances are comparable to the splitting in the oscillatory regime, so that the peaks are strongly overlapping.

For very small values of $k_0 d$, the s-wave resonance width turns over and approaches zero. This strange behavior will be discussed in detail in the next section.

3.3 Resonance energies and widths: 3D case

In looking at Fig. 3.4 one might be reminded of Bessel functions. The curves showing the resonant peak positions versus distance look remarkably like the zeroth order spherical Neumann functions $y_0(k_0 d)$, and the widths like the Bessel function $j_0(k_0 d)$. In fact, the resonance poles can be approximated quite well for nearly all scatterer separations by,

$$\begin{aligned} E_\pm &= E_0 - \frac{i\Gamma_0}{2} \pm \frac{\Gamma_0}{2}\left(y_0(k_0 d) - i j_0(k_0 d)\right) \\ &= E_0 - \frac{i\Gamma_0}{2} \mp \frac{\Gamma_0}{2}\frac{e^{ik_0 d}}{k_0 d}. \end{aligned} \tag{3.21}$$

To show this, we plug Eq. 3.21 into the denominator of Eq. 3.14 and show that the two roots $E_\pm$ satisfy,

$$1 - \frac{f^2}{d^2} e^{2ikd} = 0, \tag{3.22}$$

with $k = \sqrt{2E_\pm}$. A root of Eq. 3.22 corresponds to a pole of the scattering amplitude, that is, a resonance.

Using the single scatterer amplitude f, given by Eq. 3.19, Eq. 3.22 becomes,

$$\frac{\gamma^4}{d^2} e^{2ikd} = \left(E_0 - E_\pm - ik\gamma^2\right)^2. \tag{3.23}$$

First let us concentrate on the right hand side of Eq. 3.23. Substituting Eq. 3.21, we have,

$$\begin{aligned} \text{rhs} &= \left(E_0 - \left(E_0 - \frac{i\Gamma_0}{2} \mp \frac{\Gamma_0}{2}\frac{e^{ik_0 d}}{k_0 d}\right) - i\gamma^2\sqrt{2E_0 - i\Gamma_0 \mp \Gamma_0 \frac{e^{ik_0 d}}{k_0 d}}\right)^2 \\ &= \left(\frac{i\Gamma_0}{2} \pm \frac{\Gamma}{2}\frac{e^{ik_0 d}}{k_0 d} - \frac{i\Gamma_0}{2}\sqrt{1 - \frac{\Gamma_0}{2E_0}\left(i \pm \frac{e^{ik_0 d}}{k_0 d}\right)}\right)^2 \\ &\approx \frac{\Gamma_0^2}{4}\left(\pm\frac{e^{ik_0 d}}{k_0 d} + i\frac{\Gamma_0}{4E_0}\left(i \pm \frac{e^{ik_0 d}}{k_0 d}\right)\right)^2 \end{aligned}$$

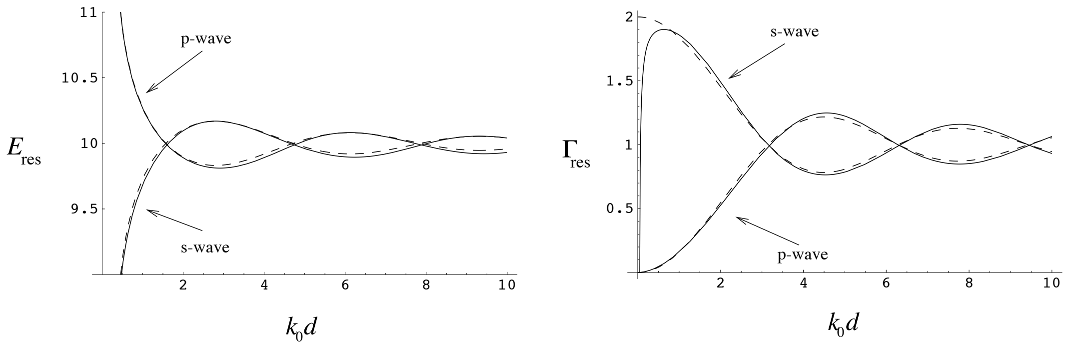

Figure 3.5: Comparison of the numerically computed resonance energies and widths (solid lines) with the spherical Bessel function approximation given by Eq. 3.21 (dashed lines). The approximation begins to break down for the s-wave width prediction near $k_0 d \sim 1$.

$$\approx \frac{\Gamma_0^2}{4} \frac{e^{2ik_0 d}}{(k_0 d)^2}, \tag{3.24}$$

where we have used the fact that the single scatterer resonance is well resolved, that is, $\Gamma_0 / E_0 \ll 1$. Now consider the left hand side of Eq. 3.23:

$$\begin{aligned} \text{lhs} &= \frac{\gamma^4}{d^2} e^{2ikd} \\ &= \frac{\Gamma_0^2}{(2k_0 d)^2} \exp\left[2ik_0 d \sqrt{1 - \frac{i\Gamma_0}{2E_0} \mp \frac{\Gamma_0}{2E_0} \frac{e^{ik_0 d}}{k_0 d}} \right] \\ &\approx \frac{\Gamma_0^2}{(2k_0 d)^2} \exp\left[2ik_0 d \left(1 - \frac{\Gamma_0}{4E_0} \left(i \pm \frac{e^{ik_0 d}}{k_0 d} \right) \right) \right] \\ &\approx \frac{\Gamma_0^2}{4} \frac{e^{2ik_0 d}}{(k_0 d)^2}, \end{aligned} \tag{3.25}$$

which is the same as Eq. 3.24. In Eq. 3.25 we have again used the fact that $\Gamma_0 / E_0 \ll 1$.

In Fig. 3.5 we compare the solutions given by Eq. 3.21 with numerically determined roots of Eq. 3.23. For most of the values, the fit is quite good. There is a slight discrepancy near the maxima and minima of the Bessel functions. This discrepancy is due to the fact that we dropped terms of order Γ_0 / E_0 in our calculation of the approximate expressions. For the curves shown, this parameter was $\Gamma_0 / E_0 = 0.1$. Numerical evidence shows that this discrepancy decreases linearly with Γ_0 / E_0.

However, there is a more substantial discrepancy between the numerical data and the formula for the s-wave width at small values of $k_0 d$. When $k_0 d$ becomes very small, then the s-wave resonance is pushed all the way down from $E = E_0$ to $E = 0$, and finally below threshold. At this point, the possibility of forming s-wave *bound* states exists, which

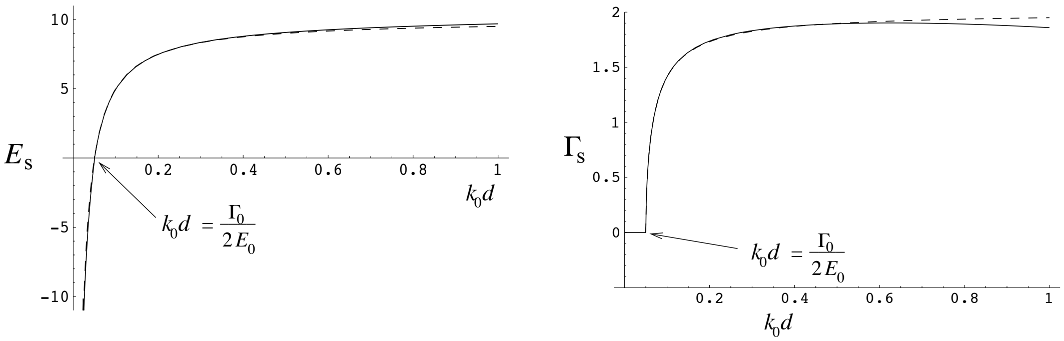

Figure 3.6: A closeup plot for $kd \ll 1$ for the s-wave resonance energy (left) and width (right). Numerically computed values are shown in solid lines, and the approximations in Eq. 3.26 and Eq. 3.27 are shown in dashed lines.

necessarily have zero width. Thus, for very small $k_0 d$, we must have that the width of the s-wave resonance turns over and dives toward zero, as we see in Fig. 3.5. The threshold for forming s-wave bound states occurs at $k_0 d = \Gamma_0 / 2E_0$, where $\Gamma_s \to 0$ and $E_s < 0$.

For very small values of $k_0 d$, we can expand Eq. 3.23 in powers of $k_0 d$ to find the behavior of the width of the s-wave resonance as bound states begin to form. One finds, in the limit $k_0 d \to 0$, for the s-wave resonance,

$$E_s \to E_0 - \frac{\Gamma_0}{2k_0 d} \tag{3.26}$$

$$\Gamma_s \to \frac{2\Gamma_0}{k_0}\sqrt{2\left(E_0 - \frac{\Gamma_0}{2k_0 d}\right)}. \tag{3.27}$$

Likewise, for the p-wave resonance,

$$E_p \to E_0 + \frac{\Gamma_0}{2k_0 d} \tag{3.28}$$

$$\Gamma_p \to \Gamma_0 \frac{(k_0 d)^2}{6}. \tag{3.29}$$

In Fig 3.6 we compare numerically computed energies and widths with the above expressions for the s-wave resonance. The agreement is quite good even up to $k_0 d \sim 1$.

3.4 Proximity resonance: 2D case

The derivation for the 2D case is completely analogous, the only difference being the different form for the Green function and for the s_i.

The appropriate Green function for the 2D case is a zeroth order Hankel function of the first kind:

$$G(\boldsymbol{r},\boldsymbol{r}') = -\frac{i}{4}H_0^{(1)}(k|\boldsymbol{r}-\boldsymbol{r}'|), \tag{3.30}$$

which has as an asymptotic form (taking $r \gg r'$),

$$G(\boldsymbol{r},\boldsymbol{r}') \to -\frac{e^{ikr}e^{-ik\hat{\boldsymbol{r}}\cdot\boldsymbol{r}'}e^{i\pi/4}}{\sqrt{8\pi kr}}. \tag{3.31}$$

We found in Sec. 2.1 that the relation between the single scattering amplitude f_i and s_i in 2D is,

$$s_i = -\sqrt{8\pi k}e^{-i\pi/4}f_i. \tag{3.32}$$

Note that in contrast to the 3D case, s_i is not simply proportional to f_i, but the relation depends on k. This is basically due to the fact that in 2D, the Green function has no units, but in 3D $G(\boldsymbol{r},\boldsymbol{r}')$ has units of $1/r$.

The Green function and the form for s_i must now be substituted into the matrix equation for ψ, Eq. 3.11, from which we extract the scattering amplitude. This time we assume the two scatters are placed symmetrically about the origin on the x-axis, a distance d apart, and θ is the angle up from the x-axis. The scatterers are identical, with single scattering amplitude f. One finds,

$$\psi(\boldsymbol{r}) = \phi(\boldsymbol{r}) + F(\theta)\frac{e^{ikr}}{\sqrt{r}}, \tag{3.33}$$

where the scattering amplitude $F(\theta)$ is,

$$F(\theta) = \frac{2f\left[\cos\left(\frac{kd}{2}\cos\theta - \frac{k_xd}{2}\right) + f\sqrt{\frac{i\pi k}{2}}H_0^{(1)}(kd)\cos\left(\frac{kd}{2}\cos\theta + \frac{k_xd}{2}\right)\right]}{1-\frac{i\pi k}{2}f^2\left(H_0^{(1)}(kd)\right)^2}. \tag{3.34}$$

Comparing Eq 3.14 with Eq. 3.34 the similarity is apparent.

We now expand $F(\theta)$ in the eigenfunctions of angular momentum particular to two dimensional space:

$$F(\theta) = \sum_{l=-\infty}^{\infty} F_l e^{il\theta}. \tag{3.35}$$

Using a similar trick as before, we multiply both sides by $e^{-il'\theta}$ and integrate $0 \to 2\pi$, using the orthonormal relations,

$$\int_0^{2\pi} e^{i(l-l')\theta}\, d\theta = 2\pi\delta_{ll'}. \tag{3.36}$$

We can take care of the integrals which appear by using one of the integral representations of the Bessel function $J_n(x)$

$$\begin{aligned} J_n(x) &= \frac{i^{-n}}{2\pi}\int_0^{2\pi} e^{ix\cos\theta+in\theta}\ d\theta \\ &= \frac{(-i)^{-n}}{2\pi}\int_0^{2\pi} e^{-ix\cos\theta-in\theta}\ d\theta, \end{aligned} \tag{3.37}$$

where the last equation is only true if the argument x is real; in our case $x = kd/2$. Also useful in getting the answer is the parity relation of the Bessel functions,

$$J_l(x) = (-1)^l J_{-l}(x). \tag{3.38}$$

After a straightforward but somewhat lengthy calculation, we find for the lth partial wave scattering amplitude,

$$F_l = \frac{2fJ_l(\frac{kd}{2})\left[\cos\left(\frac{k_x d}{2}-\frac{\pi l}{2}\right)+f\sqrt{\frac{i\pi k}{2}}\,H_0^{(1)}(kd)\cos\left(\frac{k_x d}{2}+\frac{\pi l}{2}\right)\right]}{1-\frac{i\pi k}{2}f^2\left(H_0^{(1)}(kd)\right)^2}. \tag{3.39}$$

For the purposes of investigating the two-scatterer amplitude, we are free to choose any single scattering amplitude f as long as it satisfies the optical theorem in two dimensions:

$$\sigma_{tot} = \sqrt{\frac{8\pi}{k}}\mathrm{Im}[e^{-i\pi/4}f(\boldsymbol{k}=\boldsymbol{k}_0)]. \tag{3.40}$$

An example of such a f, with resonant energy E_0 and width $\Gamma_0 = 2\sqrt{k}\gamma^2$, is

$$f(k) = \frac{\sqrt{\frac{2}{\pi}}e^{i\pi/4}\gamma^2}{E_0 - k^2/2 - i\sqrt{k}\gamma^2}. \tag{3.41}$$

In Fig. 3.7 we plot the partial wave cross sections for two nearby resonant scatterers. For comparison, the single scatterer cross section is also shown. As in the 3D case, the symmetric splitting of the s- and p-wave resonances about the single scatterer resonance is obvious. Also apparent is the broadening of the s-wave resonance by a factor of two, and the considerable narrowing of the p-wave resonance.

In Fig. 3.8 we plot the resonance energies and widths, respectively, as a function of the distance between the scatterers. The behavior is very similar to that of the 3D case in Fig. 3.4. One difference, however, is the dependence of the splitting between the s- and p-wave resonances: rather than varying as $1/kd$, it appears logarithmic in kd. We will see in the next section that this indeed is the case. Also, the turnover of the s-wave resonance width appears to be suppressed compared with the 3D case. This will be discussed in detail in the following sections.

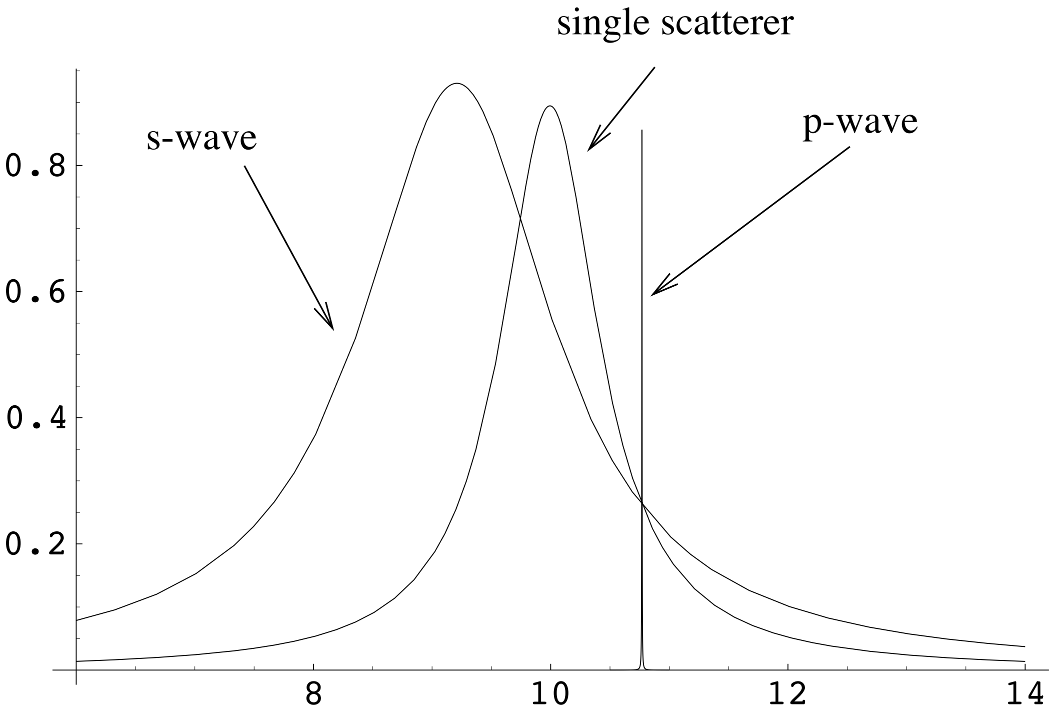

Figure 3.7: Partial wave cross sections for two nearby scatterers. The single scatterer cross section is also shown. The single scatterer parameters were $E_0 = k_0^2/2 = 10, \Gamma_0 = 1$. The distance between the scatterers was given by $k_0 d = 0.1$

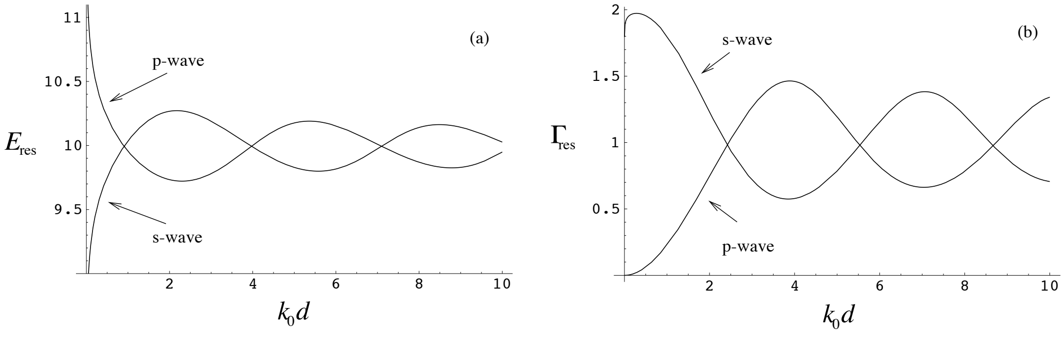

Figure 3.8: Resonance energies (a) and widths (b) for two nearby resonant scatterers in 2D. The single scatterer parameters were $E_0 = 10, \Gamma_0 = 1$.

3.5 Resonance energies and widths: 2D case

The resonance energies and widths for the 2D case can be found in a similar way to that in Sec. 3.3. The poles of the scattering amplitude are determined by the roots of

$$1 - \frac{i\pi k}{2} f^2 \left(H_0^{(1)}(kd)\right)^2 = 0, \tag{3.42}$$

with f given by Eq. 3.41. Similar to the 3D case, the roots can be well approximated by,

$$\begin{aligned} E_\pm &= E_0 - \frac{i\Gamma_0}{2} \pm \frac{\Gamma_0}{2}\left(Y_0(k_0 d) - iJ_0(k_0 d)\right) \\ E_\pm &= E_0 - \frac{i\Gamma_0}{2}\left(1 \pm H_0^{(1)}(k_0 d)\right). \end{aligned} \tag{3.43}$$

To show this, we insert Eq. 3.43 into Eq. 3.42 and, as in the 3D case, use the fact that the single scatterer resonance is well resolved, that is, $\Gamma_0/E_0 \ll 1$. Eq. 3.42 becomes,

$$-\gamma^4 k \left(H_0^{(1)}(kd)\right)^2 = (E_0 - E_\pm - i\sqrt{k}\gamma^2)^2. \tag{3.44}$$

First we will concentrate on the right hand side of Eq. 3.44. We find,

$$\begin{aligned} \text{rhs} &= \left[E_0 - \left(E_0 - \frac{i\Gamma_0}{2}\left(1 \pm H_0^{(1)}(k_0 d)\right)\right) - \frac{i\Gamma_0}{2}\left(1 - \frac{i\Gamma_0}{2E_0}\left(1 \pm H_0^{(1)}(k_0 d)\right)\right)^{\frac{1}{4}}\right]^2 \\ &\approx \left[\frac{i\Gamma_0}{2}\left(H_0^{(1)}(k_0 d) + \frac{i\Gamma_0}{8E_0}\left(1 \pm H_0^{(1)}(k_0 d)\right)\right)\right]^2 \\ &\approx -\frac{\Gamma_0^2}{4}\left(H_0^{(1)}(k_0 d)\right)^2. \end{aligned} \tag{3.45}$$

The left hand side of Eq. 3.44 gives,

$$\text{lhs} = -\frac{\Gamma_0^2}{4k_0} k \left(H_0^{(1)}(kd)\right)^2 \tag{3.46}$$

$$\approx -\frac{\Gamma_0^2}{4}\left(H_0^{(1)}(k_0 d)\right)^2, \tag{3.47}$$

which is the same as Eq. 3.45. Thus Eq. 3.43 is proven.

In Fig. 3.9 we compare the approximations given by Eq. 3.43 with the numerically computed roots of Eq. 3.42. We see that the agreement is quite good for nearly all values of $k_0 d$. The discrepancy at the maxima and minima of the Bessel functions is due to neglecting of terms of order Γ_0/E_0 in the approximations above. As $\Gamma_0/E_0 \to 0$, these discrepancies vanish.

However, as in the 3D case, we see that the s-wave width does not actually approach $\Gamma_s = 2\Gamma_0$ at zero energy, but turns over and approaches zero near $k_0 d = 0$. The

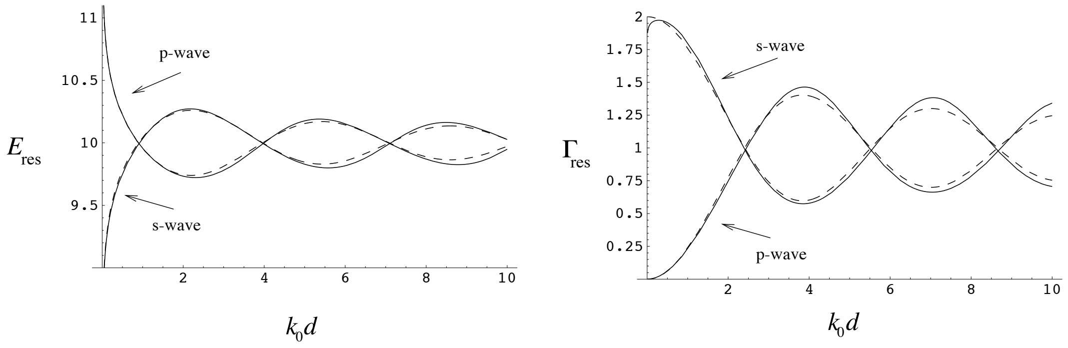

Figure 3.9: Comparison of the numerically computed resonance energies and widths (solid lines) with the Bessel function approximation given by Eq. 3.44 (dashed lines). The approximation breaks down for the s-wave width prediction for $k_0d \ll 1$.

reason for this is the same as in the 3D case. As the peak splitting gets larger and larger, the s-wave resonance energy approaches zero. However, the value of k_0d for which $E_s = 0$ is typically extremely small, for reasonable values of E_0 and Γ_0, as we shall see below. To find the behavior for small k_0d, we expand Eq. 3.42 and find,

$$E_s \rightarrow E_0 + \frac{\Gamma_0}{\pi}\ln k_0 d \tag{3.48}$$

$$\Gamma_s \rightarrow \frac{2\Gamma_0}{1 - \frac{\Gamma_0}{2\pi E_0}\left(1 + \ln k_0 d\right)}, \tag{3.49}$$

and for the p-wave,

$$E_p \rightarrow E_0 - \frac{\Gamma_0}{\pi}\ln k_0 d \tag{3.50}$$

$$\Gamma_p \rightarrow \Gamma_0 \frac{(k_0 d)^2}{4}. \tag{3.51}$$

This means that the value for which the s-wave resonance energy crosses threshold is given by,

$$k_0 d = e^{-\pi E_0/\Gamma_0}. \tag{3.52}$$

For $E_0/\Gamma_0 = 10$, this value is $k_0d = 2.2 \times 10^{-14}$. Thus, we may safely neglect the possibility of forming s-wave bound states in the 2D case.

3.6 More than two scatterers

It turns out that the method developed above for two point scatterers extends easily to several scatterers. In general, for many scatterers located at positions $\{\boldsymbol{r}_i\}$ we

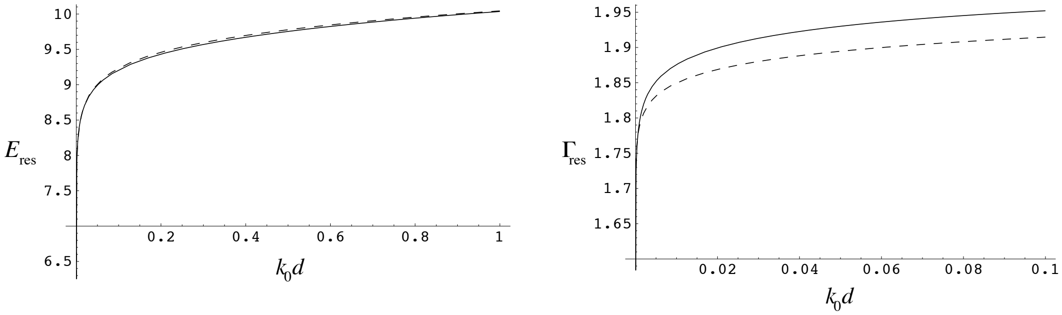

Figure 3.10: A closeup plot for $kd \ll 1$ for the s-wave resonance width shown in Fig. 3.8. The behavior $kd = 0$ is $\Gamma_s \sim -1/\ln(k_0 d)$.

have for ψ,

$$\psi(\boldsymbol{r}) = \phi(\boldsymbol{r}) + \sum_{ij}[M^{-1}]_{ij} s_i G(\boldsymbol{r}, \boldsymbol{r}_i)\phi(\boldsymbol{r}_j), \tag{3.53}$$

with the matrix $\boldsymbol{M}$ given by

$$M_{ij} = \delta_{ij} - s_j G_{ij}(1 - \delta_{ij}). \tag{3.54}$$

This leads to a scattering amplitude $F(\Omega)$,

$$F(\Omega) = \sum_{ij}[M^{-1}]_{ij} f_i e^{-ik\hat{\boldsymbol{r}}\cdot\boldsymbol{r}_i}\phi(\boldsymbol{r}_j), \tag{3.55}$$

where we understand Ω to be the angles (θ, ϕ) in 3D, and just θ in 2D. It turns out the above expression is correct in both 2D and 3D. This has to do with the relation between the s_i's and $G(\boldsymbol{r}, \boldsymbol{r}')$ in each case. Actually, the product, $s_i G(\boldsymbol{r}, \boldsymbol{r}')$, for $r \gg r'$ reduces to

$$\begin{aligned} s_i G(\boldsymbol{r}, \boldsymbol{r}_i) &\rightarrow f_i \frac{e^{ikr}}{r} e^{-ik\hat{\boldsymbol{r}}\cdot\boldsymbol{r}_i} \text{ (in 3D)} \\ &\rightarrow f_i \frac{e^{ikr}}{\sqrt{r}} e^{-ik\hat{\boldsymbol{r}}\cdot\boldsymbol{r}_i} \text{ (in 2D)}. \end{aligned}$$

One can perform a partial wave expansion on Eq. 3.55, in a way similar to what was done previously for two scatters. The result in two dimensions is,

$$\begin{aligned} f_l &= \frac{1}{2\pi}\int_0^{2\pi} F(\theta) e^{-il\theta} d\theta \\ &= \sum_{ij}[M^{-1}]_{ij} f_i e^{ikx_j} \int_0^{2\pi} e^{-ik\hat{\boldsymbol{r}}\cdot\boldsymbol{r}_i - il\theta}\, d\theta \\ &= \sum_{ij}[M^{-1}]_{ij} f_i J_l(kr_i) e^{i(kx_j - l\theta_i - l\pi/2)}, \end{aligned} \tag{3.56}$$

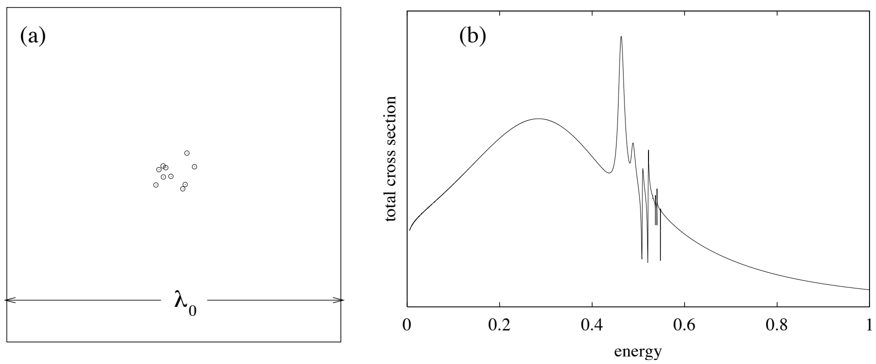

Figure 3.11: Total cross section versus energy for a random collection of 10 scatterers. In (a), the scatterer locations are shown. The resonance wavelength, λ_0, is indicated in the figure. In (b), the total cross section is shown. The single scatterer parameters were $E_0 = 0.5, \Gamma_0 = 0.05$

where we have taken an incident wave of the form $\phi = e^{ikx}$ without loss of generality. The position of scatterer i is given by (r_i, θ_i) and $x_i = r_i \cos\theta_i$. This result is correct even for non-identical scatterers, and is analytic. The hard part of course is inverting the matrix M, which must be done numerically when the number of scatterers is more than a few.

In Fig. 3.11, the total cross section is shown for a cloud of ten randomly located nearby scatterers. Very sharp features are apparent in the cross section. Also, we see that the s-wave mode is broadened by a factor of ten, which is just the number of scatterers. This is analogous to the factor of two broadening in the s-wave mode for two nearby scatterers discussed above.

The partial wave expansion in 3D for a generic collection of scatterers is more complicated, first because there are more angles to integrate over, and also because there is in general no azimuthal symmetry of the collection of scatterers. This means the partial wave expansion is an expansion in the spherical harmonics $Y_{lm}(\theta, \phi)$, where there are sums over both l and m. The partial wave expansion then takes the form,

$$F(\theta, \phi) = \sum_{l=0}^{\infty} \sum_{m=-l}^{l} f_{lm} Y_{lm}(\theta, \phi). \tag{3.57}$$

Using the orthogonality relation,

$$\int_{\Omega} Y^*_{l'm'}(\theta, \phi) Y_{lm}(\theta, \phi)\, d\Omega = \delta_{ll'} \delta_{mm'}, \tag{3.58}$$

we can extract the amplitude f_{lm}. This is done by multiplying Eq. 3.57 by $Y^*_{l'm'}(\theta,\phi)$ and integrating over angles. We find,

$$\begin{aligned} f_{lm} &= \int_\Omega F(\theta,\phi) Y^*_{lm}(\theta,\phi)\ d\Omega \\ &= \sum_{ij} [M^{-1}]_{ij} f_i e^{ikz_j} \int_\Omega e^{-ik\hat{\boldsymbol{r}}\cdot\boldsymbol{r}_i} Y^*_{lm}(\theta,\phi)\ d\Omega, \end{aligned}$$

where we have taken the incident wave $\phi = e^{ikz}$ without loss of generality. We can do the integral by expanding the exponential in spherical harmonics. A general plane wave $e^{i\boldsymbol{k}\cdot\boldsymbol{r}}$ can be expanded thus,

$$e^{i\boldsymbol{k}\cdot\boldsymbol{r}} = 4\pi \sum_{l=0}^{\infty} \sum_{m=-l}^{l} i^l j_l(kr) Y^*_{lm}(\theta_k,\phi_k) Y_{lm}(\theta_r,\phi_r), \tag{3.59}$$

where (θ_k,ϕ_k) are the angles defining the direcition of $\boldsymbol{k}$ and (θ_r,ϕ_r) define the direction of $\boldsymbol{r}$. Therefore we have for our plane wave, $e^{-ik\hat{\boldsymbol{r}}\cdot\boldsymbol{r}_i}$,

$$e^{-ik\hat{\boldsymbol{r}}\cdot\boldsymbol{r}_i} = 4\pi \sum_{l=0}^{\infty} \sum_{m=-l}^{l} (-i)^l j_l(kr_i) Y_{lm}(\theta,\phi) Y^*_{lm}(\theta_i,\phi_i), \tag{3.60}$$

where (r_i,θ_i,ϕ_i) are the coordinates of scatterer i. The $Y^*_{lm}(\theta_i,\phi_i)$ are just constants, as far as our integral is concerned, so we can use the orthogonality relations for the Y_{lm} to do the integral. We have then for the partial wave amplitudes,

$$\begin{aligned} f_{lm} &= 4\pi \sum_{ij} [M^{-1}]_{ij} f_i e^{ikz_j} \sum_{l'=0}^{\infty} \sum_{m'=-l'}^{l} (-i)^{l'} j_{l'}(kr_i) Y^*_{l'm'}(\theta_i,\phi_i) \int_\Omega Y^*_{l'm'}(\theta,\phi) Y_{lm}(\theta,\phi)\ d\Omega \\ &= 4\pi \sum_{ij} [M^{-1}]_{ij} f_i e^{ikz_j} \sum_{l'=0}^{\infty} \sum_{m'=-l'}^{l} (-i)^{l'} j_{l'}(kr_i) Y^*_{l'm'}(\theta_i,\phi_i) \delta_{ll'} \delta_{mm'} \\ &= 4\pi \sum_{ij} [M^{-1}]_{ij} f_i j_l(kr_i) Y^*_{lm}(\theta_i,\phi_i) e^{i(kz_j - l\pi/2)}. \end{aligned} \tag{3.61}$$

Comparing Eq. 3.61 with Eq. 3.56, the similarity is obvious. We almost could have guessed the 3D formula, given the 2D formula.

3.7 Total cross section

We can use Eq. 3.55 and the optical theorem to find simple expressions for the total cross section. Assuming an incident wave of the form $\phi(\boldsymbol{r}) = e^{i\boldsymbol{k}_0\cdot\boldsymbol{r}}$, $|\boldsymbol{k}_0| = k$, and using the optical theorem given by Eq. 3.20, we have for the 3D case,

$$\sigma_{\text{tot}} = \frac{4\pi}{k}\text{Im}\left[\sum_{ij}\left[M^{-1}\right]_{ij} f_i e^{-i\boldsymbol{k}_0\cdot\boldsymbol{\rho}_{ij}}\right], \tag{3.62}$$

where,

$$\boldsymbol{\rho}_{ij} = \boldsymbol{r}_i - \boldsymbol{r}_j. \tag{3.63}$$

If we average this expression over all possible incoming directions of the incident wave we find,

$$\begin{aligned}\langle\sigma_{\text{tot}}\rangle &= \frac{4\pi}{k}\frac{1}{4\pi}\text{Im}\left[\sum_{ij}\left[M^{-1}\right]_{ij} f_i \int_\Omega e^{-i\boldsymbol{k}_0\cdot\boldsymbol{\rho}_{ij}}\, d\Omega\right] \\ &= \frac{2\pi}{k}\text{Im}\left[\sum_{ij}\left[M^{-1}\right]_{ij} f_i \int_0^\pi e^{-ik\rho_{ij}\cos\theta}\sin\theta\, d\theta\right] \\ &= \frac{4\pi}{k}\sum_{ij} j_0(k\rho_{ij})\text{Im}\left[\left[M^{-1}\right]_{ij} f_i\right],\end{aligned} \tag{3.64}$$

where we have used one of the integral expressions of the spherical Bessel function $j_0(x)$, given in Eq. 3.17.

In 2D, the expression is similar. We have for the total cross section,

$$\sigma_{\text{tot}} = \sqrt{\frac{8\pi}{k}}\text{Im}\left[e^{-i\pi/4}\sum_{ij}\left[M^{-1}\right]_{ij} f_i e^{-i\boldsymbol{k}_0\cdot\boldsymbol{\rho}_{ij}}\right]. \tag{3.65}$$

Averaging over angles we find,

$$\langle\sigma_{\text{tot}}\rangle = \sqrt{\frac{8\pi}{k}}\frac{1}{2\pi}\text{Im}\left[e^{-i\pi/4}\sum_{ij}\left[M^{-1}\right]_{ij} f_i \int_0^{2\pi} e^{-i\boldsymbol{k}_0\cdot\boldsymbol{\rho}_{ij}}\, d\theta\right] \tag{3.66}$$

$$= \sqrt{\frac{8\pi}{k}}\sum_{ij} J_0(k\rho_{ij})\text{Im}\left[e^{-i\pi/4}\left[M^{-1}\right]_{ij} f_i\right], \tag{3.67}$$

where we have used Eq. 3.37 for the integral.

3.8 Optical theorem consistency check

To conclude this chapter, we will prove that the somewhat complicated expression in Eq. 3.14 satisfies the optical theorem in 3D.

The scattering amplitude for two point scatterers in 3D is

$$F(\theta) = \frac{2f\left[\cos\left(\frac{kd}{2}\cos\theta - \frac{k_z d}{2}\right) + \frac{f}{d}e^{ikd}\cos\left(\frac{kd}{2}\cos\theta + \frac{k_z d}{2}\right)\right]}{1 - \frac{f^2}{d^2}e^{2ikd}}. \tag{3.68}$$

If this scattering amplitude is to be physically allowed, it must satisfy the optical theorem:

$$\sigma_{tot} = \frac{4\pi}{k}\mathrm{Im}[F(\boldsymbol{k} = \boldsymbol{k}_0)], \tag{3.69}$$

where θ_0 is the angle that the incident wave makes with the z-axis.

We assume that the single scatterer amplitude, f, is independent of angle and that it also satisfies the optical theorem. Further, we will assume that the incident wave is along the z-axis. This assumption is not necessary for the proof, although it does simplify the work somewhat. Let's begin with the right hand side of Eq. 3.69. Substituting Eq. 3.68, we have,

$$\begin{aligned}
\mathrm{rhs} &= \frac{4\pi}{k}\mathrm{Im}\left[\frac{2f\left[\cos\left(\frac{kd}{2}\cos(0) - \frac{kd}{2}\right) + \frac{f}{d}e^{ikd}\cos\left(\frac{kd}{2}\cos(0) + \frac{kd}{2}\right)\right]}{1 - \frac{f^2}{d^2}e^{2ikd}}\right] \\
&= \frac{4\pi}{k}\mathrm{Im}\left[\frac{2f\left(1 + \frac{f}{d}e^{ikd}\cos kd\right)}{1 - \frac{f^2}{d^2}e^{2ikd}}\right].
\end{aligned}$$

To find the imaginary part, we multiply top and bottom by the complex conjugate of the denominator:

$$\begin{aligned}
\mathrm{rhs} &= \frac{4\pi}{k}\mathrm{Im}\left[\frac{2f\left(1 + \frac{f}{d}e^{ikd}\cos kd\right)\left(1 - \frac{(f^*)^2}{d^2}e^{-2ikd}\right)}{\left|1 - \frac{f^2}{d^2}e^{2ikd}\right|^2}\right] \\
&= \frac{8\pi}{k\left|1 - \frac{f^2}{d^2}e^{2ikd}\right|^2}\left[\mathrm{Im}(f) - \frac{|f|^2}{d^2}\mathrm{Im}\left(f^* e^{-2ikd}\right)\right. \\
&\qquad\qquad \left. + \frac{\cos kd}{d}\mathrm{Im}\left(f^2 e^{ikd}\right) - \frac{|f|^4\cos kd}{d^3}\mathrm{Im}\left(e^{-ikd}\right)\right]
\end{aligned} \tag{3.70}$$

We now need to expand the four terms in the above expression. The first term is simple. Because f also satisfies the optical theorem, we have,

$$\mathrm{Im}(f) = k|f|^2. \tag{3.71}$$

We can expand the other imaginary parts above thus:

$$\mathrm{Im}\left(f^* e^{-2ikd}\right) = \mathrm{Im}\left[\left(\mathrm{Re}(f) - i\mathrm{Im}(f)\right)\left(\cos 2kd - i\sin 2kd\right)\right]$$

$$\begin{aligned} &= -\mathrm{Im}(f)\cos 2kd - \mathrm{Re}(f)\sin 2kd \\ &= -k|f|^2\cos 2kd - \mathrm{Re}(f)\sin 2kd, \end{aligned} \tag{3.72}$$

and,

$$\begin{aligned} \mathrm{Im}\left(f^2e^{ikd}\right) &= \mathrm{Im}\left[(\mathrm{Re}(f)+i\mathrm{Im}(f))^2(\cos kd + i\sin kd)\right] \\ &= -\mathrm{Im}\left[\left(\mathrm{Re}^2(f)-\mathrm{Im}^2(f)+2i\mathrm{Re}(f)\mathrm{Im}(f)\right)(\cos kd+i\sin kd)\right] \\ &= \left(\mathrm{Re}^2(f)-\mathrm{Im}^2(f)\right)\sin kd + 2\mathrm{Re}(f)\mathrm{Im}(f)\cos kd. \end{aligned} \tag{3.73}$$

These expression in Eq. 3.73 can be simplified using

$$\mathrm{Re}^2(f)-\mathrm{Im}^2(f) = |f|^2 - 2k^2|f|^4. \tag{3.74}$$

Now, plugging in the results of Eq. 3.72 and Eq. 3.73 into our expression for the right hand side, we have,

$$\begin{aligned} \mathrm{rhs} &= \frac{8\pi}{k\left|1-\frac{f^2}{d^2}e^{2ikd}\right|^2}\Bigg[k|f|^2 + \frac{|f|^4}{d^3}\sin kd\cos kd \\ &\qquad + \frac{|f|^2}{d^2}\left(k|f|^2\cos 2kd + \mathrm{Re}(f)\sin 2kd\right) \\ &\qquad + \frac{\cos kd}{d}\left(\left(|f|^2-2k^2|f|^4\right)\sin kd + 2k|f|^2\mathrm{Re}(f)\cos kd\right)\Bigg]. \end{aligned} \tag{3.75}$$

This expression can be massaged a bit more, by using identities from trigonometry. We find eventually,

$$\begin{aligned} \mathrm{rhs} &= \frac{8\pi|f|^2}{\left|1-\frac{f^2}{d^2}e^{2ikd}\right|^2}\Bigg[1+\frac{\mathrm{Re}(f)}{d}+\sin 2kd\left(\frac{|f|^2}{2kd^3}+\frac{\mathrm{Re}(f)}{kd^2}+\frac{1-2k^2|f|^2}{2kd}\right) \\ &\qquad + \cos 2kd\left(\frac{|f|^2}{d^2}+\frac{\mathrm{Re}(f)}{d}\right)\Bigg]. \end{aligned} \tag{3.76}$$

Now we will evaluate the *left* hand side of Eq. 3.69, using Eq. 3.68 as input. This involves doing angular integrals over θ, ϕ. If $F(\theta)$ satisfies the optical theorem, we must have,

$$\mathrm{rhs} = \frac{4\pi}{k}\mathrm{Im}(F(0)) = \int |F(\theta)|^2\, d\Omega = \mathrm{lhs}. \tag{3.77}$$

First we need to find $|F(\theta)|^2$. That is,

$$|F(\theta)|^2 = \frac{4|f|^2}{\left|1-\frac{f^2}{d^2}e^{2ikd}\right|^2}\left[\cos\left(\frac{kd}{2}(1-\cos\theta)\right)+\frac{f}{d}e^{ikd}\cos\left(\frac{kd}{2}(1+\cos\theta)\right)\right]$$

$$
\begin{aligned}
&\times \left[\cos\left(\frac{kd}{2}(1-\cos\theta)\right) + \frac{f^*}{d}e^{-ikd}\cos\left(\frac{kd}{2}(1+\cos\theta)\right)\right] \\
= \frac{4|f|^2}{\left|1-\frac{f^2}{d^2}e^{2ikd}\right|^2} &\left[\cos^2\left(\frac{kd}{2}(1-\cos\theta)\right)\right. \\
&+ \frac{|f|^2}{d^2}\cos^2\left(\frac{kd}{2}(1+\cos\theta)\right) \\
&\left. + \cos\left(\frac{kd}{2}(1-\cos\theta)\right)\cos\left(\frac{kd}{2}(1+\cos\theta)\right)\left(\frac{f}{d}e^{ikd} + \frac{f^*}{d}e^{-ikd}\right)\right].
\end{aligned}
$$

The last term can be simplified using the identity

$$\cos(a-b)\cos(a+b) = \frac{1}{2}(\cos 2a + \cos 2b). \tag{3.78}$$

We find,

$$
\begin{aligned}
|F(\theta)|^2 = \frac{4|f|^2}{\left|1-\frac{f^2}{d^2}e^{2ikd}\right|^2} &\left[\cos^2\left(\frac{kd}{2}(1-\cos\theta)\right)\right. \\
&+ \frac{|f|^2}{d^2}\cos^2\left(\frac{kd}{2}(1+\cos\theta)\right) \\
&\left. + \frac{1}{d}\left(\mathrm{Re}(f)\cos kd - k|f|^2\sin kd\right)\left(\cos kd + \cos(kd\cos\theta)\right)\right].
\end{aligned}
\tag{3.79}
$$

Now, since the total cross section is the integral over all angles of the above expression, we will be needing to do integrals of the form,

$$\int_0^\pi \cos^2(a(1-\cos\theta))\sin\theta\ d\theta = 1 + \frac{\sin 4a}{4a}, \tag{3.80}$$

$$\int_0^\pi \cos^2(a(1+\cos\theta))\sin\theta\ d\theta = 1 + \frac{\sin 4a}{4a}, \tag{3.81}$$

and

$$\int_0^\pi \cos(2a\cos\theta)\sin\theta\ d\theta = \frac{\sin 2a}{a}, \tag{3.82}$$

where $a = kd/2$. Using these formulae, we have for the total cross section,

$$
\begin{aligned}
\sigma_{tot} &= \int |F(\theta)|^2 \sin\theta\ d\theta\ d\phi \\
&= 2\pi \int |F(\theta)|^2 \sin\theta\ d\theta \\
&= \frac{8\pi|f|^2}{\left|1-\frac{f^2}{d^2}e^{2ikd}\right|^2}\left[\left(1+\frac{|f|^2}{d^2}\right)\left(1+\frac{\sin 2kd}{2kd}\right)\right.
\end{aligned}
$$

$$
\begin{aligned}
&\qquad + \frac{1}{d}\Big(\mathrm{Re}(f)\cos kd - k|f|^2\sin kd\Big)\left(2\cos kd + \frac{2\sin kd}{kd}\right)\Bigg] \\
= &\ \frac{8\pi|f|^2}{\left|1-\frac{f^2}{d^2}e^{2ikd}\right|^2}\Bigg[1 + \frac{|f|^2}{d^2} + \sin 2kd\left(\frac{1}{2kd} + \frac{|f|^2}{2kd^3}\right) \\
&\qquad + \frac{2\mathrm{Re}(f)\cos^2 kd}{d} + \frac{2\mathrm{Re}(f)}{kd^2}\cos kd\sin kd \\
&\qquad - \frac{2k|f|^2}{d}\cos kd\sin kd - \frac{2|f|^2}{d^2}\sin^2 kd\Bigg]
\end{aligned}
$$

Now all the terms with products of trigonometric functions can be expanded to yield:

$$
\begin{aligned}
\sigma_{tot} \quad = &\ \frac{8\pi|f|^2}{\left|1-\frac{f^2}{d^2}e^{2ikd}\right|^2}\Bigg[1 + \frac{\mathrm{Re}(f)}{d} + \sin 2kd\left(\frac{|f|^2}{2kd^3} + \frac{\mathrm{Re}(f)}{kd^2} + \frac{1-2k^2|f|^2}{2kd}\right) \\
&\qquad + \cos 2kd\left(\frac{|f|^2}{d^2} + \frac{\mathrm{Re}(f)}{d}\right)\Bigg].
\end{aligned}
$$

Comparing this expression with Eq. 3.76, we see that the expressions are identical. Thus we have proven that the lengthy formula for $F(\theta)$, given by Eq. 3.68, indeed satisfies the optical theorem.

Chapter 4

Observation of Proximity Resonances in a Parallel-Plate Waveguide

4.1 Introduction

In the interest of determining whether proximity resonances actually exist in nature, we decided to look for them in the context of microwave scattering. A microwave system has several advantages: the geometry of the scattering system may be precisely controlled, there are no appreciable sources of decoherence, and perhaps most interestingly, there is a one-to-one correspondence between two dimensional microwave scattering and the scattering of electron waves in 2D governed by the Schrödinger equation. In fact, for the specific case of dielectric scattering considered below, there is a direct correspondence to the quantum mechanical scattering problem of two nearby square wells.

In this chapter, I will describe an experiment that, for the first time, observed the phenomenon of proximity resonances. Numerical simulations of the scattering problem were found to agree very well with the experimental results.

For the purposes of modeling the experiment, we developed a method of solving the scattering problem involving cylindrical basis functions centered on each scatterer. It turned out that the point scatterer model [10, 37], which was used in the original discussion of proximity resonances [20], was not sufficient to accurately model the experiment. In order for the point scatterer model to be applicable, at least two conditions must be met: $a \ll \lambda$, and $a \ll d$, where a is the physical radius of each scatterer, λ the wavelength, and d the distance between the scatterers. In our experiments, the first condition was always met, but the second was not.

4.2 Electromagnetism in two dimensions

Before we describe the experiment, we must learn a bit about electromagnetic waves in a parallel plate waveguide. Such a waveguide is formed by two perfectly conducting infinite plane sheets, placed parallel to one another. In this section I will derive the equations governing these waves. The plates of the cavity will be taken to be perpendicular to the z-axis. We begin with the source-free Maxwell equations for a homogeneous medium:

$$\begin{aligned} \nabla \cdot \boldsymbol{E} &= 0 && (4.1) \\ \nabla \cdot \boldsymbol{H} &= 0 && (4.2) \\ \nabla \times \boldsymbol{E} &= \frac{i\omega}{c}\boldsymbol{H} && (4.3) \\ \nabla \times \boldsymbol{H} &= -\frac{i\epsilon\omega}{c}\boldsymbol{E}, && (4.4) \end{aligned}$$

where ϵ is the dielectric constant of the medium, and we have assumed a harmonic time dependence $e^{-i\omega t}$ of the fields. These four vector equations are condensed from eight scalar equations relating the various components of $\boldsymbol{E}, \boldsymbol{H}$:

$$\frac{\partial E_x}{\partial x} + \frac{\partial E_y}{\partial y} + \frac{\partial E_z}{\partial z} = 0 \quad \text{from (4.1)} \qquad (4.5)$$

$$\frac{\partial H_x}{\partial x} + \frac{\partial H_y}{\partial y} + \frac{\partial H_z}{\partial z} = 0 \quad \text{from (4.2)} \qquad (4.6)$$

$$\left.\begin{aligned} \tfrac{\partial E_z}{\partial y} - \tfrac{\partial E_y}{\partial z} &= \tfrac{i\omega}{c} H_x \\ \tfrac{\partial E_x}{\partial z} - \tfrac{\partial E_z}{\partial x} &= \tfrac{i\omega}{c} H_y \\ \tfrac{\partial E_y}{\partial x} - \tfrac{\partial E_x}{\partial y} &= \tfrac{i\omega}{c} H_z \end{aligned}\right\} \text{from (4.3)} \qquad (4.7)$$

$$\left.\begin{aligned} \tfrac{\partial H_z}{\partial y} - \tfrac{\partial H_y}{\partial z} &= -\tfrac{i\epsilon\omega}{c} E_x \\ \tfrac{\partial H_x}{\partial z} - \tfrac{\partial H_z}{\partial x} &= -\tfrac{i\epsilon\omega}{c} E_y \\ \tfrac{\partial H_y}{\partial x} - \tfrac{\partial H_x}{\partial y} &= -\tfrac{i\epsilon\omega}{c} E_z \end{aligned}\right\} \text{from (4.4).} \qquad (4.8)$$

Because of the boundary condition forced on the solution by the presence of the plates, we must have a harmonic z-dependence for each of the components:

$$E_\alpha(x, y, z) = E_\alpha(x, y)e^{ik_z z} \qquad (4.9)$$

$$H_\alpha(x,y,z) \;=\; H_\alpha(x,y)e^{ik_z z}, \tag{4.10}$$

where $\alpha = x, y, z$, $k_z = \frac{n\pi}{L}$, and L is the separation between the plates. Substituting Eqs. 4.9, 4.10 into Eqs. 4.5, 4.6, 4.7, 4.8, we find,

$$E_x \;=\; \frac{i}{\epsilon\frac{\omega^2}{c^2} - k_z^2}\left(\frac{\omega}{c}\frac{\partial H_z}{\partial y} + k_z\frac{\partial E_z}{\partial x}\right) \tag{4.11}$$

$$E_y \;=\; \frac{i}{\epsilon\frac{\omega^2}{c^2} - k_z^2}\left(-\frac{\omega}{c}\frac{\partial H_z}{\partial x} + k_z\frac{\partial E_z}{\partial y}\right) \tag{4.12}$$

$$H_x \;=\; \frac{i}{\epsilon\frac{\omega^2}{c^2} - k_z^2}\left(-\frac{\epsilon\omega}{c}\frac{\partial E_z}{\partial y} + k_z\frac{\partial H_z}{\partial x}\right) \tag{4.13}$$

$$H_y \;=\; \frac{i}{\epsilon\frac{\omega^2}{c^2} - k_z^2}\left(\frac{\epsilon\omega}{c}\frac{\partial E_z}{\partial x} + k_z\frac{\partial H_z}{\partial y}\right). \tag{4.14}$$

Thus all the other field components can be expressed in terms of just two: E_z and H_z. In fact, one can show that with the knowledge of *any* two field components, one can generate all the others. However, for the lowest mode of a parallel plate cavity, called the transverse electromagnetic[1] (TEM) mode, E_z has a special significance, which we will discuss below.

Now we will discuss for a moment the boundary conditions on the electromagnetic fields at a perfectly conducting surface. We must have that both the parallel component of the electric field, $E_{||}$, and the perpendicular component of the magnetic field, $H_\perp$, are zero at the conducting surface. The z-dependence of the field amplitudes for the various components are shown for a few modes in Fig. 4.1. We see that the presence of the walls quantizes the fields in the z-direction, and that for the lowest mode, there is no variation of the fields in the z-direction at all. For this reason, we call the TEM mode *two dimensional.* Furthermore, for this mode, there is really only one fundamental component, which we can take to be E_z. Here "fundamental" means only that knowledge of E_z implies knowledge of both H_x and H_y, through Eqs. 4.13, 4.14.

Henceforth, we will only be concerned with the TEM mode, for it is this mode which is most interesting from the standpoint of drawing analogies to quantum mechanics, as we will see below. Now imagine enclosing some area in our parallel plate waveguide by placing metallic strips between the plates, forming a cavity, as shown in Fig. 4.2. What does the presence of these new walls mean for the TEM mode? Remember that the electric field is not allowed to have any component parallel to the surface of a conductor. Furthermore, there is only one nonzero component of the electric field active in the TEM mode,

---

[1] It is called the transverse electromagnetic mode because both the electric and magnetic fields are transverse to the direction of wave propagation, $\boldsymbol{k}$, which is parallel to the plates.

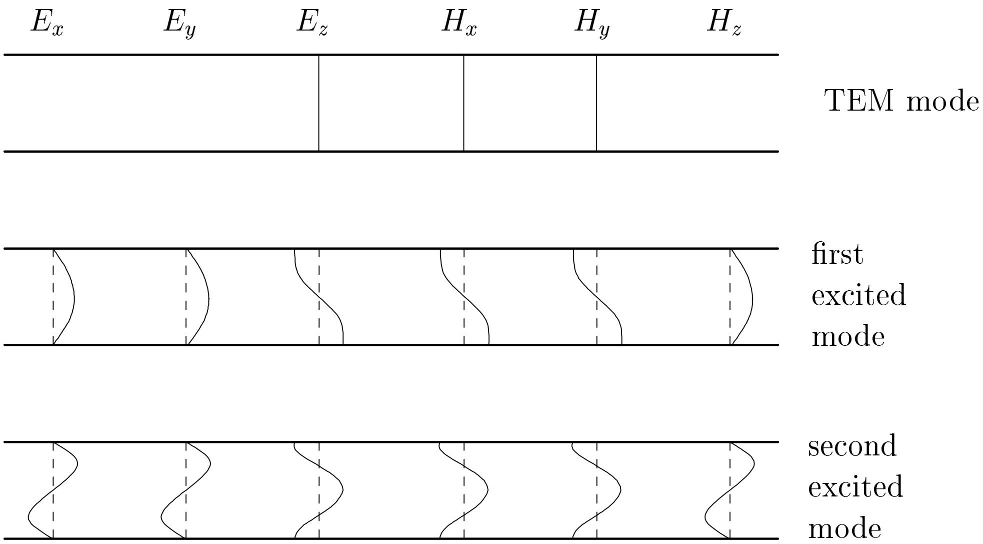

Figure 4.1: Here is shown the z-dependence of the field components for the first three modes of a parallel plate cavity. The components for which no z-dependence is shown are zero everywhere (TEM mode only).

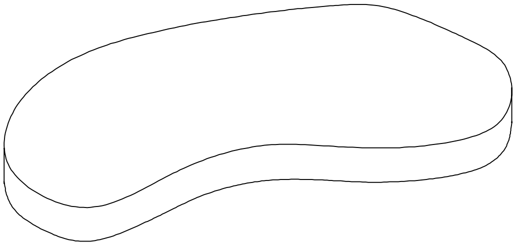

Figure 4.2: A closed two dimensional microwave cavity, or billiard.

namely E_z. However, since the boundary walls are *parallel* to this component, we must have that E_z goes to zero at the perimeter of the cavity. This is identical to the boundary condition on a quantum mechanical wavefunction ψ in a two dimensional enclosure, often called a billiard. Because both E_z and ψ satisfy the Helmholtz equation, there is a direct correspondence between the two. Thus, by studying the lowest modes of a parallel plate microwave resonator, we can gain insight about the analogous quantum mechanical billiard problem. This correspondence has been exploited by numerous authors [17, 40, 42, 43].

Now consider placing a dielectric object in the waveguide, as in Fig. 4.3. What is the boundary condition on E_z then? In general, we must have that $E_{||}$ is continuous across a dielectric interface. Since E_z is everywhere parallel to the dielectric, we must have that E_z is continuous across the surface. Now let us investigate the boundary condition on the *slope* of E_z across the dielectric surface. We know that all the components of $\boldsymbol{H}$ are continuous across a dielectric surface – only changes in the *permittivity* of a substance are important for $\boldsymbol{H}$. Now, from Eqs. 4.13, 4.14 we see that, for the TEM mode,

$$\begin{aligned} H_x &= -\frac{ic}{\omega}\frac{\partial E_z}{\partial y} &(4.15)\\ H_y &= \frac{ic}{\omega}\frac{\partial E_z}{\partial x}, &(4.16)\end{aligned}$$

because $k_z = 0$. Now, since H_x and H_y are continuous across the dielectric interface, we find that $\frac{\partial E_z}{\partial y}$ and $\frac{\partial E_z}{\partial x}$ also are continuous. This is equivalent to the continuity boundary condition on the derivative of a quantum mechanical wavefunction at a potential step. So we see that, at a particular energy, the component E_z is completely analogous to ψ, where the dielectric acts like a potential well.

However, there remains one important difference between dielectrics and quantum mechanical square wells. In quantum mechanics, the ratio of wavenumbers inside and outside the well is,

$$\frac{k_{\text{in}}}{k_{\text{out}}} = \sqrt{\frac{E-V}{E}},$$

where V is the well depth and E is the energy. Note that this ratio depends on E, and diverges at low energy. In the electromagnetic case, this ratio is a constant, and equal to the index of refraction:

$$\frac{k_{\text{in}}}{k_{\text{out}}} = \sqrt{\epsilon}.$$

This means that a system of quantum square wells can only be compared with an equivalent system of dielectric discs at a particular energy. If the energy is changed, ϵ must also be changed to retain correspondence.

4.3 Experiment

The waveguide, shown in Fig. 4.3, consisted of two parallel copper plates, 1 m square, separated by a 1 cm gap. To minimize the effect of waves reflected off the edges of the waveguide, the perimeter was lined with a 11.5 cm thick layer of microwave absorber (C-RAM LF-79, Cuming Microwave Corp.), designed to provide 20 dB of attenuation in the reflected wave intensity at frequencies above 600 MHz. Without the absorber, there

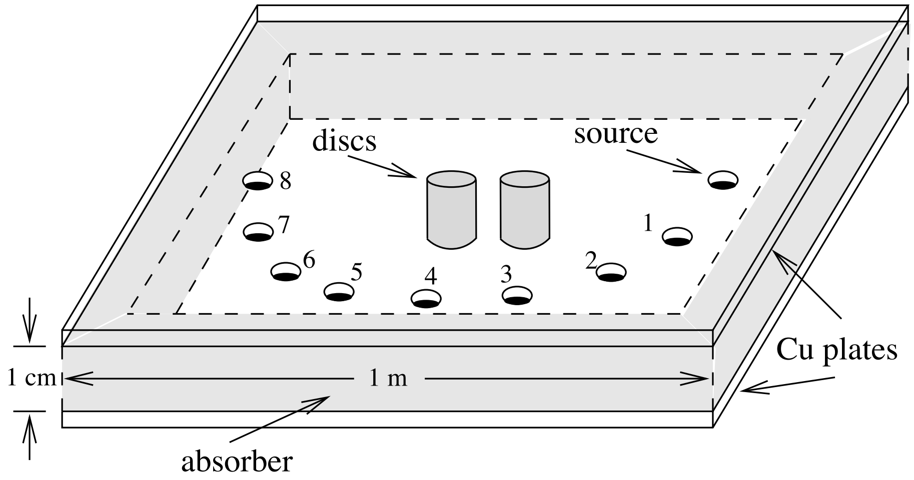

Figure 4.3: The parallel-plate waveguide used to measure the proximity resonance. Source and receiving antennae were inserted through holes drilled in the top plate. The field could be measured in any of eight locations located on a semicircle 25 cm from the discs. Note that the figure is not drawn to scale.

would be substantial reflections of both the incident and scattered wave off the edges of the waveguide, which would produce strong cavity modes and unnecessarily complicate the analysis. The important effect of the absorber was to allow the waveguide to behave as if it were infinite in extent in the directions parallel to the plates, and thus support oscillations at all frequencies.

The scatterers were cylindrical in shape (radius: 2 mm, height: 1 cm, obtained from Trak Ceramics, Hagerstown, MD.) and had a measured dielectric constant of $\epsilon = 77\pm1$. Each disc had an individual s-wave scattering resonance at 2.3 GHz with a 1.1 GHz width. They were illuminated with microwaves from a point source located 25 cm away from the midpoint of the two scatterers. The field in the waveguide could be measured at eight points located on a circle of 25 cm radius centered at the midpoint between the scatterers.

Antennae were inserted perpendicular to the plates to launch the incident wave and measure the field. Such antennae couple to the component of the electric field perpendicular to the plates. For a plate separation of 1 cm and frequencies below 15 GHz (the experiment operated between 1-3 GHz), *only* the TEM mode propagates in the waveguide, and all others are evanescent. As an example, we calculate the decay constant, $\kappa = \sqrt{k_z^2 - (\omega/c)^2}$, for the mode with one oscillation transverse to the plates at 3 GHz. With $k_z = \pi/L$ and $L = 1$ cm, we find $\kappa \simeq 3$ cm^{-1}. This means that this mode has decayed by a factor e^{-75}

over a distance of 25 cm, the distance between the source and the scatterers. Thus we may safely ignore all modes but the TEM mode for the purpose of this work.

As mentioned above, for the TEM mode both $\boldsymbol{E}$ and $\boldsymbol{H}$ are transverse to the direction of propagation, just as for a plane wave in free space. In fact, a useful visualization of this mode in the waveguide is just a section of an infinite plane wave, $\boldsymbol{E}_0 e^{i\boldsymbol{k}\cdot\boldsymbol{r}}$, with wave vector $\boldsymbol{k}$ parallel, and electric field $\boldsymbol{E}_0$ normal to the plates. Because of the correspondence of E_z for the TEM mode and a quantum mechanical wavefunction ψ, we will henceforth refer to E_z as ψ.

The measured signal was compared to the source signal in both amplitude and phase with a HP 8714C network analyzer. Because both amplitude and phase could be measured, it was possible to extract the (complex) scattered wave, ψ_s from the full signal, $\psi = \phi + \psi_s$, where ϕ is the incident wave. This was done by removing the scatterers from the waveguide and repeating the measurement, yielding ϕ. This result was then subtracted from the full wave to yield the scattered wave signal.

4.4 Two dimensional microwave scattering

The full solution to the scattering problem of a single dielectric disc in a parallel plate waveguide can be found analytically[2] [46]. The two disc problem, however, becomes difficult because of the lack of cylindrical symmetry. We address this difficulty by using a basis which reflects the broken symmetry of the problem: two sets of Bessel functions, each centered on one of the discs. This method is similar in spirit to that of Goell [16]. Referring to Fig. 4.4, we have in regions I, II, and III, respectively,

$$\begin{aligned}
\psi_I &= \sum_{l=-l_{\max}}^{l_{\max}} A_l i^l J_l(\kappa r_1) e^{il\theta_1} && (4.17)\\
\psi_{II} &= \sum_{l=-l_{\max}}^{l_{\max}} B_l i^l J_l(\kappa r_2) e^{il\theta_2} && (4.18)\\
\psi_{III} &= \phi + \sum_{l=-l_{\max}}^{l_{\max}} \left[C_l i^l H_l^{(1)}(kr_1) e^{il\theta_1} + D_l i^l H_l^{(1)}(kr_2) e^{il\theta_2} \right], && (4.19)
\end{aligned}$$

---

[2] Note that the van de Hulst solution is for scattering off an infinite dielectric cylinder in free space, with arbitrary polarization and direction of the incident wave. If the polarization is taken parallel, and the incident direction normal to the axis of the cylinder, then this solution is exactly analogous to TEM scattering in our waveguide.

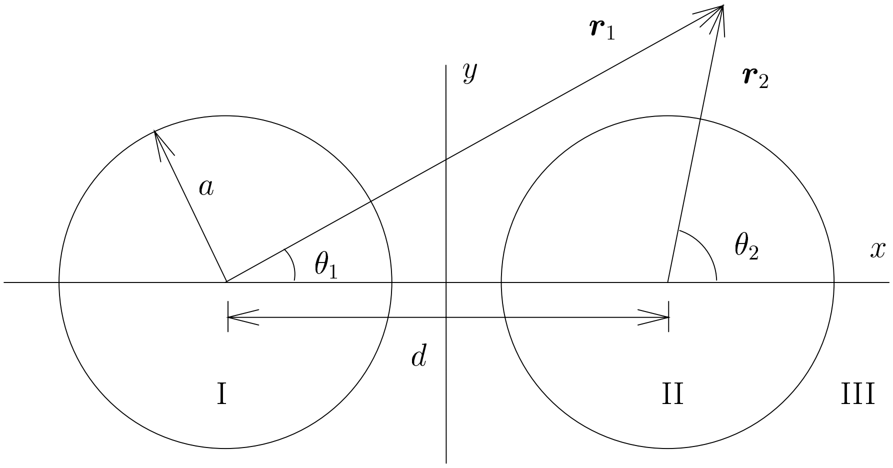

Figure 4.4: A coordinate system for two disc scattering. Each disc has radius a and they are separated by a distance d.

where $J_l(x)$ and $H_l^{(1)}(x)$ are Bessel functions and Hankel functions of the first kind, ϕ is a TEM incident wave, $\kappa = \sqrt{\epsilon}\ k$, and $l_{\max}$ determines the size of the basis set. The factor i^l is present only for future convenience. Note that the variable z does not appear in the above equations, because for the TEM mode there is no z dependence of the fields. An exact solution would require that $l_{\max} \to \infty$. However, we find very good solutions for $l_{\max}$ as small as 5. The reason only a small number of basis functions was necessary is because we are only interested in low energy scattering, where $\lambda \gg a$. In this limit, the scattered wave is *locally* s-wave around each scatterer, so that most of the solution is contained in the $l = 0$ values of the constants A_l, B_l, C_l, D_l. These complex constants are to be determined by matching ψ and its normal derivative $\partial_n \psi$ along the perimeter of each disc.

The exact solution would require matching $\{\psi, \partial_n \psi\}$ at all points along the boundary of each disc. In practice, one can only match at a finite number of points. From each matching point, one obtains two equations relating the constants A_l, B_l, C_l, D_l. The entire collection of matching equations can be expressed in matrix form, $Mx = b$, where the number of rows and columns of M is determined by the number of matching points and basis functions, respectively. The vector x is built up of the coefficients A_l, B_l, C_l, D_l, and b is determined by the incident wave ϕ. In general, one chooses more matching points than basis functions, so that the solution x minimizes the length $r = |Mx - b|$. This minimization is efficiently carried out by finding the singular value decomposition of the matrix M [18, 35].

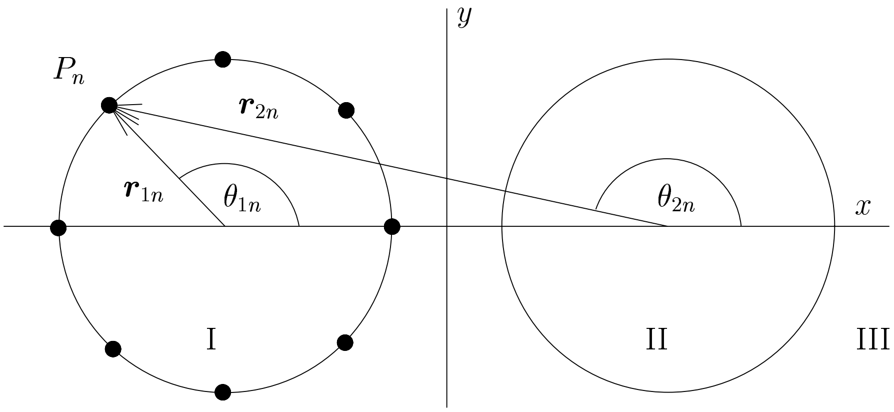

Figure 4.5: Matching points on disc I. Here we match on 8 points around the disc, and the relevant vectors are drawn for the particular matching point P_n.

The residual r provides an indication of the accuracy of the solution. For this work, typical values or r were 10^{-10} per matching point. This is to be compared with values of $|\psi|$ and $|\partial_n\psi|$ of order unity on the perimeters of the discs.

4.5 The matrix M

We will now show in detail how the matrix elements of M are computed. We will assume an incident wave $\phi = e^{i\boldsymbol{k}\cdot\boldsymbol{r}}$. As mentioned above, the solution involves matching both ψ and $\partial_n\psi$ at N points around each disc. The matching points are indictated in Fig. 4.5. Let us begin with matching ψ around disc I. Matching inside and outside solutions at the point $\boldsymbol{r}_{1n} = (a\cos\theta_{1n} - d/2, a\sin\theta_{1n})$ gives,

$$\sum_{l=-l_{\max}}^{l_{\max}} \left[A_l i^l J_l(\kappa a)e^{il\theta_{1n}} - C_l i^l H_l(ka)e^{il\theta_{1n}} - D_l i^l H_l(kr_{2n})e^{il\theta_{2n}}\right] = e^{i\boldsymbol{k}\cdot\boldsymbol{r}_{1n}}, \tag{4.20}$$

where the first term in the sum represents the wave inside I, the second is the wave scattered from I, the third is the wave scattered from II, and the exponential is the incident wave evaluated at $\boldsymbol{r}_{1n}$.

The functions r_{2n} and $e^{il\theta_{2n}}$ are complicated, since their point of reference is displaced from disc I by a distance d. Here, the angle θ_{2n} is the angle between the x-axis and the line connecting the center of disc II and the point $\boldsymbol{r}_{1n}$. Similarly, r_{2n} is the distance between the center of disc II and the point $\boldsymbol{r}_{1n}$. The forms of these functions are:

$$r_{2n} = \sqrt{a^2 + d^2 - 2ad\cos\theta_{1n}}, \tag{4.21}$$

and,

$$\begin{aligned} e^{il\theta_{2n}} &= (\cos\theta_{2n} + i\sin\theta_{2n})^l \\ &= \left(\frac{-d + a\cos\theta_{1n} + ia\sin\theta_{1n}}{\sqrt{a^2+d^2-2ad\cos\theta_{1n}}}\right)^l. \end{aligned} \tag{4.22}$$

The same procedure can be done for disc II, with very similar results. Now we match on a the set of points $\boldsymbol{r}_{2n} = (a\cos\theta_{2n} + d/2, a\sin\theta_{2n})$. The matching conditions are,

$$\sum_{l=-l_{\max}}^{l_{\max}} \left[B_l i^l J_l(\kappa a) e^{il\theta_{2n}} - D_l i^l H_l(ka) e^{il\theta_{2n}} - C_l i^l H_l(kr_{1n}) e^{il\theta_{1n}}\right] = e^{i\boldsymbol{k}\cdot\boldsymbol{r}_{2n}}, \tag{4.23}$$

where the functions r_{1n} and $e^{il\theta_{1n}}$ are now,

$$r_{1n} = \sqrt{a^2+d^2+2ad\cos\theta_{2n}}, \tag{4.24}$$

and,

$$\begin{aligned} e^{il\theta_{1n}} &= (\cos\theta_{1n} + i\sin\theta_{1n})^l \\ &= \left(\frac{d + a\cos\theta_{2n} + ia\sin\theta_{2n}}{\sqrt{a^2+d^2+2ad\cos\theta_{2n}}}\right)^l. \end{aligned} \tag{4.25}$$

It is understood that θ_{1n} is the angle between the x-axis and the line connecting the center of disc I and the point $\boldsymbol{r}_{2n}$. Similarly, r_{1n} is the distance between the center of disc I and the point $\boldsymbol{r}_{2n}$.

Eqs. 4.20, 4.23 combine to determine the matching conditions for ψ around each disc. We now must find the conditions for $\partial_n\psi$, which is more complicated because we must take the normal derivatives of the already somewhat complicated functions above. Matching $\partial_n\psi$ on disc I gives:

$$\begin{aligned} \sum_{l=-l_{\max}}^{l_{\max}} \Bigg[& A_l i^l \kappa J_l'(\kappa a) e^{il\theta_{1n}} - C_l i^l k H_l'(ka) e^{il\theta_{1n}} \qquad (4.26) \\ & -D_l \left(i^l k H_l'(kr_{2n}) e^{il\theta_{2n}} \left.\frac{\partial r_2}{\partial r_1}\right|_{\boldsymbol{r}_{1n}} + i^{l+1} l H_l(kr_{2n}) e^{il\theta_{2n}} \left.\frac{\partial \theta_2}{\partial r_1}\right|_{\boldsymbol{r}_{1n}} \right) \Bigg] = \hat{\boldsymbol{r}}_1 \cdot \nabla e^{i\boldsymbol{k}\cdot\boldsymbol{r}}\Big|_{\boldsymbol{r}=\boldsymbol{r}_{1n}}, \end{aligned}$$

where the first term is from the derivative of the wave inside disc I, the second is the from the derivative of the wave scattered from disc I, and the last two terms are from the derivative of the wave scattered from disc II. It is the derivatives appearing in these terms that are complicated. For completeness, here they are:

$$\frac{\partial r_2}{\partial r_1} = \frac{a - d\cos\theta_1}{\sqrt{a^2+d^2-2ad\cos\theta_1}} \tag{4.27}$$

$$\frac{\partial \theta_2}{\partial r_1} = \frac{-d\sin\theta_1}{a^2+d^2-2ad\cos\theta_1}. \tag{4.28}$$

The first measures the change in r_2 when r_1 is changed by a small amount, and the second measures the change in θ_2 when r_1 is changed. In Eq. 4.26, these derivatives should be evaluated on the surface of disc I. There is a similar pair of derivatives for disc II:

$$\frac{\partial r_1}{\partial r_2} = \frac{a + d\cos\theta_2}{\sqrt{a^2 + d^2 + 2ad\cos\theta_2}} \tag{4.29}$$

$$\frac{\partial \theta_1}{\partial r_2} = \frac{d\sin\theta_2}{a^2 + d^2 + 2ad\cos\theta_2}. \tag{4.30}$$

These derivatives are used in the matching condition for the slope of ψ on disc II:

$$\sum_{l=-l_{\max}}^{l_{\max}} \left[B_l i^l \kappa J_l'(\kappa a) e^{il\theta_{2n}} - D_l i^l k H_l'(ka) e^{il\theta_{2n}} \right. \tag{4.31}$$

$$\left. -C_l \left(i^l k H_l'(kr_{1n}) e^{il\theta_{1n}} \left.\frac{\partial r_1}{\partial r_2}\right|_{\boldsymbol{r}_{2n}} + i^{l+1} l H_l(kr_{1n}) e^{il\theta_{1n}} \left.\frac{\partial \theta_1}{\partial r_2}\right|_{\boldsymbol{r}_{2n}} \right) \right] = \hat{\boldsymbol{r}}_2 \cdot \nabla e^{i\boldsymbol{k}\cdot\boldsymbol{r}} \Big|_{\boldsymbol{r}=\boldsymbol{r}_{2n}}.$$

Eqs 4.20, 4.23, 4.26, 4.31 combine to form the matrix equation $Mx = b$, where the vector x is made up of the coefficients A_l, B_l, C_l, D_l, and b is a vector determined by the value and slope of the incident wave evaluated on the perimeter of each disc. The elements of M can be read off from these four matching condition equations.

4.6 Partial wave expansion

In this section, I will derive a simple expression for the partial wave amplitudes for the wave scattered by the two discs involving the coefficients C_l, D_l. With this expansion, all the partial waves may be conveniently separated and studied.

Outside the discs, the scattered wave takes the form,

$$\psi_{sc} = \sum_{l=-l_{\max}}^{l_{\max}} \left(i^l C_l H_l(kr_1) e^{il\theta_1} + i^l D_l H_l(kr_2) e^{il\theta_2} \right). \tag{4.32}$$

The scattering amplitude only has meaning for distances large compared with the size of the scattering system, that is, in the asymptotic region. For the two discs, this means $r_1, r_2 \gg d$. In this limit, we have,

$$\begin{aligned} r_1 &= \sqrt{\left(x + \frac{d}{2}\right)^2 + y^2} \\ &\approx r + \frac{d}{2}\cos\theta, \end{aligned} \tag{4.33}$$

and,

$$\begin{aligned} r_2 &= \sqrt{\left(x - \frac{d}{2}\right)^2 + y^2} \\ &\approx r - \frac{d}{2}\cos\theta, \end{aligned} \tag{4.34}$$

where θ is the angle between the x-axis and the point of observation. Similarly, we can take the asymptotic forms of the Hankel functions in the scattered wave:

$$H_l(kr) \rightarrow \sqrt{\frac{2}{\pi kr}} e^{ikr - i\pi l/2 - i\pi/4}. \tag{4.35}$$

With these asymptotic expressions, and taking $\theta_1, \theta_2 \rightarrow \theta$, the scattered wave becomes,

$$\psi_{sc} \rightarrow \sqrt{\frac{2}{i\pi kr}} e^{ikr} \sum_{l=-l_{\max}}^{l_{\max}} \left(C_l e^{-\frac{ikd}{2}\cos\theta + il\theta} + D_l e^{\frac{ikd}{2}\cos\theta + il\theta} \right), \tag{4.36}$$

so that the scattering amplitude is,

$$f(\theta) = \sqrt{\frac{2}{i\pi k}} \sum_{l=-l_{\max}}^{l_{\max}} \left(C_l e^{-\frac{ikd}{2}\cos\theta + il\theta} + D_l e^{\frac{ikd}{2}\cos\theta + il\theta} \right). \tag{4.37}$$

We now wish to decompose this scattering amplitude into partial waves:

$$f(\theta) = \sum_{l=-\infty}^{\infty} f_l e^{il\theta}. \tag{4.38}$$

This can be achieved by multiplying both sides of Eq. 4.37 by $e^{-il'\theta}$ and integrating $0 \rightarrow 2\pi$. We find,

$$\begin{aligned} f_{l'} &= \frac{1}{2\pi} \int_0^{2\pi} f(\theta) e^{-il'\theta} \\ &= \frac{1}{2\pi} \sqrt{\frac{2}{i\pi k}} \sum_{l=-l_{\max}}^{l_{\max}} \int_0^{2\pi} \left(C_l e^{-\frac{ikd}{2}\cos\theta + i(l-l')\theta} + D_l e^{\frac{ikd}{2}\cos\theta + i(l-l')\theta} \right). \end{aligned} \tag{4.39}$$

As a final step, we use one of the integral representations of the Bessel function:

$$J_l(x) = \frac{i^l}{2\pi} \int_0^{2\pi} e^{-ix\cos\theta - il\theta} d\theta. \tag{4.40}$$

With this form substituted into Eq. 4.39, we find for the partial wave amplitudes,

$$f_l = \sqrt{\frac{2}{i\pi k}} \sum_{l'=-l_{\max}}^{l_{\max}} J_{l-l'}(kd/2) \left(C_{l'} (-i)^{l-l'} + D_{l'} i^{l-l'} \right). \tag{4.41}$$

Now, once the coefficients C_l, D_l have been determined numerically, we have a convenient expression for studying each partial wave separately. This is particularly nice when looking for the proximity resonance, since it occurs exclusively in the p-wave for two scatterers.

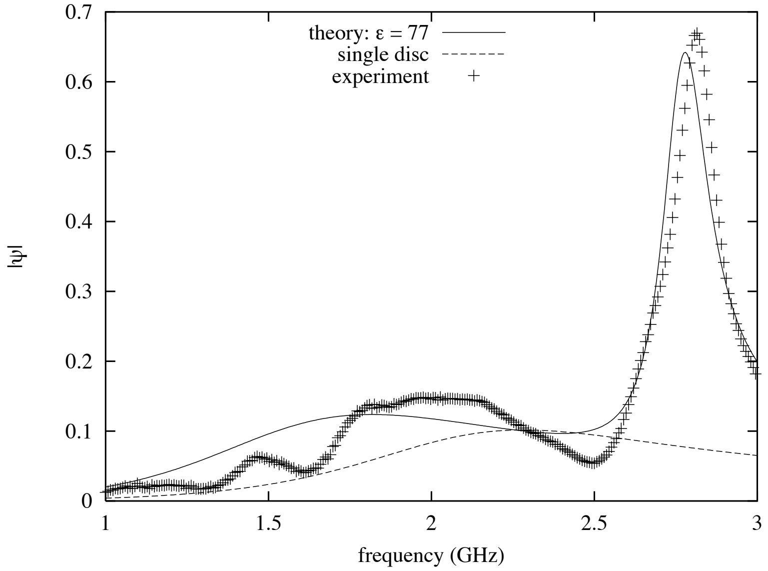

Figure 4.6: Here we plot the scattered amplitude at position 7 versus frequency. Comparison between theoretical (solid line) and experimental data (crosses). Disc separation: 1.0 cm. The single disc resonance also shown (dashed line).

4.7 Results

In Fig. 4.6 we plot the scattered amplitude $|\psi_s| = |\psi - \phi|$ measured at position 7 (see Fig. 4.3). The theoretical result agrees very well, apart from a weak 0.3 GHz modulation of the experimental signal due to reflections off the absorbing walls of the waveguide. The numerical data was generated using $l_{\max} = 5$ and matching at 10 equally spaced locations around each disc. The broad feature centered around 2.0 GHz is the s-wave (in phase) resonance. A strong proximity resonance is apparent at around 2.8 GHz. The width of this peak is smaller by a factor of seven than the single scatterer s-wave resonance width. We also checked that this peak was indeed p-wave in character by measuring the angular dependence of the scattered wave in the vicinity of 2.8 GHz. Notably, the peak was absent when the measuring antenna was placed on the line equidistant from each disc, which defines a nodal line of the scattered wave for a p-wave resonance.

In Figs. 4.7, 4.8 we plot the peak position and width, respectively, of the proximity resonance as a function of disc separation. Again the numerical predictions are in good agreement with the data. For comparison, we also include the predictions of the point scatterer model, using as input parameters a single scatterer resonance frequency $f_0 = 2.3$ GHz and width of $\Gamma_0 = 1.1$ GHz. It can be shown that within this model, the proximity

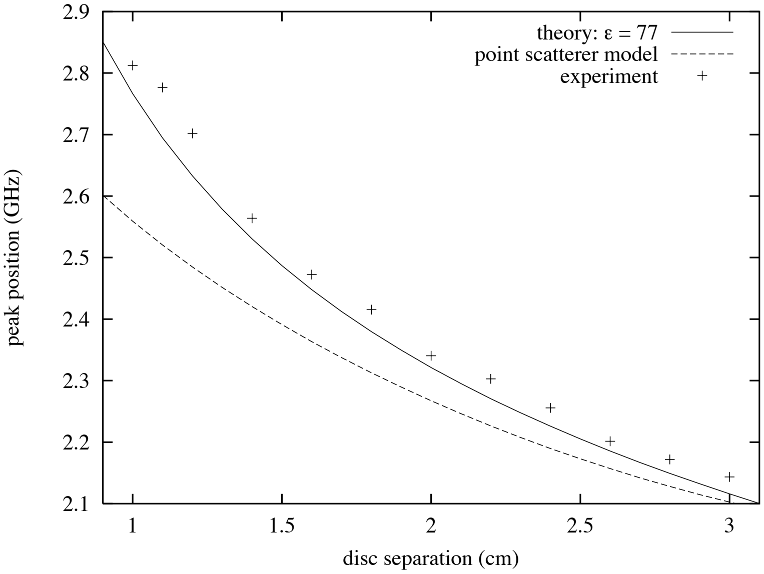

Figure 4.7: Here we plot the position of the proximity resonance peak versus disc separation. The theoretical curve (solid line) tracks the experimental values well (crosses). The point scatterer model prediction is also shown (dashed line).

resonance peak position f and width Γ obey the following formulae (see Chapter 3),

$$f = f_0 - \frac{\Gamma_0}{2} Y_0(k_0 d) \tag{4.42}$$

$$\Gamma = \Gamma_0 \left(1 - J_0(k_0 d)\right), \tag{4.43}$$

where J_0 is a zeroth order Bessel function, Y_0 is a zeroth order Neumann function, k_0 is the on-resonance wave number of a single scatterer, and d is the distance between the scatterers. The point scatterer model does a reasonable job of tracking the peak positions, but the resonance widths are not described well by the model.

4.8 Measuring the dielectric constant

In all the above calculations, the dielectric constant of the discs is an input parameter. Although the company that supplied the dielectric material gave a value for ϵ, we thought it prudent to independently measure it. For this purpose, a small cavity was made, shown in Fig. 4.9. It consisted of a cylindrical hole 2.54 cm in diameter, machined into a block of oxygen free high conductivity (OFHC) copper, with a matching copper lid. The depth of the hole was equal to the height of a disc. A disc was placed into the center

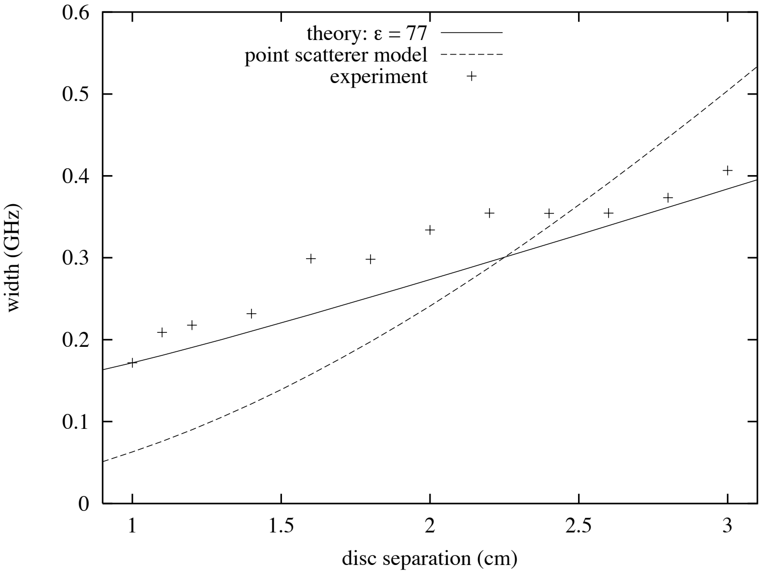

Figure 4.8: Here we plot the width of the proximity resonance versus disc separation. As above, the theoretical curve (solid line) models the experimental data (crosses) well. The point scatterer model prediction is also shown (dashed line).

of the cavity, and then the lid was screwed down tight to close the cavity. Microwaves were coupled into the cavity with short antennae as shown in the figure. A cross section of the lowest mode of such a cavity is shown in Fig. 4.10. As above, E_z plays the role of a wavefunction, where the z-axis is along the axis of the disc. Notice the greater curvature of the wavefunction in the dielectric region. The symmetric s-wave modes of the cavity shown in Fig. 4.10 can easily be computed. Inside the dielectric, the solution is,

$$E_z^{\text{in}}(r) = AJ_0(\sqrt{\epsilon}kr), \tag{4.44}$$

whereas outside the dielectric we have,

$$E_z^{\text{out}}(r) = BJ_0(kr) + CY_0(kr). \tag{4.45}$$

where $k = \omega/c$. The Neumann function $Y_0(x)$ is not allowed in the dielectric region because the solution must be finite at $r = 0$. The constants A, B, C are determined through the boundary conditions,

$$\begin{aligned} E_z^{\text{in}}(a) &= E_z^{\text{out}}(a) && (4.46)\\ \left.\frac{\partial E_z^{\text{in}}(r)}{\partial r}\right|_{r=a} &= \left.\frac{\partial E_z^{\text{out}}(r)}{\partial r}\right|_{r=a} && (4.47)\\ E_z^{\text{out}}(R) &= 0, && (4.48) \end{aligned}$$

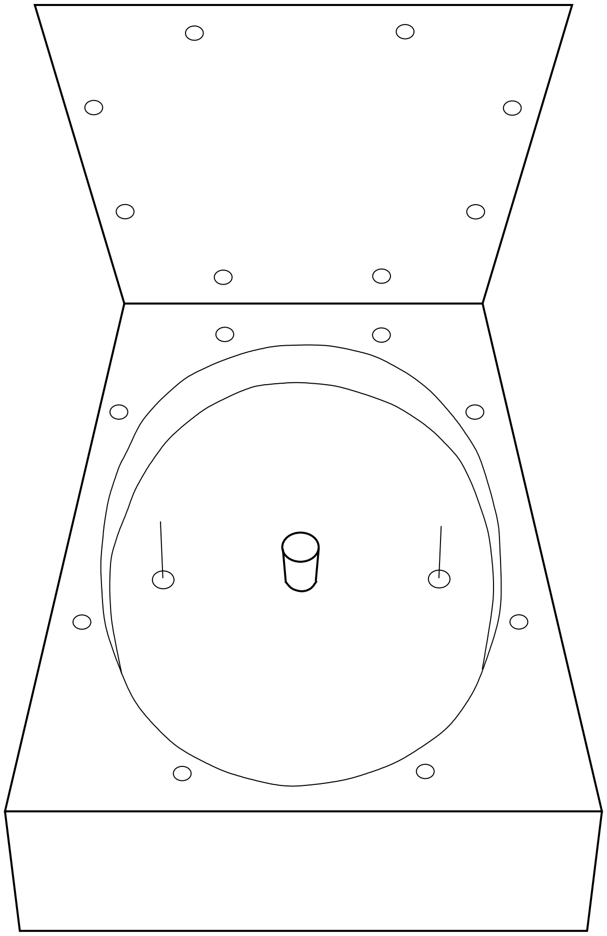

Figure 4.9: The cavity used for measuring the dielectric constant of the discs.

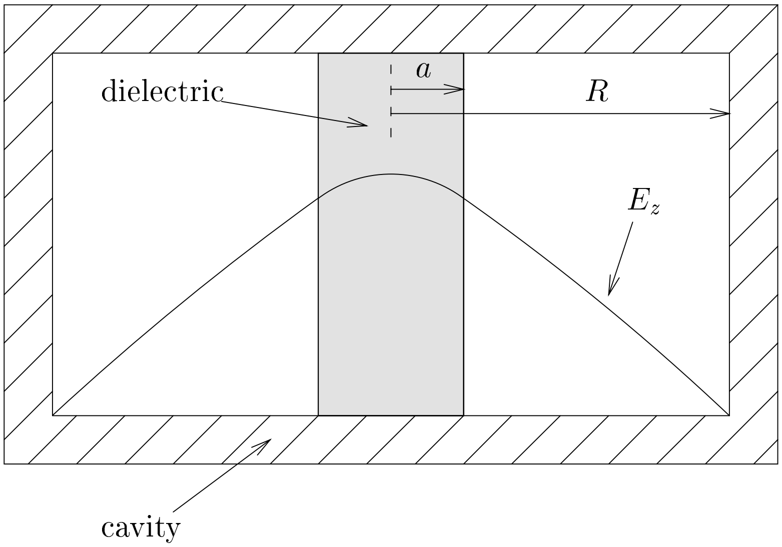

Figure 4.10: A cross section of the lowest mode of the cavity used to measure the dielectric constant. The full mode profile is formed by rotating the figure about the axis of symmetry. Note the greater curvature of E_z in the dielectric region. For simplicity the holes for inserting the antennae are not shown.

where a is the radius of the disc and R is the radius of the cavity. These three condtions combine to give a matrix equation for A, B, C:

$$\begin{pmatrix} J_0(\sqrt{\epsilon}ka) & -J_0(ka) & -Y_0(ka) \\ \sqrt{\epsilon}J_0'(\sqrt{\epsilon}ka) & -J_0'(ka) & -Y_0'(ka) \\ 0 & J_0(kR) & -Y_0(kR) \end{pmatrix} \begin{pmatrix} A \\ B \\ C \end{pmatrix} = 0 \tag{4.49}$$

These equations can only be simultaneously solved when the determinant of the matrix is zero. Thus, finding the eigenfrequencies of the cavity reduces to finding the values of k for which the above determinant is zero. A sequence of such eigenvalues, determined as a function of ϵ, can then be compared with the experimentally measured resonance frequency of the cavity to determine ϵ. An experimentally measured spectrum of the cavity is shown in Fig. 4.11. The resonance frequency of the cavity is found by measuring the transmission from one antenna to the other as a function of frequency. The measured resonance frequency 2.62 GHz is found to correspond to a dielectric constant of $\epsilon = 77$. The quality factor of this resonance is $Q = f_0/\Delta f = 1050$, where f_0 is the resonance frequency, and Δf is the width of the resonance. The cavity could be used as a high-Q notch filter.

It is interesting to note that without the presence of the disc in the cavity, the cavity would have its first resonance at the much higher frequency of 9.03 GHz. This is

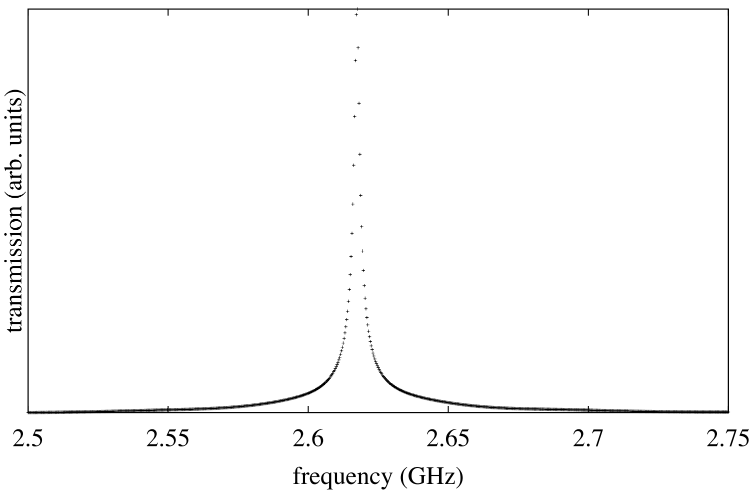

Figure 4.11: Experimentally measured transmission of the cavity pictured in Fig. 4.10.

simply determined by setting $J_0(ka) = 0$. Alternatively, in order to make an empty cavity with a resonance at 2.62 GHz, it would need a diameter of 8.8 cm, as opposed to 2.5 cm. So the inclusion of high ϵ dielectrics into filter designs allows them to be much smaller, which is why they are used today in the cellular phone industry. It is the high curvature of the fields in the dielectric which allow such cavities to support resonances at frequencies which would otherwise be much to low.

In summary, we have, for the first time, observed proximity resonances in a two dimensional system. The analysis of the experimental data seems to be well supported by a numerical solution to the scattering problem. Immediate extensions of the ideas presented here include increasing the number of scatterers to look for even narrower resonances, which would be associated with higher angular momentum scattered waves (d-waves, for example). The spectrum of a dense (compared to a wavelength), ordered array of s-wave resonant scatterers is also an interesting system as it relates to band structure formation.

I am grateful to Paul Horowitz for his advice on microwave techniques, and especially for use of his network analyzer, which he so generously offered. I also thank John Doyle for suggesting to me during my qualifying exam that I, a theorist, actually try this experiment.

Chapter 5

Threshold Resonances in a Double Well System

5.1 Introduction

In this chapter we will discuss another type of scattering resonance that occurs in the extreme quantum limit: the threshold resonance. This type of resonance occurs when a bound level approaches threshold and crosses into the continuum as some system parameter is varied. In the context discussed here, the system is two square wells, and the parameter to be varied is their separation.

Recently, the scattering of a particle on two resonant s-wave scatterers placed near one another was discussed [20]. A narrow resonance in the p-wave cross section of the combined system was shown to appear when the scatterers were placed within one wavelength of each other. This resonance was named the "proximity resonance" (see Chapter 3). It is closely related to Dicke sub-radiance[9]. The existence of proximity resonances has since been verified experimentally in the context of microwave scattering in a parallel plate waveguide (see Chap. 4, and also [21]).

Szmytkowski has considered the scattering of a particle off of two non-resonant point scatterers, and found a resonance in the p-wave cross section at zero energy when the scatterers were placed exactly one scattering length, a, apart [44]. Szmytkowski suggested this effect is a proximity resonance produced by *non-resonant* point scatterers. However, the behavior of this resonance versus the distance between the scatterers differs greatly from the behavior of the proximity resonance found by Heller. For example, the resonance produced by two *resonant* scatterers becomes *narrower* as the scatterers move closer together. Conversely, the resonance produced by two *non-resonant* scatterers *broadens* as the scatterers move closer together than a, and it *disappears completely* if the separation is greater than a. Clearly, the mechanism at work in producing these resonances is different for the two cases.

The point scatterer model, when used with non-resonant scatterers, is designed to mimic the behavior of a real potential well with a bound or virtual state close the continuum [8, 10, 37]. With this in mind, we considered the problem of two square wells in three dimensions, with their parameters chosen such that one well would have a single level very close to threshold. Now, the energy spectrum of the combined system will have two states: one that is symmetric about the midpoint between the wells, and another that is antisymmetric. As is well known, the symmetric state has a lower energy than the unperturbed level of the single well, and the antisymmetric state has a higher energy. Furthermore, the closer the wells are, the greater is the energy splitting between the symmetric and antisymmetric states. Now, remembering that the unperturbed energy of the single well is close to threshold, there will be some particular distance between the wells where the energy of the antisymmetric state is pushed all the way up to threshold and enters the continuum. It is at exactly this distance that the p-wave zero energy scattering resonance appears. This release of the antisymmetric level has been discussed previously in the literature [3, 8]. So we find that this resonance is not a proximity resonance as defined by Heller, but rather is associated with a virtual level of the double well system, and is dependent on the fact that the single well has a bound state close to threshold. Therefore we refer to this resonance as a *threshold resonance*.

5.2 Double well scattering

To make these ideas quantitative, we solved the scattering problem of two square wells in three dimensions using a method very similar to that presented in Chapter 4. Each well has a depth V and radius r_0, and they are separated by the center-to-center distance d. The method involves the use of a basis which reflects the broken symmetry of the problem: two sets of spherical Bessel functions, each centered about one of the wells. Referring to Fig. 5.1, we have in regions I, II, and III, respectively,

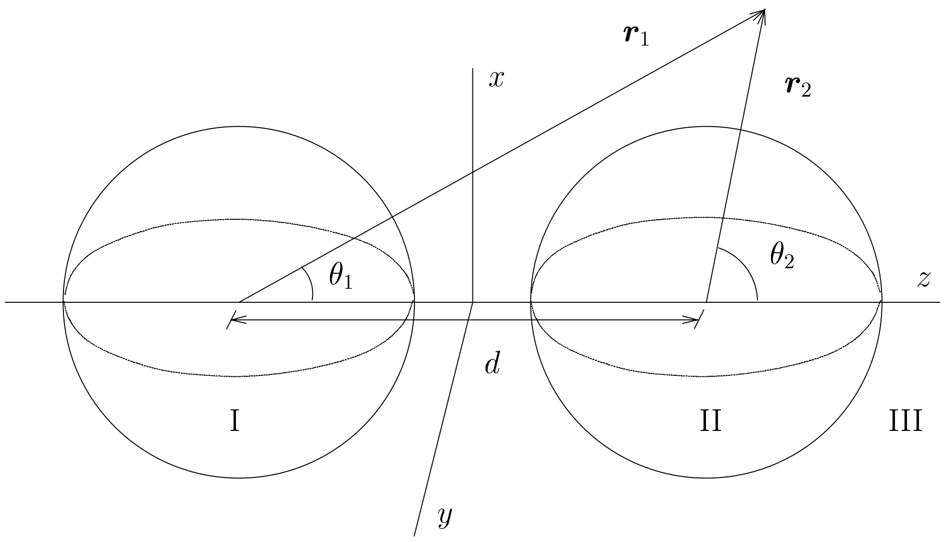

Figure 5.1: A coordinate system for double well scattering.

$$\begin{aligned}
\psi_I &= \sum_{l=0}^{l_{\max}} A_l j_l(\kappa r_1) P_l(\cos\theta_1), &(5.1)\\
\psi_{II} &= \sum_{l=0}^{l_{\max}} B_l j_l(\kappa r_2) P_l(\cos\theta_2), &(5.2)\\
\psi_{III} &= e^{ikz} + \sum_{l=0}^{l_{\max}} \left[C_l h_l^{(1)}(kr_1) P_l(\cos\theta_1) + D_l h_l^{(1)}(kr_2) P_l(\cos\theta_2)\right], &(5.3)
\end{aligned}$$

where $j_l(x)$ and $h_l^{(1)}(x)$ are spherical Bessel functions and spherical Hankel functions of the first kind, $P_l(x)$ is a Legendre polynomial, $k = \sqrt{2E}$, $\kappa = \sqrt{2(E-V)}$, and $l_{\max}$ determines the size of the basis set. For the purposes of this work it is sufficient to consider incident waves with wave vector $\boldsymbol{k}$ parallel to the line connecting the centers of the two wells. Then the solution will have azimuthal symmetry and it is not necessary to include a term $e^{im\phi}$ in the basis functions, since $m = 0$ for azimuthally symmetric solutions.

Finding the solution involves matching ψ and its normal derivative, $\partial_n \psi$, along the perimeter of each well corresponding to $\phi =$ constant. The matching conditions can be expressed as a matrix equation, $Mx = b$, where x is a vector containing the coefficients A_l, B_l, C_l, D_l, and b is determined by the incident wave. The matrix M is determined through the matching conditions. The method of solution is entirely analogous to that presented in Chapter 4, and will not be repeated here.

5.3 Partial wave expansion

As in Chapter 4, the partial wave amplitudes f_l can be related in a simple way to the coefficients C_l, D_l, and thus all relevant partial waves can be separated and studied. In this section, I will derive this expansion.

In the region outside of the wells, the scattered wave is,

$$\psi_s = \sum_{l=0}^{l_{\max}} \left(C_l h_l^{(1)}(kr_1) P_l(\cos\theta_1) + D_l h_l^{(1)}(kr_2) P_l(\cos\theta_2) \right). \tag{5.4}$$

In the asymptotic region, we may make the following approximations:

$$\begin{aligned} \theta_1 &\approx \theta & (5.5)\\ \theta_2 &\approx \theta & (5.6)\\ r_1 &\approx r + \frac{d}{2}\cos\theta & (5.7)\\ r_2 &\approx r - \frac{d}{2}\cos\theta & (5.8)\\ h_l^{(1)}(kr) &\approx \frac{e^{ikr - il\pi/2 - i\pi/2}}{kr}. & (5.9) \end{aligned}$$

Substituting these asymptotic expressions, we have for the scattered wave,

$$\psi_s \approx -\frac{ie^{ikr}}{kr} \sum_{l=0}^{l_{\max}} \left(C_l (-i)^l e^{-\frac{ikd}{2}\cos\theta} P_l(\cos\theta) + D_l (-i)^l e^{\frac{ikd}{2}\cos\theta} P_l(\cos\theta) \right), \tag{5.10}$$

so that the scattering amplitude is,

$$f(\theta) = -\frac{i}{k} \sum_{l=0}^{l_{\max}} (-i)^l P_l(\cos\theta) \left(C_l e^{-\frac{ikd}{2}\cos\theta} + D_l e^{\frac{ikd}{2}\cos\theta} \right). \tag{5.11}$$

The partial wave expansion is given by,

$$f(\theta) = \sum_{l=0}^{\infty} f_l (2l+1) P_l(\cos\theta). \tag{5.12}$$

We can extract the partial wave amplitudes by multiplying both sides of Eq. 5.11 by $P_{l'}(\cos\theta)$ and integrating over $\cos\theta$. We find,

$$\begin{aligned} f_l &= \frac{1}{2} \int_{-1}^{1} f(\theta) P_l(\cos\theta)\; d\cos\theta \\ &= -\frac{i}{2k} \sum_{l=0}^{l_{\max}} (-i)^{l'} \left(C_{l'} \int_{-1}^{1} e^{-ikdx/2} P_l(x) P_{l'}(x)\; dx \right. \\ &\qquad \left. + D_{l'} \int_{-1}^{1} e^{ikdx/2} P_l(x) P_{l'}(x)\; dx \right). \end{aligned} \tag{5.13}$$

To do the integrals, we will need the following relation between the Legendre polynomials [7, pg. 1046]:

$$P_{l_1}(x)P_{l_2}(x) = \sum_{l=|l_1-l_2|}^{l_1+l_2} \langle l_1\ l_2\ 0\ 0|l\ 0\rangle^2 P_l(x), \tag{5.14}$$

where $\langle l_1\ l_2\ m_1\ m_2|l\ m\rangle$ is a Clebsch-Gordan coefficient. So we have for the integral,

$$\begin{aligned} I_{ll'} &= \int_{-1}^{1} e^{ikdx/2} P_l(x)P_{l'}(x)\ dx \\ &= \sum_{n=|l-l'|}^{l+l'} \langle l\ l'\ 0\ 0|n\ 0\rangle^2 \int_{-1}^{1} e^{ikdx} P_n(x)\ dx. \end{aligned} \tag{5.15}$$

Now we use one of the integral representations of the spherical Bessel function,

$$j_n(z) = \frac{(-i)^n}{2} \int_{-1}^{1} e^{izx} P_n(x)\ dx. \tag{5.16}$$

Then Eq. 5.15 becomes,

$$I_{ll'} = 2 \sum_{n=|l-l'|}^{l+l'} i^n j_n(kd/2) \langle l\ l'\ 0\ 0|n\ 0\rangle^2, \tag{5.17}$$

and the partial wave amplitudes are:

$$f_l = -\frac{i}{2k} \sum_{l'=0}^{l_{\max}} (-i)^{l'} \left(C_{l'} I_{ll'}^* + D_{l'} I_{ll'} \right). \tag{5.18}$$

The partial wave cross sections are

$$\sigma_l = 4\pi(2l+1)|f_l|^2. \tag{5.19}$$

With the convenient decomposition given by Eq. 5.18, all relevant partial waves can be trivially computed, given the coefficients C_l, D_l.

5.4 Double well bound states

The *bound* states of the double well system can be found in an similar manner, using the modified spherical Bessel functions, $k_l(kr)$, outside the wells instead of outgoing waves:

$$\psi_{III} = \sum_{l=0}^{l_{\max}} C_l \left[k_l(kr_1) P_l(\cos\theta_1) \pm k_l(kr_2) P_l(\cos\theta_2) \right]. \tag{5.20}$$

where $k = \sqrt{-2E}$ and we have exploited the fact that the bound states must have definite parity on reflection about the xy plane. Similarly, $B_l = \pm A_l$ in Eqs. 5.1, 5.2. Here the upper sign is for the states which are even about the y-axis, and the lower sign is for the odd states. Also, in looking for bound states, the matrix problem reduces to finding the nullspace of M, or $Mx = 0$, since there is no incident wave.

5.5 Results

In Fig. 5.2 we plot the p-wave cross section versus energy for various values of the well separation. The parameters characterizing a single well were $r_0 = 1$, $V = -1.24374$. For these values, the unperturbed energy level and scattering length of the single well were $E = -.00005$ and $a = 100$. The bound state energy and scattering length are related by $E = -1/2a^2$. Note that the p-wave cross section at $d = 101$, when the wells are slightly more than one scattering length distant from each other, is relatively featureless. However, changing the distance between the wells by only 1%, from 101 to 100, changes the on-resonance p-wave cross section by nearly *four* orders of magnitude. It is at exactly this point where the antisymmetric level of the two wells enters the continuum and becomes a virtual level, which then couples strongly to the $E > 0$ incident wave. As the wells move nearer, the virtual level moves up in energy, and thus becomes more and more “virtual,” as is indicated by the broadening of the threshold resonance for smaller values of d.

The picture is even more clear in Fig. 5.3, where we plot the energy levels for $E < 0$, and position of the threshold resonance for $E > 0$, versus d. One clearly sees the crossing of the antisymmetric level into the continuum at $d = a = 100$, and the curve representing the position of the threshold resonance joins smoothly with the energy level curve at this point. We have added vertical bars on the curve for $E > 0$ to indicate the resonance width. For comparison, we have also plotted the results of the point scatterer model, used by Szmytkowski, which predicts that the energy levels and scattering resonances of the two-center system satisfy (see Chapter 3),

$$1 - \frac{f^2}{d^2} e^{2ikd} = 0, \tag{5.21}$$

with $E = k^2/2$, and the single point scatterer scattering amplitude, f, is given by,

$$f = \frac{-a}{1 + ika}. \tag{5.22}$$

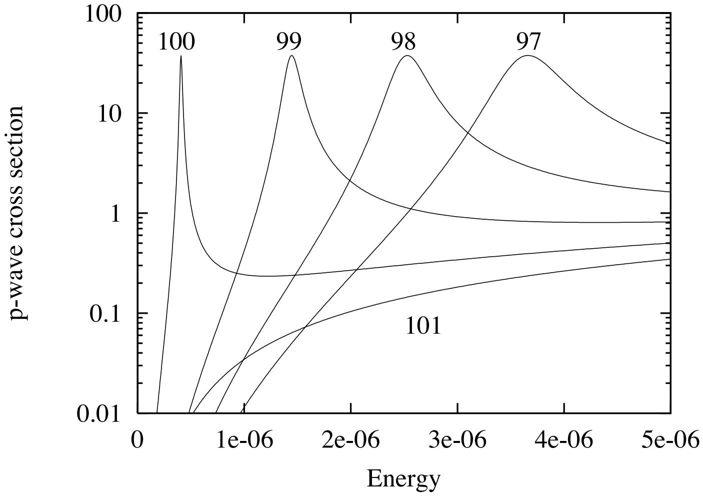

Figure 5.2: P-wave cross section versus energy for various well separations, d = 97, 98, 99, 100, and 101. Note the change in the on-resonance cross section by nearly four orders of magnitude as the separation goes from a to $1.01a$.

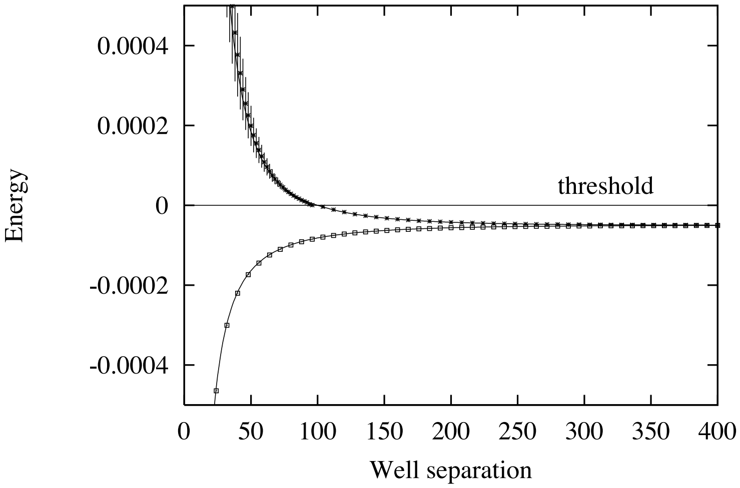

Figure 5.3: Energy levels for the even state (lower curve, points), odd state (upper curve, $E < 0$, points), and the threshold resonance (upper curve, $E > 0$, points) versus well separation. The well parameters were chosen such that the unperturbed single well had a scattering length of 100. The width of the virtual state is indicated by vertical bars. For comparison, the results of the point scatterer model are also shown (lines).

The bound states and scattering resonances are determined by the roots of Equation 5.21 in the complex E plane, where the real part of the root corresponds to a resonance energy, and the imaginary part to the resonance width. Real roots correspond to bound states of the two-center system. One can show that both roots of Equation 5.21 are real and negative when $d > a$; in this region both the symmetric and antisymmetric states are bound. For $d < a$, only the symmetric state remains bound, as can be seen from Fig. 5.3. The agreement between the point scatterer model and the full theory is striking. We emphasize that these results indicate that the point scatterer model accurately represents the square wells even when $d < a$. Only when d approaches r_0 does the point scatterer model become inaccurate.

In looking at Fig. 5.3 one is reminded of Born-Oppenheimer potential curves for the binding of two weakly interacting atoms by a shared electron. The lower curve is analogous to the bonding state, and the upper to the anti-bonding state. In a real molecule, however, there is a hard core repulsion at small values of the separation of the two nuclei which causes the potential curve of the bonding state to turn over, rather than descending to ever lower energies. Of course, this behavior is not present in the double well system, because the wells have no mutual interaction.

5.6 Efimov and Thomas Effects

We have found the system of two heavy particles interacting with a third light particle ideal for simple explanations of both the Efimov [12, 13] and Thomas [45] effects. Here we are thinking of the two wells as non-interacting heavy particles. Efimov found that three particles, interacting through large scattering length potentials, have an infinite number of three-body bound states at threshold as the scattering length becomes infinite. One can easily show, within the context of the point scatterer model, that the Born-Oppenheimer potential curve for the two wells behaves for large separations ($d \gg r_0$) as $V(d) \sim -1/d^2$ as $a \to \infty$. Such a potential has an infinite number of bound states at threshold, in a way similar to the Coulomb potential [32]. These states are the so-called Efimov states. It is interesting to note that if the two wells are made more attractive, the Efimov states enter the continuum, instead of becoming more bound. This is because the scattering length gets *smaller* as the wells are made more attractive.

In 1935, Thomas showed that three particles, interacting through two-body interactions with scattering length a and range r_0, possess an infinite number of three-body bound states as $r_0 \to 0$, keeping a fixed. However, in contrast to the Efimov effect, these bound states do not appear at threshold, but are in a sense *infinitely* bound; there is no ground state. This is because of the pathological nature of the inverse square potential [32]. One can show, again within the context of the point scatterer model, where the limit $r_0 \to 0$ is automatically satisfied, that the Born-Oppenheimer potential curve behaves as $V(d) \sim -1/d^2$ for $d \ll a$. It is the inverse square singularity of the heavy-heavy potential that causes the "ground state" to move off to infinite binding energy. The Thomas effect is intimately related to the "fall into the center" phenomenon discussed by Landau [28].

5.7 Disappearance of the s-wave cross section

There is another interesting property that the double well system exhibits, namely, the behavior of the low energy *s-wave* cross section, σ_0, as the wells get very near each other. One might expect that, because two wells are "more" than one, that two wells should scatter "more" than a single well. This is indeed the case, as long as $d > a$. However, as $d \to 0$, holding the energy fixed such that $ka \ll 1$, we find the surprising result that $\sigma_0 \to 0$. This can be understood by turning again to Fig. 5.3. The lower curve, corresponding to the symmetric bound state, will determine the behavior of the s-wave scattering cross section. For a single well at low energy, $\sigma_0 = 4\pi a^2$, where a is given by $E = -1/2a^2$ and E is the energy of the bound state near threshold. Thus, the farther the single level is from threshold, the smaller is σ_0 at low energy. Now, in the double well system, we see that the symmetric state is driven to lower energies as the wells approach each other. Thus the effective scattering length of the combined system, and therefore σ_0, will become smaller and smaller. This is the reason for the disappearance of σ_0 at low energies as the wells approach each other. In Fig. 5.4 we plot σ_0 versus d at fixed low energy, $|ka| = .01$, normalized to $4\pi a^2$. The wells become essentially *invisible* to the symmetric part of the incident wave as $d \to 0$. At low energy, all other partial waves are negligible compared to σ_0 and we have the result that $\sigma_{tot}/4\pi a^2 \to 0$. Furthermore, note that σ_0 for the combined system when $d = a$ is *identical* to that of a single well. This means that, for $d = a$, one well could be *removed* from the problem without affecting σ_0. Of course, σ_1 would be drastically affected by removal of one of the wells, because of the presence of the p-wave threshold resonance when $d = a$.

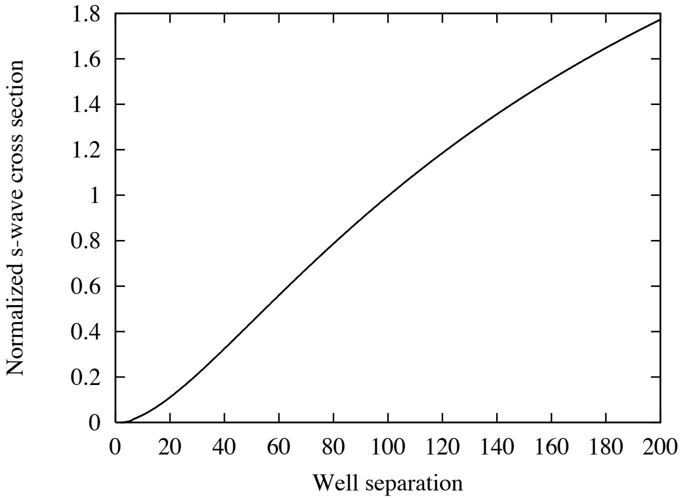

Figure 5.4: S-wave cross section versus well separation, for fixed energy $ka = .01$, normalized to $4\pi a^2$. The two wells become invisible when they are very close. Note also that σ_0 is identical with that of a single well when $d = a$.

This is a purely quantum mechanical (wave) effect, because it depends on the fact that σ_0 for the single well, $4\pi a^2$, is much larger than the visible area of the well, πr_0^2. For a classical scatterer, the cross section is just πr_0^2. Two classical square wells *always* have a larger cross section than one, even when they are right next to each other (unless, of course, the incident direction is taken parallel with the line connecting the centers of the billiard balls).

This disappearance of σ_0 has important consequences for the interesting problem of scattering in the presence of an external confining potential [33]. Here we are thinking of particles in a trap interacting with each other though potentials such that $a \gg r_0$, where r_0 is the range of the inter-particle potential. In particular, when the typical length scale of the confining potential approaches the scattering length, we expect dramatic a reduction in the s-wave cross section of a confined scatterer. As a simple model of the effect confinement has on the scattering, we imagine a single well with a level near threshold, with scattering length a, a distance d from a perfectly reflecting wall. The bound state wave function is forced to zero on the wall, so we may consider the equivalent problem of a double well system, where only the antisymmetric state is allowed. If $d \gg a/2$, the energy of the level is shifted upward slightly and the cross section of the well in the presence of the wall is mildly increased. Precisely at the point $d = a/2$, the level enters the continuum and a threshold resonance appears. Since the presence of the wall forbids the symmetric state, the well does not possess any bound states for $d < a/2$. Thus, once the virtual level has been pushed far into the continuum, i.e. for $d \ll a/2$, the scattering of the well will be *greatly* reduced from what it would have been in the absence of the wall. It is obvious that the presence of a second wall on the opposite side of the scatterer will only enhance the effect. Now, assuming that the confinement of the trap is strong enough such that $l \ll a$ is satisfied, where l is a characteristic length scale of the trap, we expect a dramatic reduction in the collision cross section for atoms in such a trap. Of course, a real trap would not have the hard walls we describe here, but it seems clear that similar effects are going to occur whenever the characteristic trapping length scale becomes less than the scattering length of a free space atom.

A further consequence of this effect may be the suppression of three body collisions in cold dense gases, such as a Bose condensate. The idea is as follows: in a normal two-body collision, the situation is often encountered that two atoms are situated within one scattering length of each other. In this circumstance, the apparent s-wave cross section of these two atoms to an incident third body will be much reduced from the single atom s-wave cross section, thus reducing the rate for three body processes.

We should emphasize here that the disappearance of the s-wave cross for the double well system is not complete. That is, there is still some scattering of the two wells in the s-wave even when they are right next to each other. The point is, the cross section is much reduced from what it would be if only one well were present. This effect is to be distinguished from the so-called Ramsauer-Townsend effect, where the cross section in a particular partial wave can become exactly zero at a particular energy [38]. This effect occurs when the phase shift for the partial wave of interest passes through a multiple of π.

5.8 Negative scattering lengths

All of the ideas presented here generalize to the case of a system of two wells, each with a *virtual* level just *above* threshold, that is, a large *negative* scattering length. In this case, when the wells are situated far from each other, there will be two virtual states, symmetric and antisymmetric. As the wells approach each other, the symmetric virtual level decreases in energy, until at a certain distance, it crosses threshold and becomes bound. In this case an *s-wave* threshold resonance will occur, in the sense that the low energy s-wave

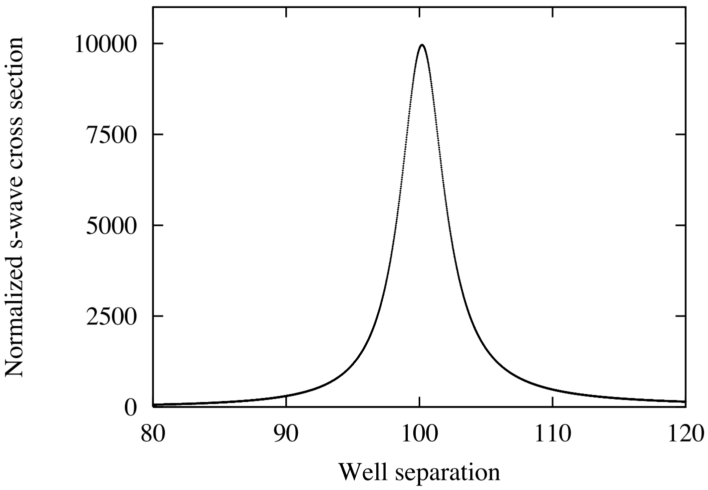

Figure 5.5: S-wave cross section versus well separation, for fixed energy $|ka| = .01$, normalized to $4\pi a^2$, with $a = -100$. The low energy s-wave cross section experiences a pronounced maximum as d passes through $-a$, where σ_0 is 10^4 times the single well value.

cross section of the combined system will experience a pronounced maximum as d passes through $-a$. The antisymmetric virtual level will increase in energy and broaden as the wells approach each other. If $|a/r_0|$ is large enough, then the s-state will drop well below threshold when the wells are very close, thus suppressing σ_0 in a manner similar to the case above. In Fig. 5.5 we plot σ_0 at fixed low energy, $ka = .01$, for a system of two wells with $a < 0$ as a function of well separation. The well parameters are $r_0 = 1$ and $V = -1.2238$, which give each well a scattering length of $a = -100$. The s-wave threshold resonance is visible when $d = -a$, where σ_0 is a factor of 10^4 greater than $4\pi a^2$.

It is important to note that all results presented here are for potential wells of finite radius r_0 and depth V, tuned such that they had a level just below or above threshold. However, there exists a well-defined limit of $r_0 \to 0, V \to -\infty$ such that the level structure of the well near threshold is unchanged. This limit is, as $r_0 \to 0$,

$$V \to E_0 - \left(\frac{\pi}{8r_0} + \frac{\sqrt{2|E_0|}}{2\pi} \right)^2 , \tag{5.23}$$

Where E_0 is the energy of the level near threshold. In this way one can construct a zero range potential of any scattering length, which is essentially equivalent to the Huang pseudopotential [22]. This is in contrast to the simple delta function potential, which does *not* scatter in three dimensions, as was shown in Chapter 2.

Finally, we note that all the effects discussed above have been observed in the *two dimensional* double well problem. However, this case is complicated by the low energy divergence of σ_0, which is caused by the low energy singularity of the 2D Green function for the Helmholtz operator. Because σ_0 diverges at low energy, we must alter our notion of the scattering length. We take a to be the radius at which the wave function $\psi = \psi_{incident} + \psi_{scattered}$ has its first node in the limit of $k \to 0$. With this definition of the scattering length, all the effects (except for the Efimov and Thomas effects [2, 29]) mentioned above appear in 2D exactly as in 3D.

5.9 Conclusions

To summarize, we have found the resonance reported by Szmytkowski to be a threshold resonance connected with the release into the continuum of an antisymmetric state of the double well system. More generally, we find the double well system ideal for studying threshold resonances, which will occur in any system of potential wells that possess levels near threshold. With more than two wells of positive scattering length, there will be a threshold resonance corresponding to each bound state of the composite system except for the symmetric state, which remains bound as the wells get close. This means there would be $N-1$ threshold resonances for a system of N wells, if a/r_0 is sufficiently large. The analogy of the energy level curves to Born-Oppenheimer potentials is an appealing one, and we plan to pursue this idea in the context of the point scatterer model. Finally, the disappearance of σ_0 as the wells get very near is a surprising result which may have application in a wide variety of systems.

Chapter 6

Higher Partial Waves in the Point Scatterer Model

6.1 Introduction

The point scatterer model has traditionally been applied to problems of low energy scattering, where the wavelength of the incoming particle is much longer than the range of the potential which the point scatterer is designed to mimic. The reason for this is that, up to now, point scatterers have been capable of scattering s-waves *only.* Now, at fixed wave number k, it is well known that one must include at least $l \approx kr_0$ partial waves to accurately describe the scattering of a potential of range r_0. Here, by "range", we mean the actual range, or the scattering length, or the square root of the on-resonance cross section, whichever is largest. At low energy, when $kr_0 \ll 1$, the point scatterer model is very accurate, but as the energy increases, it fails to accurately describe the scattering. This low energy criterion is the main limitation of the model. In the following, we describe a procedure for incorporating partial waves of any order into the point scatterer model. In principle, it is then possible to reproduce the scattering of any potential of finite range at all energies. The main benefit of this is the possibility to address the problem of multiple scattering between many non-overlapping potentials with algebraic matrix methods, rather than the coupled integral equations that one normally would be faced with in such a multiple scattering problem.

We will work almost exclusively with t-matrices. The power of the t-matrix approach with point scatterers cannot be overemphasized. The reasons for this are many. First of all, a pure delta function in two or three dimensions does *not* scatter, so that if one insists on using potentials, a more elaborate framework must be used (see Chapter 2). The point scatterer t-matrix, on the other hand, has a straightforward interpretation. Second, the equations of multiple scattering are more transparent when expressed with t-matrices. Third, the Huang pseudopotential appears to be the only potential used in the point scatter model, which mimics the behavior of a potential well with a bound or virtual state near threshold. An analog of the Huang pseudopotential modeling the behavior of a *resonant* potential, has to my knowledge not been proposed. Thus, the pseudopotential approach seems to be limited to modeling a class of interactions defined by $a \gg r_0$, where a is the scattering length and r_0 is the range of the potential one wishes to model. The t-matrix approach, however, does not suffer from this limitation, and it is straightforward to model the behavior of *any* type of potential, as long as it is of finite range.

6.2 Higher partial waves: two dimensions

For the purposes of this section, we will concentrate on the two dimensional problem. Conceptually, the three dimensional case is no more difficult, but as a practical matter it is considerably more complicated because of the extra dimension. At the end of the chapter, we will illustrate the three dimensional case.

First let's consider just a single scatterer at the origin, with incident plane wave $\phi = e^{ikx}$. As a model potential, I will consider a hard disc, defined by,

$$V(r) = \begin{cases} \infty & r < a \\ 0 & r > a \end{cases} . \tag{6.1}$$

This potential forces the full solution to zero at $r = a$. First of all, we will need the expansion of the incident wave in eigenfunctions of angular momentum:

$$e^{ikx} = J_0(kr) + \sum_{l=1}^{\infty} 2i^l J_l(kr) \cos l\theta. \tag{6.2}$$

The full solution will be expressed as,

$$\psi(\boldsymbol{r}) = e^{ikx} + \sum_{l=0}^{\infty} s^{(l)} H_l(ka) \cos l\theta, \tag{6.3}$$

where the superscripts on the Hankel functions of the first kind have been dropped. The amplitudes $s^{(l)}$ are, up to constant factors, analogs of $s(k)$ discussed in Chapter 2. They are related to the partial wave scattering amplitudes for the hard disc. Now we'll find the $s^{(l)}$.

For s-waves, the boundary condition at $r = a$ is expressed as,

$$J_0(ka) + s^{(0)} H_0(ka) = 0. \tag{6.4}$$

This is just taking the $l = 0$ term of Eq. 6.3. For higher angular momenta, the boundary condition is expressed as

$$2i^l J_l(ka) \cos l\theta + s^{(l)} H_l(ka) \cos l\theta = 0, \tag{6.5}$$

We can easily solve Eq. 6.4 and Eq. 6.5 for the $s^{(l)}$:

$$s^{(l)} = \begin{cases} \frac{-J_0(ka)}{H_0(ka)} & l = 0 \\ \frac{-2i^l J_l(ka)}{H_l(ka)} & l > 0 \end{cases} \tag{6.6}$$

With these definitions for the $s^{(l)}$, the solution for the hard disc scattering is Eq. 6.3, because the boundary condition is satisfied by construction for each partial wave.

Now, for a single point scatterer incorporating s- and p-waves at the origin, I assert that the operator product $Gt\phi$ has the position space representation,

$$\begin{aligned} Gt\phi &= \iint d\boldsymbol{r}' d\boldsymbol{r}'' \left(G^{(0)}(\boldsymbol{r}, \boldsymbol{r}') t^{(0)}(\boldsymbol{r}', \boldsymbol{r}'') + G^{(1)}(\boldsymbol{r}, \boldsymbol{r}') t^{(1)}(\boldsymbol{r}', \boldsymbol{r}'') \right) \phi(\boldsymbol{r}'') \\ &= s^{(0)} H_0(kr) \phi(0) + s^{(1)} H_1(kr) \frac{1}{ikr} \boldsymbol{r} \cdot \nabla' \phi(\boldsymbol{r}')|_{\boldsymbol{r}'=0}, \end{aligned} \tag{6.7}$$

where the first term is the scattered s-wave, and the second term is the scattered p-wave. In order to understand this equation, let us investigate the action of the operator

$$D^{(1)} = \frac{1}{ikr} \boldsymbol{r} \cdot \nabla'|_{\boldsymbol{r}'=0} \equiv \frac{1}{ikr} r_\alpha \frac{\partial}{\partial r_\alpha} \tag{6.8}$$

on the plane wave state e^{ikx}:

$$\frac{1}{ikr} \boldsymbol{r} \cdot \nabla' e^{ikx'}|_{x'=0} = \frac{1}{ikr} \boldsymbol{r} \cdot \hat{x} ik = \hat{r} \cdot \hat{x} = \cos\theta. \tag{6.9}$$

Now, inserting this result into Eq. 6.7 and comparing with Eq. 6.3, we find that Eq. 6.7 accurately represents the scattered wave from a single hard disc at the origin up to $l = 1$.

To incorporate higher partial waves than $l = 1$, we need the trigonometry identities for $\cos l\theta$:

$$\cos 2\theta = 2\cos^2\theta - 1 \tag{6.10}$$

$$\cos 3\theta = 4\cos^3\theta - 3\cos\theta \tag{6.11}$$

$$\vdots$$

These polynomials in $\cos\theta$ are analogous to the Legendre polynomials that appear in the three dimensional angular momentum eigenfunctions.

The differential operator analogous to D producing $\cos 2\theta$ when operating on a plane wave involves second rank tensors:

$$D^{(2)} = \frac{1}{(ikr)^2}\left(2r_\alpha r_\beta \frac{\partial}{\partial r_\alpha}\frac{\partial}{\partial r_\beta} - r^2\nabla^2\right). \tag{6.12}$$

Here and everywhere I will use the Einstein convention: repeated indices are summed over. Later on I will present a rigorous method for finding these differential operators which, when acting on a generalized incident wave, give the proper angular dependence of the scattered wave.

So how do these tensors relate to the corresponding Green functions and t-matrices to give the scattered wave? Consider the following equation for the p-wave "Green function,"

$$(\nabla^2 + k^2)G^{(1)}(\boldsymbol{r} - \boldsymbol{r}') = \hat{\boldsymbol{r}}_0 \cdot \nabla\delta(\boldsymbol{r} - \boldsymbol{r}'). \tag{6.13}$$

This is an equation for a peculiar Green function. It does not have a delta function source, but rather a *dipole* delta function source at $\boldsymbol{r} = \boldsymbol{r}'$, oriented in the direction $\hat{\boldsymbol{r}}_0$. I assert that the solution is,

$$G^{(1)}(\boldsymbol{r} - \boldsymbol{r}') = \frac{i}{4k}H_1(k|\boldsymbol{r} - \boldsymbol{r}'|)\frac{\boldsymbol{r} - \boldsymbol{r}'}{|\boldsymbol{r} - \boldsymbol{r}'|} \cdot \hat{\boldsymbol{r}}_0. \tag{6.14}$$

This can easily be shown by operating with $\hat{\boldsymbol{r}}_0 \cdot \nabla$ on both sides of the equation for the free Green function,

$$(\nabla^2 + k^2)G_0(\boldsymbol{r} - \boldsymbol{r}') = \delta(\boldsymbol{r} - \boldsymbol{r}'), \tag{6.15}$$

where the free Green function is,

$$G_0(\boldsymbol{r} - \boldsymbol{r}') = -\frac{i}{4}H_0(k|\boldsymbol{r} - \boldsymbol{r}'|). \tag{6.16}$$

The dot product in Eq. 6.14 ensures that the Green function has the correct angular dependence for dipole radiation in two dimensions. But a circularly symmetric potential, in our case a hard disc, does not *have* an orientation. How are we to decide the direction of the polarization vector $\hat{\boldsymbol{r}}_0$? The answer is, we don't have to! The *incident wave* is the thing that "polarizes" the scatterer. That is why there is a derivative operator in D above. The Green function must *operate* on the incident wave to find out which direction it is traveling in, so that it knows how to polarize the scatterer! This is the essence of including higher partial waves into the point scatterer model: it requires the inclusion of new Green functions, one for each partial wave, and each has a higher derivative than the last.

This is all well and good for a single scatterer, but how are we to do multiple scattering? This is after all why we turned to the point scatterer model in the first place: because it changes the coupled integral equations of multiple scattering into *algebraic* matrix equations. Is this still possible with the inclusion of higher partial waves? We shall see that the answer is yes. For s- and p-waves, it amounts to tracking the quantities $\{\psi_i, \partial_x\psi_i, \partial_y\psi_i\}$ at the scatterer locations, instead of just $\{\psi_i\}$ for s-wave scattering only. So for the inclusion of p-waves, the matrix to be inverted becomes three times bigger. If we include all partial waves up to L, then for N scatterers the dimension of the matrix is $(2L+1)N$.

6.3 An Example: $s + p$ for two hard discs

Let us now illustrate these methods for a concrete example: multiple scattering of s- and p-waves off two non-overlapping hard discs, not necessarily of the same radius. The full wave function has the form,

$$\psi(\boldsymbol{r}) = \phi(\boldsymbol{r}) + \sum_{i=1}^{2} s_i^{(0)} H_0(k|\boldsymbol{r}-\boldsymbol{r}_i|)\psi_i + \sum_{i=1}^{2} s_i^{(1)} H_1(k|\boldsymbol{r}-\boldsymbol{r}_i|)\frac{(x-x_i)\psi_{ix} + (y-y_i)\psi_{iy}}{ik|\boldsymbol{r}-\boldsymbol{r}_i|}, \quad (6.17)$$

where ψ_{ix} is shorthand for $\frac{\partial\psi_i(\boldsymbol{r})}{\partial x}|_{\boldsymbol{r}=\boldsymbol{r}_i}$, and ψ_i is short for $\psi_i(\boldsymbol{r}_i)$. The last factor in the last sum is just the dot product of the unit vector $\frac{\boldsymbol{r}-\boldsymbol{r}_i}{|\boldsymbol{r}-\boldsymbol{r}_i|}$ with the direction of the incident wave on the scatterer at $\boldsymbol{r}_i$, $(ik)^{-1}\nabla\psi_i$. That is, it is the cosine of the angle between these two vectors. This is exactly the correct angular dependence of the scattered p-wave.

The equation for $\psi_1(\boldsymbol{r})$ follows as,

$$\psi_1(\boldsymbol{r}) = \phi(\boldsymbol{r}) + s_2^{(0)} H_0(k|\boldsymbol{r}-\boldsymbol{r}_2|)\psi_2 + s_2^{(1)} H_1(k|\boldsymbol{r}-\boldsymbol{r}_2|)\frac{(x-x_2)\psi_{2x} + (y-y_2)\psi_{2y}}{ik|\boldsymbol{r}-\boldsymbol{r}_2|}, \quad (6.18)$$

with a similar equation for $\psi_2(\boldsymbol{r})$.

In addition, we need an equation relating the derivative waves ψ_{ix}. This is found by taking the gradient of Eq. 6.18. It is vital to realize, however, that as far as this gradient is concerned, the numbers $\psi_2, \psi_{2x}, \psi_{2y}$ are constants. Probably the messiest part of these calculations is taking these derivatives. As higher partial waves are added, more derivatives are necessary. Luckily, it only has to be done once, and then you have the answer for any potential, because the $s^{(l)}$ characterize a particular potential, and they just go along for the ride as far as the derivatives are concerned.

Here is ψ_{1x} for an incident plane wave $\phi(\boldsymbol{r}) = e^{i\boldsymbol{k}_0\cdot\boldsymbol{r}}$:

$$\begin{aligned}
\psi_{1x} &= ik_{0x}e^{i\boldsymbol{k}_0\cdot\boldsymbol{r}_1} \\
&- s_2^{(0)}kH_1(k|\boldsymbol{r}_1-\boldsymbol{r}_2|)\frac{x_1-x_2}{|\boldsymbol{r}_1-\boldsymbol{r}_2|}\psi_2 \\
&- is_2^{(1)}\left(\frac{-H_2(k|\boldsymbol{r}_1-\boldsymbol{r}_2|)(x_1-x_2)^2}{|\boldsymbol{r}_1-\boldsymbol{r}_2|^2}+\frac{H_1(k|\boldsymbol{r}_1-\boldsymbol{r}_2|)}{k|\boldsymbol{r}_1-\boldsymbol{r}_2|}\right)\psi_{2x} \\
&- is_2^{(1)}\left(\frac{-H_2(k|\boldsymbol{r}_1-\boldsymbol{r}_2|)(x_1-x_2)(y_1-y_2)}{|\boldsymbol{r}_1-\boldsymbol{r}_2|^2}\right)\psi_{2y},
\end{aligned} \tag{6.19}$$

and here is ψ_{1y},

$$\begin{aligned}
\psi_{1y} &= ik_{0y}e^{i\boldsymbol{k}_0\cdot\boldsymbol{r}_1} \\
&- s_2^{(0)}kH_1(k|\boldsymbol{r}_1-\boldsymbol{r}_2|)\frac{y_1-y_2}{|\boldsymbol{r}_1-\boldsymbol{r}_2|}\psi_2 \\
&- is_2^{(1)}\left(\frac{-H_2(k|\boldsymbol{r}_1-\boldsymbol{r}_2|)(x_1-x_2)(y_1-y_2)}{|\boldsymbol{r}_1-\boldsymbol{r}_2|^2}\right)\psi_{2x} \\
&- is_2^{(1)}\left(\frac{-H_2(k|\boldsymbol{r}_1-\boldsymbol{r}_2|)(y_1-y_2)^2}{|\boldsymbol{r}_1-\boldsymbol{r}_2|^2}+\frac{H_1(k|\boldsymbol{r}_1-\boldsymbol{r}_2|)}{k|\boldsymbol{r}_1-\boldsymbol{r}_2|}\right)\psi_{2y}.
\end{aligned} \tag{6.20}$$

The corresponding equations for ψ_{2x} and ψ_{2y} are found by interchanging everywhere the indices (1, 2) above (except on the order of the Hankel functions!).

These expressions are not too pretty, but it doesn't matter really. They are just matrix elements, and the matrix will have to be inverted numerically anyway. It will take longer to actually *load* the matrix, however, because of all the extra algebra. This becomes even more significant when adding partial waves higher than $l = 1$.

The expressions Eqs. 6.18, 6.19, and 6.20 combine to give $(\psi_1, \psi_{1x}, \psi_{1y}, \psi_2, \psi_{2x}, \psi_{2y})$, in terms of $(\phi_1, \phi_{1x}, \phi_{1y}, \phi_2, \phi_{2x}, \phi_{2y})$. These relations can be rewritten in the form of a six-by-six matrix equation,

$$\begin{pmatrix} \psi_1 \\ \psi_{1x} \\ \psi_{1y} \\ \psi_2 \\ \psi_{2x} \\ \psi_{2y} \end{pmatrix} = \begin{pmatrix} 1 & 0 & 0 & M_{14} & M_{15} & M_{16} \\ 0 & 1 & 0 & M_{24} & M_{25} & M_{26} \\ 0 & 0 & 1 & M_{34} & M_{35} & M_{36} \\ M_{41} & M_{42} & M_{43} & 1 & 0 & 0 \\ M_{51} & M_{52} & M_{53} & 0 & 1 & 0 \\ M_{61} & M_{62} & M_{63} & 0 & 0 & 1 \end{pmatrix}^{-1} \begin{pmatrix} \phi_1 \\ \phi_{1x} \\ \phi_{1y} \\ \phi_2 \\ \phi_{2x} \\ \phi_{2y} \end{pmatrix}. \tag{6.21}$$

The 18 non-trivial matrix elements can, with care, be read off from Eqs. 6.18, 6.19, 6.20). For completeness, we list them here:

$$\begin{aligned}
M_{14} &= -s_2^{(0)} H_0(kr_{12}) \\
M_{15} &= -\frac{s_2^{(1)} H_1(kr_{12}) x_{12}}{ikr_{12}} \\
M_{16} &= -\frac{s_2^{(1)} H_1(kr_{12}) y_{12}}{ikr_{12}} \\
M_{24} &= \frac{s_2^{(0)} H_1(kr_{12}) k x_{12}}{r_{12}} \\
M_{25} &= is_2^{(1)} \left(\frac{H_1(kr_{12})}{kr_{12}} - \frac{H_2(kr_{12}) x_{12}^2}{r_{12}^2} \right) \\
M_{26} &= -\frac{is_2^{(1)} H_2(kr_{12}) x_{12} y_{12}}{r_{12}^2} \\
M_{34} &= \frac{s_2^{(0)} H_1(kr_{12}) k y_{12}}{r_{12}} \\
M_{35} &= M_{26} \\
M_{36} &= is_2^{(1)} \left(\frac{H_1(kr_{12})}{kr_{12}} - \frac{H_2(kr_{12}) y_{12}^2}{r_{12}^2} \right)
\end{aligned}$$

where we have made some obvious abbreviations: $(x_1 - x_2) \to x_{12}$, etc. These elements make up the upper right block of the matrix. The lower left block is achieved by exchanging the indices (1,2) in the upper right block. Note that the matrix almost becomes symmetric, up to some minus signs, if the two discs have the same radius, because then $s_1^{(l)} = s_2^{(l)}$.

Although these formulae look quite forbidding, it is not really a problem, because the matrix will be inverted numerically anyway. Care does have to be taken when calculating these derivatives, however. Even more care is necessary for adding higher partial waves, but in principle the method is straightforward. For d-waves, for example, we would need the following derivatives, in addition to the ones we already have: ψ_{ixx}, ψ_{ixy}, and ψ_{iyy}. At first sight, one would think that this means we have three more new numbers which must be tracked at each scatterer location. However, we can use the fact that our solution satisfies the Helmholtz equation to find the number of truly independent derivatives. We have,

$$(\nabla^2 + k^2)\psi_i(\boldsymbol{r}) = 0, \tag{6.22}$$

or,

$$\psi_{iyy} = -\psi_{ixx} - k^2\psi_i, \tag{6.23}$$

so that the number ψ_{iyy} is superfluous, since it is given in terms of ψ_{ixx} and ψ_i. It is easy to show, by taking progressively higher derivatives of Eq. 6.22, that for any l only two more dimensions to the matrix are added for each higher partial wave. Thus, for N scatterers and L partial waves, the dimension of the matrix to be inverted is $N(2L+1)$.

In Fig. 6.1 we show the results of a simple experiment. A plane wave coming from below impacts two identical hard discs, such that $ka = 1$, and their centers are separated by a distance $d = 3a$. The picture on the left is with two s-wave scatterers. On the right, the same scatterers, but with p-wave included. Note that the boundary condition is satisfied better with the p-waves included, especially in the region between the scatterers. These pictures demonstrate that the addition of higher partial waves is moving us in the right direction towards a high energy solution of the multiple scattering problem. See Appendix B, Fig. B.1 for another example of the method.

By the way, we should not attach any significance to the non-zero amplitude of the wave *inside* the hard disc. In general, the wave function at a radius less than the range of the potential does not have any meaning when using point scatterers. It is only the *scattered wave* which exists outside the potential that the point scatterer model gets right. This is because the scattered wave is made up of both Bessel *and* Neumann functions, and the Neumann functions are singular at $r = 0$, so naturally they are nonsense inside the disc.

This seems to be related to the fact that if you find the eigenstates of a generic billiard from a superposition of plane waves, and then try to continue the solution beyond the billiard wall, the solution blows up.

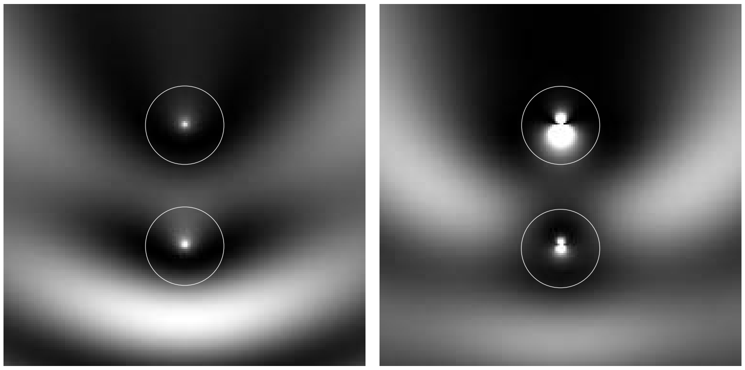

s-wave only s- and p-wave

Figure 6.1: Comparison between s-wave scattering and s+p-wave scattering. The boundaries of the discs are shown with a white outline. One clearly sees that a substantial fraction of the scattered wave is p-wave in character from the shape of the source functions inside the discs.

6.4 Rigorous derivation

Below I will prove that the techniques developed above for adding p-waves to the point scatterer model are correct, and show how higher angular momenta can be accounted for in the model.[1]

First we need the idea of a generalized incident wave. If we are considering a system of many scatterers, the wave that is incident on any one of the scatterers is not just the incident plane wave, but also includes the coherent superposition of all the waves coming from all the other scatterers. However, this complicated wave can be expanded in plane waves, because the plane waves are a complete set in free space. So let's write the wave incident on scatterer i as a superposition of plane waves:

$$\psi_0(\boldsymbol{r}) = \int \tilde{\psi}_0(\theta') e^{i\boldsymbol{k}(\theta')\cdot\boldsymbol{r}}\, d\theta'. \tag{6.24}$$

This is *almost* a Fourier transform. The difference is, we are holding the length of $\boldsymbol{k}(\theta)$ fixed, and only changing its direction.

Now, we know that if we had just a plane wave traveling in direction $\boldsymbol{k}_0$ incident on scatterer i, then the scattered wave from i would be,

$$\psi_s = \sum_{l=0}^{\infty} s^{(l)} H_l(k|\boldsymbol{r} - \boldsymbol{r}_i|) \cos l(\theta_i - \theta_0) e^{i\boldsymbol{k}_0\cdot\boldsymbol{r}_i}, \tag{6.25}$$

---

[1] This section is the result of enjoyable discussions with Maxim Olshanii.

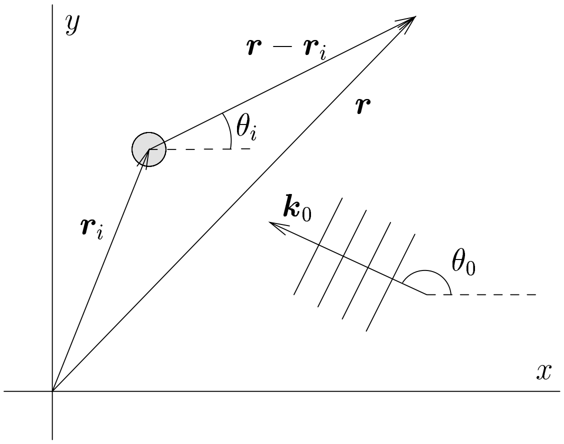

Figure 6.2: A plane wave incident on a scatterer displaced from the origin. The various angles in Eq. 6.25 are indicated. The angular dependence of the scattered p-wave would be $\cos(\theta_i - \theta_0)$.

where θ_i is the angle that $\boldsymbol{r}-\boldsymbol{r}_i$ makes with the x-axis, and θ_0 is the direction of the incident wave, as shown in Fig. 6.2. The phase $e^{i\boldsymbol{k}_0\cdot\boldsymbol{r}_i}$ is present because the scatterer is not at the origin. Using this expression, we can find the general form for the scattered wave when the incident wave is not plane, but a general solution of the Helmholtz equation, $\psi_0(\boldsymbol{r})$. We have,

$$\psi_s = \sum_{l=0}^{\infty} s^{(l)} H_l(k|\boldsymbol{r}-\boldsymbol{r}_i|) \int \tilde{\psi}_0(\theta')\cos l(\theta_i-\theta') e^{i\boldsymbol{k}(\theta')\cdot\boldsymbol{r}_i}\, d\theta'. \tag{6.26}$$

We now expand the cosine and consider the integrals that result:

$$\psi_s = \frac{1}{2}\sum_{l=0}^{\infty} s^{(l)} H_l(k|\boldsymbol{r}-\boldsymbol{r}_i|)\left(e^{il\theta_i}\int \tilde{\psi}_0(\theta')e^{-il\theta'}e^{i\boldsymbol{k}(\theta')\cdot\boldsymbol{r}_i}\, d\theta' + e^{-il\theta_i}\int \tilde{\psi}_0(\theta')e^{il\theta'}e^{i\boldsymbol{k}(\theta')\cdot\boldsymbol{r}_i}\, d\theta'\right) \tag{6.27}$$

Now we make a good guess. We assert that,

$$\left(\frac{\partial}{\partial z}\right)^l \psi_0(\boldsymbol{r})|_{\boldsymbol{r}=\boldsymbol{r}_i} = \left(\frac{ik}{2}\right)^l \int \tilde{\psi}_0(\theta')e^{-il\theta'}e^{i\boldsymbol{k}(\theta')\cdot\boldsymbol{r}_i}\, d\theta', \tag{6.28}$$

and,

$$\left(\frac{\partial}{\partial z^*}\right)^l \psi_0(\boldsymbol{r})|_{\boldsymbol{r}=\boldsymbol{r}_i} = \left(\frac{ik}{2}\right)^l \int \tilde{\psi}_0(\theta')e^{il\theta'}e^{i\boldsymbol{k}(\theta')\cdot\boldsymbol{r}_i}\, d\theta', \tag{6.29}$$

where $z = x + iy$. This can easily be shown by taking derivatives of Eq. 6.24, using the fact that,

$$\frac{\partial}{\partial z} = \frac{1}{2}\left(\frac{\partial}{\partial x} - i\frac{\partial}{\partial y}\right). \tag{6.30}$$

Using this result for the integrals, we have for the scattered wave,

$$\begin{aligned}\psi_s &= \frac{1}{2}\sum_{l=0}^{\infty} s^{(l)} H_l(k|\boldsymbol{r}-\boldsymbol{r}_i|)\left(\frac{2}{ik}\right)^l \left(e^{il\theta_i}\left(\frac{\partial}{\partial z}\right)^l + e^{-il\theta_i}\left(\frac{\partial}{\partial z^*}\right)^l\right)\psi_0(\boldsymbol{r})|_{\boldsymbol{r}=\boldsymbol{r}_i} \\ &= \sum_{l=0}^{\infty} s^{(l)} H_l(k|\boldsymbol{r}-\boldsymbol{r}_i|)\left(\frac{1}{ik|\boldsymbol{r}-\boldsymbol{r}_i|}\right)^l \times \\ &\quad \mathrm{Re}\left[((x-x_i)+i(y-y_i))^l\left(\frac{\partial}{\partial x}-i\frac{\partial}{\partial y}\right)^l\right]\psi_0(\boldsymbol{r})|_{\boldsymbol{r}=\boldsymbol{r}_i}. \qquad (6.31)\end{aligned}$$

This is an interesting equation. It means that we can accurately express the scattered wave up to order l in the partial wave expansion with just a few numbers. These numbers are the value and derivatives up to order l of the generalized incident wave at the *center* of the potential. We have reduced the boundary conditions at the *surface* of the potential to a *point*. The problem is then zero dimensional, in the sense that it becomes algebraic instead of involving integrals over surfaces. In 3D, this reduction is even more dramatic, because there the boundary surface of the potential is 2D, but the problem can still be reduced to zero dimensions.

Thus we have found the derivative operator that, when operating on a plane wave traveling along the x-axis, gives $\cos l\theta$. This operator is,

$$D^{(l)} = \left(\frac{1}{ikr}\right)^l \mathrm{Re}\left[(x+iy)^l\left(\frac{\partial}{\partial x}-i\frac{\partial}{\partial y}\right)^l\right]. \qquad (6.32)$$

Let's calculate what this operator is for $l=0,1,2$ to show that it is the same as the guesses we made in earlier sections. The case $l=0$ is trivial. Then $D^{(0)}=1$. For $l=1$, we have,

$$\begin{aligned}D^{(1)} &= \frac{1}{ikr}\mathrm{Re}\left[(x+iy)\left(\frac{\partial}{\partial x}-i\frac{\partial}{\partial y}\right)\right] \\ &= \frac{1}{ikr}\left(x\frac{\partial}{\partial x}+y\frac{\partial}{\partial y}\right) \\ &= \frac{1}{ikr}\boldsymbol{r}\cdot\nabla, \qquad (6.33)\end{aligned}$$

just as we guessed. For $l=2$,

$$\begin{aligned}D^{(2)} &= \frac{1}{(ikr)^2}\mathrm{Re}\left[(x+iy)^2\left(\frac{\partial}{\partial x}-i\frac{\partial}{\partial y}\right)^2\right] \\ &= \frac{1}{(ikr)^2}\mathrm{Re}\left[\left(x^2-y^2+2ixy\right)\left(\frac{\partial^2}{\partial x^2}-\frac{\partial^2}{\partial y^2}-2i\frac{\partial^2}{\partial x\partial y}\right)\right] \\ &= \frac{1}{(ikr)^2}\left((x^2-y^2)\left(\frac{\partial^2}{\partial x^2}-\frac{\partial^2}{\partial y^2}\right)+4xy\frac{\partial^2}{\partial x\partial y}\right), \qquad (6.34)\end{aligned}$$

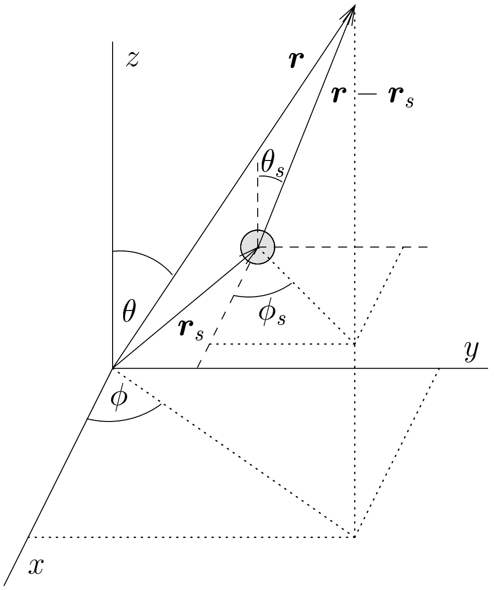

Figure 6.3: A scatterer in 3D. The various angles and vectors appear in the expression for the scattered wave, Eq. 6.35. The incident wave, traveling in direction (θ_0, ϕ_0), is not shown.

which is the same as the form we guessed for $l = 2$ earlier in Eq. 6.12. Now it is clear how to add any order partial wave l, so that the point scatterer model has been extended in principle to include all partial waves.

6.5 Three dimensional case

In this section we will go through the steps necessary to extend the methods above to the three dimensional case. For a plane wave with wave vector $\mathbf{k}_0$ incident on a scatterer at $\boldsymbol{r}_s$, the scattered wave is,

$$\psi_s(\boldsymbol{r}) = \sum_{l=0}^{\infty} \sum_{m=-l}^{l} s^{(l)} h_l(k|\boldsymbol{r} - \boldsymbol{r}_s|) Y_{lm}(\theta_s, \phi_s) Y_{lm}^*(\theta_0, \phi_0) e^{i\boldsymbol{k}_0 \cdot \boldsymbol{r}_s}, \tag{6.35}$$

where $\boldsymbol{r}_s$ is the location of the scatterer, and (θ_s, ϕ_s) are the angles defining the direction of $\boldsymbol{r} - \boldsymbol{r}_s$, as shown in Fig. 6.3. The incident wave is traveling in the direction defined by (θ_0, ϕ_0), and $h_l(x)$ is an outgoing spherical Hankel function. The $Y_{lm}(\theta, \phi)$ are the familiar spherical harmonics. In 3D they play the role of the 2D angular functions $e^{il\theta}$. The phase $e^{i\boldsymbol{k}_0 \cdot \boldsymbol{r}_s}$ is present because the scatterer is not at the origin. One might have imagined that a sum over m would not be necessary, since we are dealing with scatterers which mimic spherically symmetric potentials. The sum *is* necessary, however, because the incident wave is not necessarily along the z-axis. Only in the special situation of incidence along z is one allowed to drop the sum over m. Conversely, one may well wonder why the amplitudes $s^{(l)}$ are not also indexed by m. The reason here is that the model potentials have spherical symmetry, so that in partial wave expansion of the scattering amplitude for a single potential, only terms with $m = 0$ enter in. If the potentials were not spherical, then the $s^{(l)}$ would also be indexed by m.

Let us explicitly show that the $s^{(l)}$ do not depend on m for the special case of the hard sphere potential. We will take an incident plane wave traveling in direction $\boldsymbol{k}_0$, which can be expanded in spherical harmonics thus,

$$\phi(\boldsymbol{r}) = e^{i\boldsymbol{k}_0\cdot\boldsymbol{r}} = 4\pi \sum_{l=0}^{\infty}\sum_{m=-l}^{l} i^l j_l(kr) Y_{lm}(\theta,\phi) Y_{lm}^*(\theta_0,\phi_0), \tag{6.36}$$

where (θ_0, ϕ_0) define the direction of $\boldsymbol{k}_0$ and (θ, ϕ) define the direction of $\boldsymbol{r}$. The boundary condition on $\psi = \phi + \psi_s$ at $r = a$ is (for simplicity we place the scatterer at the origin),

$$\phi(r = a) + \psi_s(r = a) = 0, \tag{6.37}$$

or,

$$\sum_{l=0}^{\infty}\sum_{m=-l}^{l} Y_{lm}(\theta,\phi) Y_{lm}^*(\theta_0,\phi_0)\left(4\pi i^l j_l(ka) + s^{(l)} h_l(ka)\right) = 0. \tag{6.38}$$

This implies,

$$s^{(l)} = -\frac{4\pi i^l j_l(ka)}{h_l(ka)}, \tag{6.39}$$

which is independent of m, as advertised.

Now, in our situation we do not have a pure plane wave incident on the scatterer at $\boldsymbol{r}_s$, but it is made up as well from the coherent superposition of all the waves from other scatterers. Therefore we write the incident wave as a superposition of plane waves traveling in all directions, thus:

$$\psi_0(\boldsymbol{r}) = \iint \tilde{\psi}_0(\theta',\phi') e^{i\boldsymbol{k}(\theta',\phi')\cdot\boldsymbol{r}}\, d\theta'\, d\phi'. \tag{6.40}$$

In analogy with Eq. 6.35, the response of our scatterer to this *generalized* incident wave is,

$$\psi_s(\boldsymbol{r}) = \sum_{l=0}^{\infty}\sum_{m=-l}^{l} s^{(l)} h_l(k|\boldsymbol{r}-\boldsymbol{r}_s|) Y_{lm}(\theta_s,\phi_s) \iint \tilde{\psi}_0(\theta',\phi') Y_{lm}^*(\theta',\phi') e^{i\boldsymbol{k}(\theta',\phi')\cdot\boldsymbol{r}_s}\, d\theta'\, d\phi'. \tag{6.41}$$

Now, in the previous section the method relied on finding a way of writing the integral appearing in Eq. 6.27 in terms of a derivative operator acting on the generalized incident wave in Eq. 6.24. This will be our approach here. In Eq. 6.41 we, have an integral, and we want to try and express that integral as a derivative operator acting on the wave given by Eq. 6.40. Let us look again at the integral appearing in Eq. 6.41:

$$I_{lm} = \iint \tilde{\psi}_0(\theta', \phi') Y^*_{lm}(\theta', \phi') e^{i\boldsymbol{k}(\theta',\phi')\cdot\boldsymbol{r}_s}\, d\theta'\, d\phi'. \tag{6.42}$$

We must find a combination of the partial derivatives, $\{\partial_x, \partial_y, \partial_z\}$ such that when they act on Eq. 6.40, they give I_{lm}. Let us call this mystery derivative operator D_{lm}. That is,

$$D_{lm}\psi_0(\boldsymbol{r})|_{\boldsymbol{r}=\boldsymbol{r}_s} = I_{lm}. \tag{6.43}$$

Now, the only variable in the incident wave ψ_0 that is operated on by D_{lm} is $\boldsymbol{r}$. Thus we can safely move D_{lm} through the integrals over (θ', ϕ') in the expression for ψ_0. We must therefore have,

$$D_{lm} e^{i\boldsymbol{k}(\theta',\phi')\cdot\boldsymbol{r}}|_{\boldsymbol{r}=\boldsymbol{r}_s} = Y^*_{lm}(\theta', \phi') e^{i\boldsymbol{k}(\theta',\phi')\cdot\boldsymbol{r}_s}. \tag{6.44}$$

Solving this equation for D_{lm} is the main task of this section. Let us investigate the action of the various derivatives on the plane wave $e^{i\boldsymbol{k}(\theta',\phi')\cdot\boldsymbol{r}}$:

$$\begin{aligned} \left(\frac{\partial}{\partial x}\right)^n e^{i\boldsymbol{k}(\theta',\phi')\cdot\boldsymbol{r}}|_{\boldsymbol{r}=\boldsymbol{r}_s} &= (ik\sin\theta'\cos\phi')^n\, e^{i\boldsymbol{k}(\theta',\phi')\cdot\boldsymbol{r}_s} \\ &= \left(\frac{ikx'}{r'}\right)^n e^{i\boldsymbol{k}(\theta',\phi')\cdot\boldsymbol{r}_s}. \end{aligned} \tag{6.45}$$

Similarly,

$$\left(\frac{\partial}{\partial y}\right)^n e^{i\boldsymbol{k}(\theta',\phi')\cdot\boldsymbol{r}}|_{\boldsymbol{r}=\boldsymbol{r}_s} = \left(\frac{iky'}{r'}\right)^n e^{i\boldsymbol{k}(\theta',\phi')\cdot\boldsymbol{r}_s}, \tag{6.46}$$

$$\left(\frac{\partial}{\partial z}\right)^n e^{i\boldsymbol{k}(\theta',\phi')\cdot\boldsymbol{r}}|_{\boldsymbol{r}=\boldsymbol{r}_s} = \left(\frac{ikz'}{r'}\right)^n e^{i\boldsymbol{k}(\theta',\phi')\cdot\boldsymbol{r}_s}, \tag{6.47}$$

because,

$$\boldsymbol{k}(\theta', \phi') = k(\sin\theta'\cos\phi', \sin\theta'\sin\phi', \cos\theta'). \tag{6.48}$$

Therefore, our task reduces to finding the expression of $Y^*_{lm}(\theta, \phi)$ in terms of powers of $\{\frac{x}{r}, \frac{y}{r}, \frac{z}{r}\}$, as can be seen from Eq. 6.44 and the derivatives in Eqs. 6.45, 6.46, 6.47.

Now, $Y^*_{lm}(\theta, \phi)$ is given by,

$$\begin{aligned} Y^*_{lm}(\theta, \phi) &= \sqrt{\frac{2l+1}{4\pi}\frac{(l-m)!}{(l+m)!}} P_{lm}(\cos\theta) e^{-im\phi} \\ &= (\pm 1)^{|m|}\sqrt{\frac{2l+1}{4\pi}\frac{(l-|m|)!}{(l+|m|)!}} P_{l|m|}(\cos\theta) e^{\mp i|m|\phi} \end{aligned} \tag{6.49}$$

where the upper sign is for $m > 0$ and the lower sign is for $m < 0$. First let us see how we can get the ϕ-dependence of $Y^*_{lm}(\theta, \phi)$ from derivative operators involving $\frac{x}{r}$ and $\frac{y}{r}$. We have,

$$\begin{aligned} e^{\mp i|m|\phi} &= (\cos\phi \mp i\sin\phi)^{|m|} \\ &= \left(\frac{\sin\theta\cos\phi}{\sin\theta} \mp i\frac{\sin\theta\sin\phi}{\sin\theta}\right)^{|m|} \\ &= \frac{1}{(\sin\theta)^{|m|}}\left(\frac{x}{r} \mp i\frac{y}{r}\right)^{|m|} \end{aligned} \tag{6.50}$$

This shows how to produce the ϕ-dependence of $Y^*_{lm}(\theta, \phi)$: we just operate with something proportional to $(\partial_x \mp i\partial_y)^{|m|}$. Now for the θ-dependence: we can write the Legendre functions $P_{l|m|}(x)$ in terms of the Legendre polynomials thus:

$$P_{l|m|}(x) = (-1)^{|m|}(1-x^2)^{|m|/2}\frac{d^{|m|}}{dx^{|m|}}P_l(x). \tag{6.51}$$

Now we put $x = \cos\theta$ to find,

$$\begin{aligned} P_{l|m|}(\cos\theta)e^{\mp i|m|\phi} &= \frac{1}{(\sin\theta)^{|m|}}\left(\frac{x}{r} \mp i\frac{y}{r}\right)^{|m|}(-1)^{|m|}(\sin\theta)^{|m|}\frac{d^{|m|}}{d(\cos\theta)^{|m|}}P_l(\cos\theta) \\ &= (-1)^{|m|}\left(\frac{x}{r} \mp i\frac{y}{r}\right)^{|m|}\frac{d^{|m|}}{d\left(\frac{z}{r}\right)^{|m|}}P_l\left(\frac{z}{r}\right). \end{aligned} \tag{6.52}$$

This expression is what we have been looking for. It allows us to express the spherical harmonic solely in terms of the directional cosines, $\{\frac{x}{r}, \frac{y}{r}, \frac{z}{r}\}$. We have,

$$Y^*_{lm}(\theta, \phi) = (\pm 1)^{|m|}\sqrt{\frac{2l+1}{4\pi}\frac{(l-|m|)!}{(l+|m|)!}}\left(\frac{x}{r} \mp i\frac{y}{r}\right)^{|m|}p_{lm}\left(\frac{z}{r}\right), \tag{6.53}$$

where,

$$p_{lm}(x) = \frac{d^{|m|}}{dx^{|m|}}P_l(x). \tag{6.54}$$

Using Eq. 6.53 and Eqs. 6.45, 6.46, 6.47, we can finally write down the operator D_{lm}. It is,

$$D_{lm} = (\mp 1)^{|m|}\sqrt{\frac{2l+1}{4\pi}\frac{(l-|m|)!}{(l+|m|)!}}\left(\frac{\partial}{\partial x} \mp i\frac{\partial}{\partial y}\right)^{|m|}d_{lm}\left(\frac{\partial}{\partial z}, \nabla^2\right). \tag{6.55}$$

A few words are in order at this point. We must explain what is meant by the operator d_{lm}. The function $p_{lm}(x)$ is a polynomial in x of degree $l - |m|$. If $l - |m|$ is even (odd) then $p_{lm}(x)$ contains all even (odd) powers of x up to $l - |m|$. To illustrate, we will calculate the operator D_{lm} for $l = 4, m = 1$. We have,

$$\begin{aligned} p_{4,1}(x) &= \frac{d}{dx} P_4(x) \\ &= \frac{d}{dx}\left(\frac{35}{8}x^4 - \frac{15}{4}x^2 + 3\right) \\ &= \frac{5}{2}\left(7x^3 - 3x\right). \end{aligned} \tag{6.56}$$

Now, the differential operator that produces this polynomial (with $x = \cos\theta$) when acting on a plane wave must have all of its derivatives of order 3, no more and no less. The only possible combination is,

$$d_{4,1}\left(\frac{\partial}{\partial z}, \nabla^2\right) = \frac{5}{2}\left(\frac{1}{ik}\right)^3 \left(7\frac{\partial^3}{\partial z^3} - 3\frac{\partial}{\partial z}\nabla^2\right). \tag{6.57}$$

Now we understand what is meant by d_{lm} in Eq. 6.55. One first computes the polynomial $p_{lm}(x)$, then replaces everywhere x with $\partial/\partial z$, and then inserts as many powers of ∇^2 in each term as is necessary so that each term has derivatives of order $l - |m|$. Then the whole operator must be divided by $(ik)^{l-|m|}$.

The operator $d_{4,1}(\partial/\partial z, \nabla^2)$, in combination with the proper x and y derivatives, will give us the full $D_{4,1}$. Using Eq. 6.55,

$$D_{4,1} = -\frac{15}{8\sqrt{5\pi}}\left(\frac{1}{ik}\right)^4 \left(\frac{\partial}{\partial x} - i\frac{\partial}{\partial y}\right)\left(7\frac{\partial^3}{\partial z^3} - 3\frac{\partial}{\partial z}\nabla^2\right). \tag{6.58}$$

Similarly, we have for $l = 4, m = -1$,

$$D_{4,-1} = \frac{15}{8\sqrt{5\pi}}\left(\frac{1}{ik}\right)^4 \left(\frac{\partial}{\partial x} + i\frac{\partial}{\partial y}\right)\left(7\frac{\partial^3}{\partial z^3} - 3\frac{\partial}{\partial z}\nabla^2\right). \tag{6.59}$$

We can check this by finding the operation of $D_{4,1}$ on a plane wave:

$$\begin{aligned} D_{4,1} \exp\left[i\boldsymbol{k}(\theta', \phi') \cdot \boldsymbol{r}\right]\Big|_{\boldsymbol{r}=\boldsymbol{r}_s} &= D_{4,1} \exp\left[ik\left(\frac{xx'}{r'} + \frac{yy'}{r'} + \frac{zz'}{r'}\right)\right]\Bigg|_{\boldsymbol{r}=\boldsymbol{r}_s} \\ &= -\frac{15}{8\sqrt{5\pi}}\left(\frac{1}{ik}\right)^4 \left(\frac{ikx'}{r'} - i\frac{iky'}{r'}\right) \times \\ &\quad \left\{7\left(\frac{ikz'}{r}\right)^3 - 3\left(\frac{ikz'}{r'}\right)(ik)^2\right\} e^{i\boldsymbol{k}(\theta',\phi')\cdot\boldsymbol{r}_s} \\ &= -\frac{15}{8\sqrt{5\pi}}\left(\frac{x'}{r'} - i\frac{y'}{r'}\right)\left\{7\left(\frac{z'}{r}\right)^3 - 3\left(\frac{z'}{r'}\right)\right\} e^{i\boldsymbol{k}(\theta',\phi')\cdot\boldsymbol{r}_s} \\ &= -\frac{15}{8\sqrt{5\pi}} \sin\theta' \left(7\cos^3\theta' - 3\cos\theta'\right) e^{-im\phi'} e^{i\boldsymbol{k}(\theta',\phi')\cdot\boldsymbol{r}_s} \\ &= Y^*_{4,1}(\theta', \phi') e^{i\boldsymbol{k}(\theta',\phi')\cdot\boldsymbol{r}_s}. \end{aligned} \tag{6.60}$$

Thus we have succeeded in finding the operator, which, when it acts on the generalized incident wave, returns the necessary spherical harmonic. We can then replace the integral appearing in Eq. 6.41 thus,

$$I_{lm} = D_{lm}\psi_0(\boldsymbol{r})|_{\boldsymbol{r}=\boldsymbol{r}_s}. \tag{6.61}$$

This leaves us with an expression for the scattered wave in terms of the incident wave and derivatives thereof, just as we had in the 2D case. The derivative operators for a given l, m will not be pleasant to behold. However, once calculated they are good for any potential, since the characteristics of the potential are contained within the $s^{(l)}$. Furthermore, the matrix we eventually find will have to be inverted numerically anyway, so the ugliness of its elements is not an important issue. If the reader is beginning to think that this formalism is becoming terribly complicated, she should keep in mind the alternative: solving a Lippmann-Schwinger with several disconnected potentials such as in Eq. 2.12:

$$\psi(\boldsymbol{r}) = \phi(\boldsymbol{r}) + \sum_i \int G(\boldsymbol{r}, \boldsymbol{r}')V_i(\boldsymbol{r}')\psi(\boldsymbol{r}')\ d^3\boldsymbol{r}' \tag{6.62}$$

One hardly knows where to begin when faced with a multiple-integral equation such as this!

6.6 An example: two scatterers

As an illustration of the method, we will show how to incorporate p-waves into the 3D point scatterer model. We will need the following operators: $D_{0,0}, D_{1,0}, D_{1,\pm 1}$. Using Eq. 6.55 we have,

$$\begin{aligned} D_{0,0} &= \frac{1}{\sqrt{4\pi}} && (6.63)\\ D_{1,0} &= \sqrt{\frac{3}{4\pi}}\frac{1}{ik}\frac{\partial}{\partial z} && (6.64)\\ D_{1,\pm 1} &= \mp\sqrt{\frac{3}{8\pi}}\frac{1}{ik}\left(\frac{\partial}{\partial x} \mp i\frac{\partial}{\partial y}\right). && (6.65)\end{aligned}$$

It is easy to show that the action of these operators on a plane wave is,

$$\begin{aligned} D_{0,0}e^{i\boldsymbol{k}(\theta',\phi')\cdot\boldsymbol{r}}|_{\boldsymbol{r}=\boldsymbol{r}_s} &= \frac{1}{\sqrt{4\pi}}e^{i\boldsymbol{k}(\theta',\phi')\cdot\boldsymbol{r}_s}\\ &= Y^*_{0,0}(\theta',\phi')e^{i\boldsymbol{k}(\theta',\phi')\cdot\boldsymbol{r}_s} && (6.66)\\ D_{1,0}e^{i\boldsymbol{k}(\theta',\phi')\cdot\boldsymbol{r}}|_{\boldsymbol{r}=\boldsymbol{r}_s} &= \sqrt{\frac{3}{4\pi}}\cos\theta' e^{i\boldsymbol{k}(\theta',\phi')\cdot\boldsymbol{r}_s}\\ &= Y^*_{1,0}(\theta',\phi')e^{i\boldsymbol{k}(\theta',\phi')\cdot\boldsymbol{r}_s} && (6.67)\end{aligned}$$

$$\begin{aligned} D_{1,\pm 1} e^{i\boldsymbol{k}(\theta',\phi')\cdot\boldsymbol{r}}\big|_{\boldsymbol{r}=\boldsymbol{r}_s} &= \mp\sqrt{\frac{3}{8\pi}}\sin\theta' e^{\mp i\phi'} e^{i\boldsymbol{k}(\theta',\phi')\cdot\boldsymbol{r}_s} \\ &= Y^*_{1,\pm 1}(\theta',\phi') e^{i\boldsymbol{k}(\theta',\phi')\cdot\boldsymbol{r}_s} \qquad (6.68) \end{aligned}$$

Now we turn to the problem of the two scatterers, placed at points $\boldsymbol{r}_1, \boldsymbol{r}_2$. By analogy with Eq. 6.41, the solution is,

$$\psi(\boldsymbol{r}) = \phi(\boldsymbol{r}) + \sum_{i=1}^{2}\sum_{l=0}^{1}\sum_{m=-l}^{l} s^{(l)} h_l(k|\boldsymbol{r}-\boldsymbol{r}_i|) Y_{lm}(\theta_i,\phi_i) D_{lm}\psi_i(\boldsymbol{r})\big|_{\boldsymbol{r}=\boldsymbol{r}_i} \qquad (6.69)$$

with ψ_i defined by,

$$\begin{aligned} \psi_1(\boldsymbol{r}) &= \phi(\boldsymbol{r}) + \sum_{l=0}^{1}\sum_{m=-l}^{l} s^{(l)} h_l(k|\boldsymbol{r}-\boldsymbol{r}_2|) Y_{lm}(\theta_2,\phi_2) D_{lm}\psi_2(\boldsymbol{r})\big|_{\boldsymbol{r}=\boldsymbol{r}_2}, \qquad (6.70) \\ \psi_2(\boldsymbol{r}) &= \phi(\boldsymbol{r}) + \sum_{l=0}^{1}\sum_{m=-l}^{l} s^{(l)} h_l(k|\boldsymbol{r}-\boldsymbol{r}_1|) Y_{lm}(\theta_1,\phi_1) D_{lm}\psi_1(\boldsymbol{r})\big|_{\boldsymbol{r}=\boldsymbol{r}_1}. \qquad (6.71) \end{aligned}$$

Now it is just a matter of inserting the operators D_{lm}, expanding the results of Eqs. 6.70, 6.71 and their derivatives, and then finding the matrix that relates the values and slopes of the incident wave to those of ψ_1, ψ_2. Before we take the necessary derivatives of Eqs. 6.70, 6.71, we must first write these equations in a form that makes their x, y, z dependence transparent. We will begin with Eq. 6.70. The procedure is, we insert the forms for the D_{lm} into Eq. 6.70, apply them to the incident wave, and expand. One finds,

$$\begin{aligned} \psi_1(\boldsymbol{r}) &= \phi(\boldsymbol{r}) \\ &\quad + \frac{s_2^{(0)} h_0(k|\boldsymbol{r}-\boldsymbol{r}_2|)}{4\pi}\psi_2 \\ &\quad + \frac{3 s_2^{(1)} h_1(k|\boldsymbol{r}-\boldsymbol{r}_2|)}{4\pi i k}\left[\sin\theta_2\cos\phi_2\psi_{2x} + \sin\theta_2\sin\phi_2\psi_{2y} + \cos\theta_2\psi_{2z}\right] \\ &= \phi(\boldsymbol{r}) \\ &\quad + \frac{s_2^{(0)} h_0(k|\boldsymbol{r}-\boldsymbol{r}_2|)}{4\pi}\psi_2 \\ &\quad + \frac{3 s_2^{(1)} h_1(k|\boldsymbol{r}-\boldsymbol{r}_2|)}{4\pi i k}\left(\frac{x-x_2}{|\boldsymbol{r}-\boldsymbol{r}_2|}\psi_{2x} + \frac{y-y_2}{|\boldsymbol{r}-\boldsymbol{r}_2|}\psi_{2y} + \frac{z-z_2}{|\boldsymbol{r}-\boldsymbol{r}_2|}\psi_{2z}\right), \qquad (6.72) \end{aligned}$$

where ψ_2 is shorthand for $\psi_2(\boldsymbol{r}_2)$ and similarly, $\psi_{2\alpha} \equiv \partial_\alpha\psi_2(\boldsymbol{r})|_{\boldsymbol{r}=\boldsymbol{r}_2}$. The first term is just the incident wave, the second term is the s-wave scattered from $\boldsymbol{r}_2$, and the third term is the p-wave scattered from $\boldsymbol{r}_2$. Eq. 6.72 should look familiar. It is the exact analog of Eq. 6.18 in the 2D case. We are now ready to take the necessary derivatives to get an equation relating the derivatives of $\psi_1(\boldsymbol{r})$ to $\psi_2, \psi_{2x}, \psi_{2y}, \psi_{2z}$. A straightforward calculation yields the x-derivative of Eq. 6.72 as,

$$\begin{aligned}
\psi_{1x} &= \phi_{1x} \\
&\quad - \frac{s_2^{(0)} h_1(k|\boldsymbol{r}_1 - \boldsymbol{r}_2|) k (x_1 - x_2)}{4\pi |\boldsymbol{r}_1 - \boldsymbol{r}_2|} \psi_2 \\
&\quad + \frac{3 s_2^{(1)}}{4\pi i k} \Bigg[\left(\frac{h_1(k|\boldsymbol{r}_1 - \boldsymbol{r}_2|)}{|\boldsymbol{r}_1 - \boldsymbol{r}_2|} - \frac{k h_2(k|\boldsymbol{r}_1 - \boldsymbol{r}_2|)(x_1 - x_2)^2}{|\boldsymbol{r}_1 - \boldsymbol{r}_2|^2} \right) \psi_{2x} \\
&\qquad - \frac{k h_2(k|\boldsymbol{r}_1 - \boldsymbol{r}_2|)(x_1 - x_2)(y_1 - y_2)}{|\boldsymbol{r}_1 - \boldsymbol{r}_2|^2} \psi_{2y} \\
&\qquad - \frac{k h_2(k|\boldsymbol{r}_1 - \boldsymbol{r}_2|)(x_1 - x_2)(z_1 - z_2)}{|\boldsymbol{r}_1 - \boldsymbol{r}_2|^2} \psi_{2z} \Bigg]. \qquad (6.73)
\end{aligned}$$

Similarly, the y- and z-derivatives are,

$$\begin{aligned}
\psi_{1y} &= \phi_{1y} \\
&\quad - \frac{s_2^{(0)} h_1(k|\boldsymbol{r}_1 - \boldsymbol{r}_2|) k (y_1 - y_2)}{4\pi |\boldsymbol{r}_1 - \boldsymbol{r}_2|} \psi_2 \\
&\quad + \frac{3 s_2^{(1)}}{4\pi i k} \Bigg[- \frac{k h_2(k|\boldsymbol{r}_1 - \boldsymbol{r}_2|)(x_1 - x_2)(y_1 - y_2)}{|\boldsymbol{r}_1 - \boldsymbol{r}_2|^2} \psi_{2x} \\
&\qquad + \left(\frac{h_1(k|\boldsymbol{r}_1 - \boldsymbol{r}_2|)}{|\boldsymbol{r}_1 - \boldsymbol{r}_2|} - \frac{k h_2(k|\boldsymbol{r}_1 - \boldsymbol{r}_2|)(y_1 - y_2)^2}{|\boldsymbol{r}_1 - \boldsymbol{r}_2|^2} \right) \psi_{2y} \\
&\qquad - \frac{k h_2(k|\boldsymbol{r}_1 - \boldsymbol{r}_2|)(y_1 - y_2)(z_1 - z_2)}{|\boldsymbol{r}_1 - \boldsymbol{r}_2|^2} \psi_{2z} \Bigg], \qquad (6.74) \\
\psi_{1z} &= \phi_{1z} \\
&\quad - \frac{s_2^{(0)} h_1(k|\boldsymbol{r}_1 - \boldsymbol{r}_2|) k (z_1 - z_2)}{4\pi |\boldsymbol{r}_1 - \boldsymbol{r}_2|} \psi_2 \\
&\quad + \frac{3 s_2^{(1)}}{4\pi i k} \Bigg[- \frac{k h_2(k|\boldsymbol{r}_1 - \boldsymbol{r}_2|)(x_1 - x_2)(z_1 - z_2)}{|\boldsymbol{r}_1 - \boldsymbol{r}_2|^2} \psi_{2x} \\
&\qquad - \frac{k h_2(k|\boldsymbol{r}_1 - \boldsymbol{r}_2|)(y_1 - y_2)(z_1 - z_2)}{|\boldsymbol{r}_1 - \boldsymbol{r}_2|^2} \psi_{2y} \\
&\qquad + \left(\frac{h_1(k|\boldsymbol{r}_1 - \boldsymbol{r}_2|)}{|\boldsymbol{r}_1 - \boldsymbol{r}_2|} - \frac{k h_2(k|\boldsymbol{r}_1 - \boldsymbol{r}_2|)(z_1 - z_2)^2}{|\boldsymbol{r}_1 - \boldsymbol{r}_2|^2} \right) \psi_{2z} \Bigg]. \qquad (6.75)
\end{aligned}$$

The analogous expressions for $\psi_{2x}, \psi_{2y}, \psi_{2z}$ can be had by interchanging everywhere the indices (1,2) (except, of course, on the Hankel functions). These equations, together with Eq. 6.72, give eight equations relating the various numbers $\psi_1, \psi_{1x}, \psi_{1y}, \psi_{1z}, \psi_2, \psi_{2x}, \psi_{2y}, \psi_{2z}$

to one another. These equations form a matrix equation, thus,

$$\begin{pmatrix} \phi_1 \\ \phi_{1x} \\ \phi_{1y} \\ \phi_{1z} \\ \phi_2 \\ \phi_{2x} \\ \phi_{2y} \\ \phi_{2z} \end{pmatrix} = \begin{pmatrix} 1 & 0 & 0 & 0 & M_{15} & M_{16} & M_{17} & M_{18} \\ 0 & 1 & 0 & 0 & M_{25} & M_{26} & M_{27} & M_{28} \\ 0 & 0 & 1 & 0 & M_{35} & M_{36} & M_{37} & M_{38} \\ 0 & 0 & 0 & 1 & M_{35} & M_{36} & M_{37} & M_{48} \\ M_{51} & M_{52} & M_{53} & M_{54} & 1 & 0 & 0 & 0 \\ M_{61} & M_{62} & M_{63} & M_{64} & 0 & 1 & 0 & 0 \\ M_{71} & M_{72} & M_{73} & M_{74} & 0 & 0 & 1 & 0 \\ M_{81} & M_{82} & M_{83} & M_{84} & 0 & 0 & 0 & 1 \end{pmatrix} \begin{pmatrix} \psi_1 \\ \psi_{1x} \\ \psi_{1y} \\ \psi_{1z} \\ \psi_2 \\ \psi_{2x} \\ \psi_{2y} \\ \psi_{2z} \end{pmatrix}. \tag{6.76}$$

This matrix must then be inverted to solve for the generalized incident waves ψ_1, ψ_2 (value and slope) at each scatterer. Once these values are known, we have the solution. The final answer is then,

$$\begin{aligned} \psi(\boldsymbol{r}) &= \phi(\boldsymbol{r}) \\ &+ \sum_{i=1}^{2} \left[\frac{s_2^{(0)} h_0(k|\boldsymbol{r}-\boldsymbol{r}_i|)}{4\pi} \psi_i \right. \\ &\qquad \left. + \frac{3 s_i^{(1)} h_1(k|\boldsymbol{r}-\boldsymbol{r}_i|)}{4\pi i k} \left(\frac{x - x_i}{|\boldsymbol{r}-\boldsymbol{r}_i|} \psi_{ix} + \frac{y - y_i}{|\boldsymbol{r}-\boldsymbol{r}_i|} \psi_{iy} + \frac{z - z_i}{|\boldsymbol{r}-\boldsymbol{r}_i|} \psi_{iz} \right) \right]. \end{aligned} \tag{6.77}$$

The 32 non-trivial matrix elements can be read off from Eqs. 6.72, 6.73, 6.74, 6.75. For completeness, we will list them (employing some obvious abbreviations):

$$\begin{aligned} M_{15} &= -\frac{s_2^{(0)} h_0(kr_{12})}{4\pi} \\ M_{16} &= -\frac{3 s_2^{(1)} h_1(kr_{12}) x_{12}}{4\pi i k r_{12}} \\ M_{17} &= -\frac{3 s_2^{(1)} h_1(kr_{12}) y_{12}}{4\pi i k r_{12}} \\ M_{18} &= -\frac{3 s_2^{(1)} h_1(kr_{12}) z_{12}}{4\pi i k r_{12}} \\ M_{25} &= \frac{s_2^{(0)} h_1(kr_{12}) k x_{12}}{4\pi r_{12}} \\ M_{26} &= -\frac{3 s_2^{(1)}}{4\pi i k r_{12}} \left(h_1(kr_{12}) - \frac{k h_2(kr_{12}) x_{12}^2}{r_{12}} \right) \\ M_{27} &= \frac{3 s_2^{(1)} h_2(kr_{12}) x_{12} y_{12}}{4\pi i r_{12}^2} \end{aligned}$$

$$\begin{aligned}
M_{28} &= \frac{3s_2^{(1)}h_2(kr_{12})x_{12}z_{12}}{4\pi i r_{12}^2} \\
M_{35} &= \frac{s_2^{(0)}h_1(kr_{12})ky_{12}}{4\pi r_{12}} \\
M_{36} &= M_{27} \\
M_{37} &= -\frac{3s_2^{(1)}}{4\pi i k r_{12}}\left(h_1(kr_{12}) - \frac{kh_2(kr_{12})y_{12}^2}{r_{12}}\right) \\
M_{38} &= \frac{3s_2^{(1)}h_2(kr_{12})y_{12}z_{12}}{4\pi i r_{12}^2} \\
M_{45} &= \frac{s_2^{(0)}h_1(kr_{12})kz_{12}}{4\pi r_{12}} \\
M_{46} &= M_{28} \\
M_{47} &= M_{38} \\
M_{48} &= -\frac{3s_2^{(1)}}{4\pi i k r_{12}}\left(h_1(kr_{12}) - \frac{kh_2(kr_{12})z_{12}^2}{r_{12}}\right)
\end{aligned}$$

These matrix elements make up the upper right block of the matrix on the previous page. The lower left block is found by exchanging the indices (1,2) in the upper right block.

We emphasize here that these matrix elements are not necessarily meant to be enlightening as regards the two-scatterer problem. They are simply matrix elements of a big matrix that will have to be inverted numerically anyway. We list them here only for completeness.

6.7 More than two scatterers

It is straightforward to extend this formalism to the case of many scatterers. One has for N scatterers a matrix of dimension $4N$,

$$\begin{pmatrix}
\mathbf{1} & \boldsymbol{M}(1,2) & \boldsymbol{M}(1,3) & \cdots & \boldsymbol{M}(1,N) \\
\boldsymbol{M}(2,1) & \mathbf{1} & \boldsymbol{M}(2,3) & \cdots & \boldsymbol{M}(2,N) \\
\boldsymbol{M}(3,1) & \boldsymbol{M}(3,2) & \mathbf{1} & \cdots & \boldsymbol{M}(3,N) \\
\vdots & \vdots & \vdots & \ddots & \vdots \\
\boldsymbol{M}(N,1) & \boldsymbol{M}(N,2) & \boldsymbol{M}(N,3) & \cdots & \mathbf{1}
\end{pmatrix}, \tag{6.78}$$

where $\mathbf{1}$ is a 4×4 unit matrix, and $\boldsymbol{M}(i,j)$ is a 4×4 matrix identical to the upper right block of our two-scatterer matrix, with the indices replaced as $(1,2) \rightarrow (i,j)$.

6.8 Conclusion

In this section we have presented a method for extending the point scatterer model to higher partial waves in both two and three dimensions. This allows the solution of multiple scattering problems at higher energies, where simple s-wave scattering no longer is valid. In the 2D case, the solution involves the inversion of a matrix which is of dimension $N(2L+1)$, where N is the number of scatterers, and L is the highest angular momentum accounted for by the solution. In 3D, the dimension of the matrix is $N(3L+1)$. Thus, using standard numerical techniques, we can solve multiple scattering problems which heretofore required the solution of extremely difficult integral equations.

Chapter 7

Light Scattering by Point Dipoles

7.1 Introduction

In recent years, there have been incredible advances in the cooling and trapping of atoms. Densities as high as 10^{15} atoms $\cdot$ cm^{-3} [15] and temperatures as low as 100 nK [31] have been achieved. Today one can easily produce a cloud of atoms which are much closer together than a wavelength of a photon which is resonant with a particular atomic transition. It is even possible to create clouds that are so cold and dense that the wavelength of the *atoms themselves* is much larger than the atomic spacing. One might expect interesting light scattering properties of such a dense gas, perhaps with properties similar to the proximity resonance, discussed in Chapters 3 and 4. Although the atoms in a cloud are in motion, their speed is quite small in comparison with the velocity of light, so that the approximation of treating the atoms as fixed dipole light scatterers is not too far-fetched. With this in mind, I will consider the problem of light scattering from a collection of stationary point dipole light scatterers. This light can be either resonantly or non-resonantly scattered. Dipole scattering for light is analogous to s-wave scattering for scalar waves. The light scattering problem is a bit more involved, precisely because it is a vector wave, and not only is it necessary to track the strength of the scattered electric field, but also its polarization. Apart from this detail, the multiple scattering of a vector wave is similar to the scalar wave case.

7.2 Dipole scattering

Imagine a perfect dipole light source at the origin, oscillating with a harmonic time dependence $e^{-i\omega t}$. The dipole has a moment $\boldsymbol{p}$, which for atoms will be related to the local electric field through $\boldsymbol{p} = \alpha \boldsymbol{E}$, where α is the dynamic polarizability of the atom. Everywhere apart from the origin, the radiated (scattered) electric field is [23, pg. 395],

$$\boldsymbol{E}_s = k^2(\hat{\boldsymbol{r}} \times \boldsymbol{p}) \times \hat{\boldsymbol{r}} \frac{e^{ikr}}{r} + [3\hat{\boldsymbol{r}}(\hat{\boldsymbol{r}} \cdot \boldsymbol{p}) - \boldsymbol{p}] \left(\frac{1}{r^3} - \frac{ik}{r^2} \right) e^{ikr}, \tag{7.1}$$

where an overall harmonic time dependence $e^{-i\omega t}$ has been factored out. The first term is the so-called *far field* radiation and the second is the *near field.* They are thus named because the far field falls off only as $1/r$, and thus survives to distances much larger than λ. The near field radiation, however, falls off as $1/r^2$, and therefore is not important far from the source. Normally, in the context of light scattering, one is primarily interested in the far field radiation. For our purposes, however, the near field radiation is extremely important, because we will consider dipoles that are situated much closer than a light wavelength to one another. In this case, it is primarily the *near field* of the neighboring dipoles that is felt by a particular scatterer. Furthermore, since we are explicitly including both near and far field terms, the effects of retardation are fully accounted for in the model.

Now, the scatterer is not radiating on its own. It is responding to an incident wave, $\boldsymbol{E}_0$, which determines the magnitude of the dipole moment $\boldsymbol{p}$ through the polarizability as stated above. So really we can write the full electric field as a sum of incident and scattered fields,

$$\boldsymbol{E}(\boldsymbol{r}) = \boldsymbol{E}_0(\boldsymbol{r}) + \boldsymbol{E}_s(\boldsymbol{r}), \tag{7.2}$$

or,

$$\boldsymbol{E}(\boldsymbol{r}) = \boldsymbol{E}_0(\boldsymbol{r}) + \alpha k^2(\hat{\boldsymbol{r}} \times \boldsymbol{E}_0(0)) \times \hat{\boldsymbol{r}} \frac{e^{ikr}}{r} + \alpha \left[3\hat{\boldsymbol{r}}(\hat{\boldsymbol{r}} \cdot \boldsymbol{E}_0(0)) - \boldsymbol{E}_0(0)\right] \left(\frac{1}{r^3} - \frac{ik}{r^2} \right) e^{ikr}, \tag{7.3}$$

where we have expressed the scattered field in terms of the incident electric field at the location of the dipole. Here we already have an idea about how one might include other scatterers into this method. We now have an expression for the full electric field, given only knowledge of the incident wave. If we then put another scatterer somewhere in that field, we would know how that second scatterer would respond to that *generalized* incident wave, neglecting the effects of multiple scattering. But it is precisely the multiple scattering that gives rise to effects like the proximity resonance, so we must learn how to incorporate multiple scattering. Actually, it is rather simple, particularly if the multiple scattering of scalar waves is understood. Instead of a scalar, there are *three* numbers at every point in space that get scattered and re-scattered – what it amounts to is that the two dipole problem involves the inversion of a 6 × 6 matrix instead of a 2 × 2 matrix. Let us see how that comes about.

We would like to decompose the compact vector notation of Eq. 7.1 into Cartesian coordinates, so that a definite matrix representation of the problem is defined. First we will look at the far field term:

$$\begin{aligned}(\hat{\boldsymbol{r}} \times \boldsymbol{p}) \times \hat{\boldsymbol{r}} &= \hat{\boldsymbol{x}} \left(\frac{z^2+y^2}{r^2} p_x - \frac{xy}{r^2} p_y - \frac{xz}{r^2} p_z \right) \\ &+ \hat{\boldsymbol{y}} \left(-\frac{xy}{r^2} p_x + \frac{x^2+z^2}{r^2} p_y - \frac{yz}{r^2} p_z \right) \\ &+ \hat{\boldsymbol{z}} \left(-\frac{xz}{r^2} p_x - \frac{yz}{r^2} p_y + \frac{x^2+y^2}{r^2} p_z \right). \qquad (7.4)\end{aligned}$$

Similarly, we have for the near field term:

$$\begin{aligned}3\hat{\boldsymbol{r}}(\hat{\boldsymbol{r}} \cdot \boldsymbol{p}) - \boldsymbol{p} &= \hat{\boldsymbol{x}} \left[\left(\frac{3x^2}{r^2} - 1 \right) p_x + \frac{3xy}{r^2} p_y + \frac{3xz}{r^2} p_z \right] \\ &+ \hat{\boldsymbol{y}} \left[\frac{3xy}{r^2} p_x + \left(\frac{3y^2}{r^2} - 1 \right) p_y + \frac{3yz}{r^2} p_z \right] \\ &+ \hat{\boldsymbol{z}} \left[\frac{3xz}{r^2} p_x + \frac{3yz}{r^2} p_y + \left(\frac{3z^2}{r^2} - 1 \right) p_z \right]. \qquad (7.5)\end{aligned}$$

Now the scattered field can be written as a matrix times a vector, where the vector represents the incident field at the scatterer location, which for the moment we assume to be at the origin:

$$\begin{aligned}\boldsymbol{E}_s(\boldsymbol{r}) &= \overbrace{\alpha e^{ikr} \left(\frac{1}{r^3} - \frac{ik}{r^2} \right) \begin{pmatrix} \frac{3x^2}{r^2} - 1 & \frac{3xy}{r^2} & \frac{3xz}{r^2} \\ \frac{3xy}{r^2} & \frac{3y^2}{r^2} - 1 & \frac{3yz}{r^2} \\ \frac{3xz}{r^2} & \frac{3yz}{r^2} & \frac{3z^2}{r^2} - 1 \end{pmatrix}}^{\mathcal{M}_n(\boldsymbol{r})} \begin{pmatrix} E_{0x}(0) \\ E_{0y}(0) \\ E_{0z}(0) \end{pmatrix} \\ &+ \underbrace{\alpha k^2 \frac{e^{ikr}}{r} \begin{pmatrix} \frac{y^2+z^2}{r^2} & -\frac{xy}{r^2} & -\frac{xz}{r^2} \\ -\frac{xy}{r^2} & \frac{x^2+z^2}{r^2} & -\frac{yz}{r^2} \\ -\frac{xz}{r^2} & -\frac{yz}{r^2} & \frac{x^2+y^2}{r^2} \end{pmatrix}}_{\mathcal{M}_f(\boldsymbol{r})} \begin{pmatrix} E_{0x}(0) \\ E_{0y}(0) \\ E_{0z}(0) \end{pmatrix}, \qquad (7.6)\end{aligned}$$

where the first matrix, $\mathcal{M}_n(\boldsymbol{r})$, involves the near field, and the second, $\mathcal{M}_f(\boldsymbol{r})$, the far field. If the scatterer were not at the origin, but rather at position $\boldsymbol{r}_i$ then the following prescription can be used to find the above matrices. We just replace $\boldsymbol{r} \to \boldsymbol{r} - \boldsymbol{r}_i$, that is:

$$x \rightarrow x - x_i \tag{7.7}$$

$$y \rightarrow y - y_i \tag{7.8}$$

$$z \rightarrow z - z_i \tag{7.9}$$

$$r \rightarrow r - r_i, \tag{7.10}$$

so that if we want to move the scatterer off the origin to $\boldsymbol{r}_i$, the scattered wave would be,

$$\boldsymbol{E}_s(\boldsymbol{r}) = [\mathcal{M}_n(\boldsymbol{r} - \boldsymbol{r}_i) + \mathcal{M}_f(\boldsymbol{r} - \boldsymbol{r}_i)]\boldsymbol{E}_0(\boldsymbol{r}_i) \tag{7.11}$$

So far, nothing much has been achieved. We have managed only to express the concise vector notation of Eq. 7.1 in much more cumbersome Cartesian coordinates. We will only begin to see the utility of this decomposition when we incorporate more than one scatterer into the works, and figure out how to deal with multiple scattering.

So how do we deal with more than one scatterer? Sometimes it is best to simply state the answer, and then explain it afterwards. This will be my approach here. For N point dipole scatterers at locations $\{\boldsymbol{r}_i\}$, the solution is:

$$\boldsymbol{E}(\boldsymbol{r}) = \boldsymbol{E}_0(\boldsymbol{r}) + \sum_{i=1}^{N}[\mathcal{M}_n(\boldsymbol{r} - \boldsymbol{r}_i) + \mathcal{M}_f(\boldsymbol{r} - \boldsymbol{r}_i)]\boldsymbol{E}_i(\boldsymbol{r}_i), \tag{7.12}$$

where,

$$\boldsymbol{E}_i(\boldsymbol{r}_i) = \boldsymbol{E}_0(\boldsymbol{r}_i) + \sum_{j\neq i}[\mathcal{M}_n(\boldsymbol{r}_i - \boldsymbol{r}_j) + \mathcal{M}_f(\boldsymbol{r}_i - \boldsymbol{r}_j)]\boldsymbol{E}_j(\boldsymbol{r}_j). \tag{7.13}$$

This should look familiar from the discussions of multiple scattering in Chapter 3 and Chapter 6. We see that the fields $\boldsymbol{E}_i(\boldsymbol{r}_i)$ behave as *effective* incident waves on scatterer i. That is, they contain, in addition to the incident wave $\boldsymbol{E}_0(\boldsymbol{r}_i)$, all the waves scattered from the other scatterers $j \neq i$ that eventually reach i. In fact, the only part of $\boldsymbol{E}_i(\boldsymbol{r})$ which is not contained in the full solution is that which leaves i and *never* comes back.

Eq. 7.13 is in fact a matrix equation relating the $\boldsymbol{E}_i(\boldsymbol{r}_i)$ to the $\boldsymbol{E}_0(\boldsymbol{r}_i)$. One can solve for $\boldsymbol{E}_i(\boldsymbol{r}_i)$ by inverting a matrix of dimension $3N \times 3N$, and then plug the $\boldsymbol{E}_i(\boldsymbol{r}_i)$ into Eq. 7.12 to get the full scattering solution, where the number of dipoles is N.

7.3 The matrix $\mathcal{M}$

For completeness, let's write down this matrix equation for the case of scattering off two nearby dipoles, and the extension to many dipoles will then be straightforward. We have the matrix equation,

$$\begin{pmatrix} \boldsymbol{E}_0(\boldsymbol{r}_1) \\ \boldsymbol{E}_0(\boldsymbol{r}_2) \end{pmatrix} = \mathcal{M} \begin{pmatrix} \boldsymbol{E}_1(\boldsymbol{r}_1) \\ \boldsymbol{E}_2(\boldsymbol{r}_2) \end{pmatrix}, \tag{7.14}$$

where we must remember that each vector $\boldsymbol{E}_0(\boldsymbol{r}_i), \boldsymbol{E}_i(\boldsymbol{r}_i)$ has three components each. The matrix $\mathcal{M}$ is given by the symmetric matrix,

$$\mathcal{M} = \begin{pmatrix} 1 & 0 & 0 & M_{14} & M_{15} & M_{16} \\ 0 & 1 & 0 & M_{15} & M_{25} & M_{26} \\ 0 & 0 & 1 & M_{16} & M_{26} & M_{36} \\ M_{14} & M_{15} & M_{16} & 1 & 0 & 0 \\ M_{15} & M_{25} & M_{26} & 0 & 1 & 0 \\ M_{16} & M_{26} & M_{36} & 0 & 0 & 1 \end{pmatrix}. \tag{7.15}$$

The six non-trivial matrix elements are, with some obvious abbreviations:

$$\begin{aligned}
M_{14} &= -\alpha e^{ik|\boldsymbol{r}_{12}|}\left\{\frac{k^2\left(y_{12}^2+z_{12}^2\right)}{|\boldsymbol{r}_{12}|^3}+\left(\frac{1}{|\boldsymbol{r}_{12}|^3}-\frac{ik}{|\boldsymbol{r}_{12}|^2}\right)\left(\frac{3x_{12}^2}{|\boldsymbol{r}_{12}|^2}-1\right)\right\} \\
M_{25} &= -\alpha e^{ik|\boldsymbol{r}_{12}|}\left\{\frac{k^2\left(x_{12}^2+z_{12}^2\right)}{|\boldsymbol{r}_{12}|^3}+\left(\frac{1}{|\boldsymbol{r}_{12}|^3}-\frac{ik}{|\boldsymbol{r}_{12}|^2}\right)\left(\frac{3y_{12}^2}{|\boldsymbol{r}_{12}|^2}-1\right)\right\} \\
M_{36} &= -\alpha e^{ik|\boldsymbol{r}_{12}|}\left\{\frac{k^2\left(x_{12}^2+y_{12}^2\right)}{|\boldsymbol{r}_{12}|^3}+\left(\frac{1}{|\boldsymbol{r}_{12}|^3}-\frac{ik}{|\boldsymbol{r}_{12}|^2}\right)\left(\frac{3z_{12}^2}{|\boldsymbol{r}_{12}|^2}-1\right)\right\} \\
M_{15} &= \alpha e^{ik|\boldsymbol{r}_{12}|}\left\{\frac{k^2x_{12}y_{12}}{|\boldsymbol{r}_{12}|^3}-\left(\frac{1}{|\boldsymbol{r}_{12}|^3}-\frac{ik}{|\boldsymbol{r}_{12}|^2}\right)\left(\frac{3x_{12}y_{12}}{|\boldsymbol{r}_{12}|^2}\right)\right\} \\
M_{16} &= \alpha e^{ik|\boldsymbol{r}_{12}|}\left\{\frac{k^2x_{12}z_{12}}{|\boldsymbol{r}_{12}|^3}-\left(\frac{1}{|\boldsymbol{r}_{12}|^3}-\frac{ik}{|\boldsymbol{r}_{12}|^2}\right)\left(\frac{3x_{12}z_{12}}{|\boldsymbol{r}_{12}|^2}\right)\right\} \\
M_{26} &= \alpha e^{ik|\boldsymbol{r}_{12}|}\left\{\frac{k^2y_{12}z_{12}}{|\boldsymbol{r}_{12}|^3}-\left(\frac{1}{|\boldsymbol{r}_{12}|^3}-\frac{ik}{|\boldsymbol{r}_{12}|^2}\right)\left(\frac{3y_{12}z_{12}}{|\boldsymbol{r}_{12}|^2}\right)\right\}.
\end{aligned}$$

The first term in each expression is due to the far field scattering, and the second is due to the near field. To generalize this to N dipoles, we can write the matrix $\mathcal{M}$ as,

$$\mathcal{M} = \begin{pmatrix} \mathbf{1} & \boldsymbol{M}(1,2) & \boldsymbol{M}(1,3) & \cdots & \boldsymbol{M}(1,N) \\ \boldsymbol{M}(2,1) & \mathbf{1} & \boldsymbol{M}(2,3) & \cdots & \boldsymbol{M}(2,N) \\ \boldsymbol{M}(3,1) & \boldsymbol{M}(3,2) & \mathbf{1} & \cdots & \boldsymbol{M}(3,N) \\ \vdots & \vdots & \vdots & \ddots & \vdots \\ \boldsymbol{M}(N,1) & \boldsymbol{M}(N,2) & \boldsymbol{M}(N,3) & \cdots & \mathbf{1} \end{pmatrix}, \tag{7.16}$$

where $\mathbf{1}$ is a 3×3 unit matrix, and $\boldsymbol{M}(i,j)$ is given by the upper right 3×3 block of the matrix in Eq. 7.15, with replacement of the indices on $\boldsymbol{r}_1, \boldsymbol{r}_2$ with $1 \to i, 2 \to j$.

We can also derive a simple formula for the total cross section, σ_{tot}, using the optical theorem,

$$\sigma_{\text{tot}} = \frac{4\pi}{k}\text{Im}\left[\boldsymbol{\epsilon}_0^* \cdot \boldsymbol{f}(\boldsymbol{k} = \boldsymbol{k}_0)\right], \tag{7.17}$$

where $\boldsymbol{\epsilon}_0$ is the polarization of the incident wave, and $\boldsymbol{f}(\theta)$ is the vector scattering amplitude, which is defined by the asymtotic solution [23],

$$\boldsymbol{E}(\boldsymbol{r}) = \boldsymbol{E}_0(\boldsymbol{r}) + \boldsymbol{f}(\theta,\phi)\frac{e^{ikr}}{r}. \tag{7.18}$$

We will implicitly assume, without loss of generality, an incident wave of the form,

$$\boldsymbol{E}_0(\boldsymbol{r}) = e^{ikz}\boldsymbol{\epsilon}_0. \tag{7.19}$$

We take for $\boldsymbol{E}(\boldsymbol{r})$ the form given by Eq. 7.12. However, since we are interested in $\boldsymbol{f}(\theta,\phi)$, we may drop all the near field terms, because they do not survive into the asymtotic region. We have,

$$\begin{aligned} \boldsymbol{E}(\boldsymbol{r}) &= \boldsymbol{E}_0(\boldsymbol{r}) + \sum_{i=1}^{N} \mathcal{M}_f(\boldsymbol{r} - r_i)\boldsymbol{E}_i(\boldsymbol{r}_i) \\ &= \boldsymbol{E}_0(\boldsymbol{r}) + \boldsymbol{f}(\theta,\phi)\frac{e^{ikr}}{r}. \end{aligned} \tag{7.20}$$

Expanding this equation, we have,

$$\boldsymbol{f}(\theta,\phi)\frac{e^{ikr}}{r} = \sum_{i=1}^{N} \alpha k^2 \frac{e^{ik|\boldsymbol{r}-\boldsymbol{r}_i|}}{|\boldsymbol{r}-\boldsymbol{r}_i|} \begin{pmatrix} \frac{(y-y_i)^2+(z-z_i)^2}{|\boldsymbol{r}-\boldsymbol{r}_i|^2} & -\frac{(x-x_i)(y-y_i)}{|\boldsymbol{r}-\boldsymbol{r}_i|^2} & -\frac{(x-x_i)(z-z_i)}{|\boldsymbol{r}-\boldsymbol{r}_i|^2} \\ -\frac{(x-x_i)(y-y_i)}{|\boldsymbol{r}-\boldsymbol{r}_i|^2} & \frac{(x-x_i)^2+(z-z_i)^2}{|\boldsymbol{r}-\boldsymbol{r}_i|^2} & -\frac{(y-y_i)(z-z_i)}{|\boldsymbol{r}-\boldsymbol{r}_i|^2} \\ -\frac{(x-x_i)(z-z_i)}{|\boldsymbol{r}-\boldsymbol{r}_i|^2} & -\frac{(y-y_i)(z-z_i)}{|\boldsymbol{r}-\boldsymbol{r}_i|^2} & \frac{(x-x_i)^2+(y-y_i)^2}{|\boldsymbol{r}-\boldsymbol{r}_i|^2} \end{pmatrix} \begin{pmatrix} E_{ix}(\boldsymbol{r}_i) \\ E_{iy}(\boldsymbol{r}_i) \\ E_{iz}(\boldsymbol{r}_i) \end{pmatrix}. \tag{7.21}$$

Now, in the asymtotic region, we have that $r \gg r_i$. Thus we may safely drop all the x_i, y_i, z_i compared with x, y, z, except in the exponential. In addition, since we are only interested in the forward direction, we can set $x, y = 0; z = r$ everywhere. We have then,

$$\begin{aligned} \boldsymbol{f}(\boldsymbol{k}=\boldsymbol{k}_0)\frac{e^{ikr}}{r} &= \alpha k^2 \frac{e^{ikr}}{r}\sum_{i=1}^{N} e^{-ik\hat{\boldsymbol{r}}\cdot\boldsymbol{r}_i} \begin{pmatrix} 1 & 0 & 0 \\ 0 & 1 & 0 \\ 0 & 0 & 0 \end{pmatrix} \begin{pmatrix} E_{ix}(\boldsymbol{r}_i) \\ E_{iy}(\boldsymbol{r}_i) \\ E_{iz}(\boldsymbol{r}_i) \end{pmatrix} \\ &= \alpha k^2 \frac{e^{ikr}}{r}\sum_{i=1}^{N} e^{-ikz_i} \begin{pmatrix} E_{ix}(\boldsymbol{r}_i) \\ E_{iy}(\boldsymbol{r}_i) \\ 0 \end{pmatrix}, \end{aligned} \tag{7.22}$$

where we have used the fact that $\hat{\boldsymbol{r}} \cdot \boldsymbol{r}_i = z_i$ in the forward direction. Using this asymtotic expression and the optical theorem, we find that the cross section is,

$$\sigma_{\text{tot}} = 4\pi k \sum_{i=1}^{N} \text{Im}\left[\alpha e^{-ikz_i}\left\{\epsilon_{0x}^{*} E_{ix}(\boldsymbol{r}_i) + \epsilon_{0y}^{*} E_{iy}(\boldsymbol{r}_i)\right\}\right]. \tag{7.23}$$

This gives the cross section in terms of the effective incident waves on all the dipoles $\boldsymbol{E}_i(\boldsymbol{r}_i)$, which must be found by first inverting the matrix $\mathcal{M}$. We can solve for the $\boldsymbol{E}_i(\boldsymbol{r}_i)$ thus,

$$E_{i\alpha}(\boldsymbol{r}_i) = \sum_{\beta=1}^{3N} [\mathcal{M}^{-1}]_{3i+\alpha,\beta} E_{0\beta}, \tag{7.24}$$

where the index i labels a particular dipole, the index $\alpha = 1, 2, 3$ specifies the x, y, z component of the field, and the index β runs from 1 to $3N$. $E_{0\beta}$ is the βth component of the $3N$ dimensional vector of the incident wave evaluated at the dipole locations,

$$\boldsymbol{E}_0 = \begin{pmatrix} E_{0x}(\boldsymbol{r}_1) \\ E_{0y}(\boldsymbol{r}_1) \\ E_{0z}(\boldsymbol{r}_1) \\ \vdots \\ E_{0x}(\boldsymbol{r}_N) \\ E_{0y}(\boldsymbol{r}_N) \\ E_{0z}(\boldsymbol{r}_N) \end{pmatrix}. \tag{7.25}$$

7.4 The dynamic polarizability

We now want to apply this model to a pair of dipoles. However, before we do so, we must decide upon a form for the dynamic polarizability, $\alpha(k)$. We are not allowed to choose an arbitrary function of k, because there is the unitary condition of the optical theorem, which limits the class of polarizabilities allowed for unitary scatterers. The optical theorem relates $\mathrm{Im}\,[\alpha(k)]$ to $|\alpha(k)|^2$. We will now derive this relation.

For the purposes of this section, we will assume without loss of generality an incident wave along the x-axis, linearly polarized along the z-axis,

$$\boldsymbol{E}_0(\boldsymbol{r}) = e^{ikx}\hat{\boldsymbol{z}}. \tag{7.26}$$

This incident wave illuminates a single dipole at the origin. We want to find the total cross section of this dipole by finding the differential cross section and integrating over angles. The differential cross section is defined by [23],

$$\frac{d\sigma}{d\Omega} = \frac{r^2\,|\boldsymbol{\epsilon}_s^* \cdot \boldsymbol{E}_s|^2}{|\boldsymbol{\epsilon}_0^* \cdot \boldsymbol{E}_0|^2}, \tag{7.27}$$

where $\boldsymbol{\epsilon}_s$ is the polarization of the scattered wave, and $\boldsymbol{\epsilon}_0$ is the polarization of the incident wave. The complex conjugates are necessary to correctly handle the possibility of circular polarization, which in the present case does not apply. Using Eq. 7.6 and keeping only the far field terms, one can easily show that for the incident wave given by Eq. 7.26, the scattered field is,

$$\boldsymbol{E}_s(\boldsymbol{r}) = \alpha k^2 \frac{e^{ikr}}{r}\left(-\frac{xz}{r^2}\hat{\boldsymbol{x}} - \frac{yz}{r^2}\hat{\boldsymbol{y}} + \frac{x^2+y^2}{r^2}\hat{\boldsymbol{z}}\right). \tag{7.28}$$

The polarization vector $\boldsymbol{\epsilon}_s$ is just $\boldsymbol{E}_s(\boldsymbol{r})/|\boldsymbol{E}_s(\boldsymbol{r})|$. Taking the dot products appearing in Eq. 7.27, we find,

$$\begin{aligned} r^2\,|\boldsymbol{\epsilon}_s^* \cdot \boldsymbol{E}_s|^2 &= |\alpha|^2 k^4 \sin^2\theta \\ |\boldsymbol{\epsilon}_0^* \cdot \boldsymbol{E}_0|^2 &= 1, \end{aligned} \tag{7.29}$$

so that the differential cross section is,

$$\frac{d\sigma}{d\Omega} = |\alpha|^2 k^4 \sin^2\theta. \tag{7.30}$$

We can easily integrate this over angles to find the total cross section:

$$\begin{aligned} \sigma_{\mathrm{tot}} &= \int \frac{d\sigma}{d\Omega}\,d\Omega \\ &= |\alpha|^2 k^4 \int_0^{2\pi}\int_0^{\pi} \sin^3\theta\;d\theta\;d\phi \\ &= \frac{8\pi}{3}k^4|\alpha|^2. \end{aligned} \tag{7.31}$$

This is the famous result of Rayleigh, where the k^4 dependence is ubiquitous in the scattering of light by small particles, when it is sufficient to take only the dipole term in the multipole expansion of the scattered field. In fact, it is the strong dependence of the total cross section on k that is responsible for the beautiful blue color of the sky.

Now we wish to relate this result to that given by the optical theorem,

$$\sigma_{\text{tot}} = \frac{4\pi}{k}\text{Im}\left[\boldsymbol{\epsilon}_0^* \cdot \boldsymbol{f}(\boldsymbol{k} = \boldsymbol{k}_0)\right]. \tag{7.32}$$

In our case, the forward direction is given by the angles $\theta = \pi/2, \phi = \pi$. Then the scattering amplitude in the forward direction is,

$$\boldsymbol{f}(\theta = \pi/2, \phi = \pi) = \alpha k^2 \hat{\boldsymbol{z}}. \tag{7.33}$$

Thus, the optical theorem implies,

$$\frac{8\pi}{3}k^4|\alpha|^2 = \frac{4\pi}{k}\text{Im}\left[\alpha k^2\right], \tag{7.34}$$

or,

$$\frac{2}{3}k^3|\alpha|^2 = \text{Im}[\alpha]. \tag{7.35}$$

A particular choice of $\alpha(k)$ which satisfies this relation, and has a resonance at $k = k_0$ with width $\Delta k = 2k_0^3\gamma$ is given by,

$$\alpha(k) = \frac{3\gamma/2}{k - k_0 - ik^3\gamma}. \tag{7.36}$$

We will use this form in the next section.

7.5 Two nearby dipoles

In Fig. 7.1, we plot the total cross section for two nearby resonant dipole scatterers. Proximity resonance-like features are apparent in the cross section. In contrast to the scalar wave (quantum mechanical) case, there are *four* resonances that appear in the cross section for just *two* scatterers. This is not surprising, because the poles of the scattering amplitude in the vector wave case come from the roots of the determinant of a 6×6 matrix, rather than a 2×2 matrix in the scalar wave case. Therefore, there will be more resonances per scatterer in vector wave scattering. However, we may still wonder why there are not six resonances in the cross section, since the matrix is 6×6. The reason is as follows. Indeed,

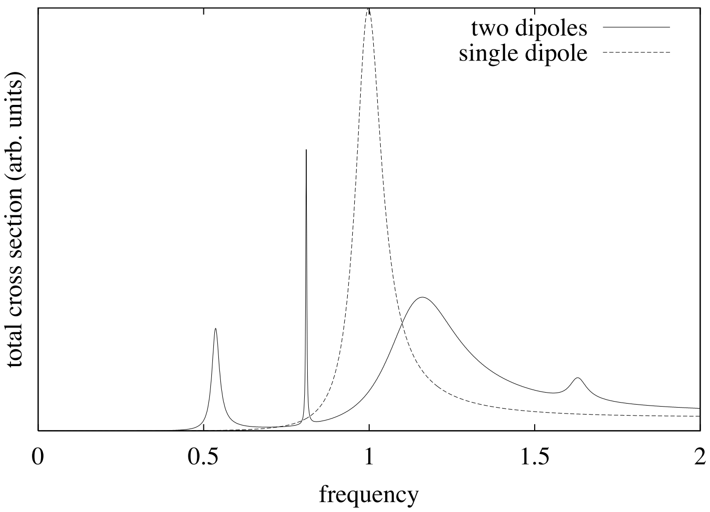

Figure 7.1: Total cross section versus energy for two resonant dipoles. The single scatterer resonance parameters were $\omega_0 = ck_0 = 1, \Delta\omega = 0.1$. The scatterers were located such that $k_0 d = 0.7$, where d is the separation. The single dipole cross section is also shown.

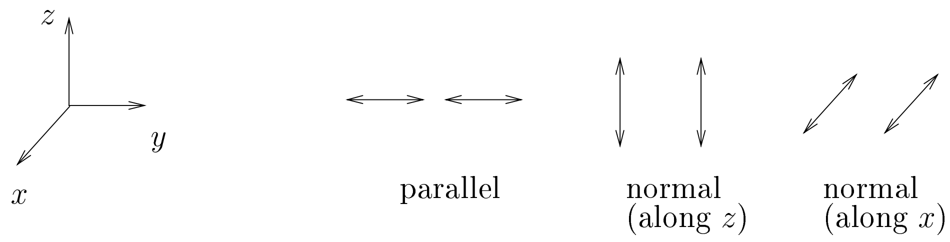

Figure 7.2: Shown are the oscillation directions of the individual dipole moments for the six modes of two dipole positioned along the y-axis. The first, which has both moments aligned along the line connecting the dipoles, is non-degenerate. This mode has a symmetric state and an antisymmetric state. The other modes have oscillation normal to the y-axis, and are degenerate. Each has a symmetric and antisymmetric state.

there six possible modes of oscillation for two dipoles, as shown in Fig 7.2. Three are symmetric, and three antisymmetric. Two of these modes have the dipoles oscillating *along* the line connecting them (two because one is symmetric, the other is antisymmetric). The other (four) modes have the dipoles oscillating *perpendicular* to this line. However, since there are *two* orthogonal directions perpendicular to this line, the perpendicular modes having the same symmetry will be degenerate with one another. This leaves a total of two non-degenerate modes (accounting for two peaks in the cross section), and four doubly-degenerate modes, (accounting for two more peaks in the cross section).

It is interesting to note that the antisymmetric resonance is shifted *down* in energy, and the symmetric peak is shifted *up*, in contrast to the scalar wave case. However, the splitting is symmetric about $\omega = \omega_0$, at least for the two largest peaks in the cross section. Also, it appears that the broad resonance has a width $\Gamma = 2\Gamma_0$, as in the scalar wave case.

I should note that after this method was derived, I found that a very similar method had been proposed much earlier by Purcell and Pennypacker, for the purpose of modelling the scattering of light off small, irregularly shaped interstellar dust grains [36]. In their method, the dipoles are placed on sites of a cubic lattice, and the scattering solution is found by iteration, rather than direct inversion of a matrix.

Chapter 8

Diffractive Orbits in an Open Microwave Billiard

8.1 Introduction

This thesis concludes with a departure from the topic of low energy scattering discussed in previous chapters – here we will explore the role of diffraction in determining the spectrum of an open quantum mechanical system.

In this chapter, we demonstrate the existence and significance of diffractive orbits in an open microwave billiard, both experimentally and theoretically. By diffractive orbits, we mean particular orbits that diffract off of a sharp edge of the system. It is found that such orbits strongly influence the transmission spectrum of the system, especially in the regime where there are no stable classical orbits. On resonance, the wavefunctions are influenced by both classical and diffractive orbits. Off resonance, the wavefunctions are determined by the constructive interference of multiple transient, nonperiodic orbits. Experimental, numerical, and semiclassical results are presented.

8.2 The resonator

Recently, Katine studied the transmission behavior of an open quantum billiard in the context of a two dimensional electron gas (2DEG) in a GaAs/AlGaAs heterostructure [25]. Their resonator was formed by a wall with a small aperture, called a quantum point contact (QPC), and an arc-shaped reflector. A schematic of this resonator is shown in Fig. 8.1. The voltage on the reflector could be varied, effectively moving the reflector towards or away from the wall. Their measurements showed a series of conductance peaks, analogous to those seen in a Fabry-Perot, as the reflector position was varied.

As we discuss below, the resonator considered here represents a new class of billiards, to our knowledge not previously studied in the literature. That is, the billiard is geometrically *open*, but in the stable regime, it is classically *closed.* In the unstable regime, the resonance properties of the billiard are determined in large part by *diffraction.*

The resonator shown in Fig. 8.1 has two distinct modes of operation. When the center of curvature of the reflector is to the left of the wall (the regime studied in [25]), then all classical paths starting from the QPC that hit the reflector remain forever in the region between wall and the reflector: the dynamics is stable and the periodic orbits can be semiclassically quantized. Each quantized mode of the resonator can be characterized by two quantum numbers (n, m), which represent the number of radial and angular nodes respectively. As the reflector-wall separation is varied, the conductance exhibits a peak each time one of these quantized modes is allowed. Once an electron is in the resonator, the only way for it to leave is by tunneling back through the QPC or by diffracting around the reflector; since both processes are slow, the resonances have narrow widths. Because the QPC is on the symmetry axis, only modes with even m can be excited. The states of the resonator in the stable regime bear a strong resemblance to a certain symmetry class of states in the lemon billiard. This class has even symmetry about the short axis of the lemon, and odd symmetry about the long axis. This connection will be explored more fully in Section 8.9.

When the center of curvature is to the right of the wall, however, the dynamics becomes unstable: all classical trajectories beginning at the QPC rapidly bounce out of the resonator, except for a single unstable periodic orbit along the axis of symmetry, which we will call the “horizontal” orbit [see Fig 8.1(b)]. The horizontal orbit is a member or a class of orbits which we call “geometric,” because their paths are governed by specular reflection off the wall and reflector, and do not undergo diffraction. Although the horizontal orbit returns to the QPC, it has a low probability of escaping the resonator there because the QPC is much smaller than the de Broglie wavelength of the electron. Because the horizontal orbit is the only periodic orbit in the unstable regime, one might expect resonant buildup only along the symmetry axis. Such a spectrum would be quasi-one-dimensional, with only the half-wavelength periodicity of a Fabry-Perot cavity. However, in numerical simulations

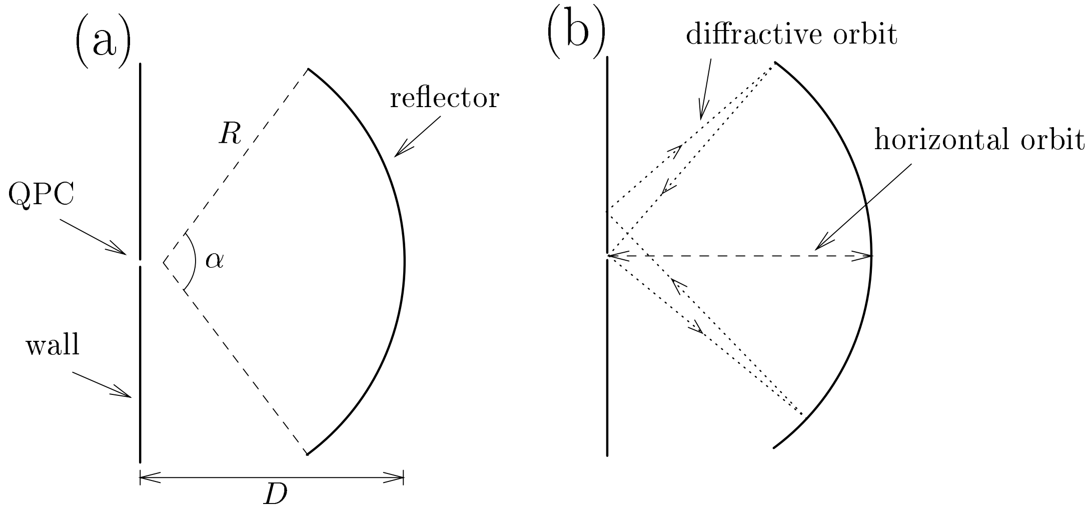

Figure 8.1: (a) A schematic of the mesoscopic resonator studied by Katine, with radius of curvature R, opening angle α, and reflector-wall separation D. Electrons impinge on the wall from the left, and the conductance to the region on the right is measured. (b) Two closed orbits of the unstable resonator: diffractive (dotted line), and horizontal (dashed line). These will be discussed later in the chapter.

it was found that there were other transmission resonances in the unstable regime which did not correspond to any classical periodic orbits [11]. It was proposed that these anomalous peaks are supported by diffraction off the tips of the reflector. Unfortunately, in the mesoscopic experiments, decoherence of the electron wave by impurities in the GaAs/AlGaAs heterostructure shortens the lifetime of the resonances, leaving insufficient energy resolution to resolve the diffractive peaks [48].

8.3 Experiment

Because of the problems of dissipation and decoherence in the mesoscopic experiments, we decided to investigate a parallel plate microwave resonator with a similar geometry. In microwave experiments, decoherence and dissipation are not a problem, the geometry of the resonator can be specified much more accurately, and the dynamical range of available wavelengths is much larger. The experimental setup is shown in Fig. 8.2. As was shown in Chapter 4, the equation governing the component of the electric field normal to the plates for the TEM mode is identical to the two-dimensional time-independent Schrödinger equation [17, 41, 42, 43]. Therefore, by studying the modes of parallel-plate resonators we

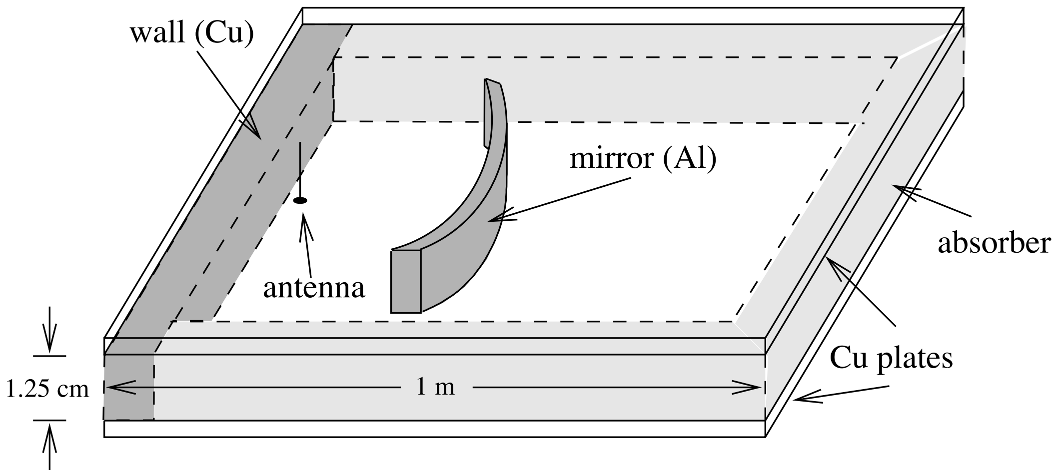

Figure 8.2: This is the microwave analog of the mesoscopic resonator studied by Katine. The antenna simulates the QPC; to reduce its coupling to the resonator, it is placed very close to the wall. The drawing is not to scale.

can gain insight into the behavior of two-dimensional solutions to the Schrödinger equation.

The resonator consisted of two parallel copper plates, 1 meter square, separated by a distance of 1.25 cm. One side of the resonator consisted of a copper wall. The other three sides were lined with a 11.5 cm thick layer of microwave absorber (C-RAM LF-79, Cuming Microwave Corp.) designed to provide 20 dB of attenuation in the reflected wave intensity in the range 0.6-40 GHz. The absorber prevented outgoing waves from returning to the resonator, thereby simulating an open system in the directions away from the wall. An antenna was inserted normal to the plates, 2 mm from the wall, to simulate the QPC. The curved reflector was formed from a rectangular aluminum rod bent into an arc with radius of curvature $R = 30.5$ cm. Various opening angles α were used: 115°, 112°, 109°, and 106°.

Instead of measuring the transmission of the resonator, we measured the reflection back from the antenna; for this we used an HP8720D network analyzer in “reflection” mode (the complex S_{11} parameter of the resonator was measured). We inferred the transmission probability $|T|^2$ via $|T|^2 = 1 - |R|^2$, where $R = S_{11}$ is the measured reflection coefficient. Because of the proximity of the antenna to the wall, it was only weakly coupled to the resonator; therefore, in the absence of the reflector, the transmission coefficient was close to zero. However, when the reflector was present, the transmission experienced pronounced maxima at certain frequencies.

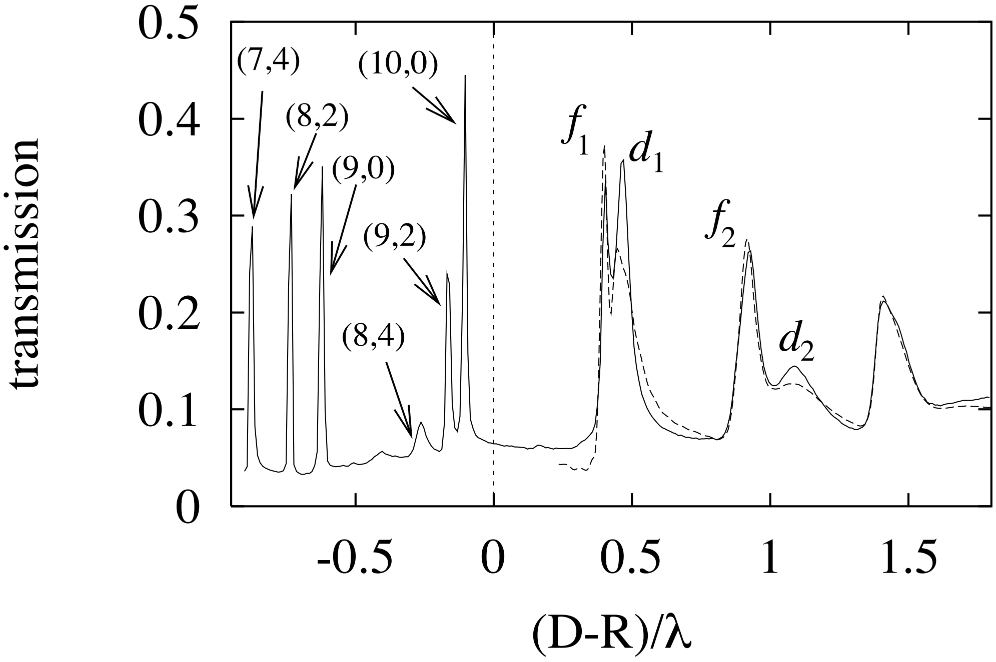

Figure 8.3: Experimental transmission versus reflector-wall separation at a fixed frequency of 5.63 GHz; i.e., $R = 5.7\lambda$. The stable/unstable transition point occurs at abscissa zero. In the stable regime, the peaks are labeled by their radial and angular quantum numbers (n, m). In the unstable regime, the diffractive resonances (labeled d) appear to the right of the Fabry-Perot peaks (labeled f). The dashed curve is the result of a semiclassical calculation which takes diffractive orbits into account (see text). The opening angle for the reflector was $\alpha = 106°$.

8.4 Results

In Fig. 8.3 we show a transmission spectrum at fixed frequency, as the distance between the wall and reflector is varied. In the stable regime, we see that the peaks are narrow and well defined. This is because the dynamics is stable in this regime: nearly all trajectories starting from the QPC that hit the reflector remain forever in the region between the wall and the reflector. In this regime, there exist invariant tori, which may be semiclassically quantized to produce the states of the stable resonator. Such a classical orbit is shown in Fig. 8.4, along with its quantum mechanical wavefunction counterpart. We see that the trajectory does not approach the region where the resonator is open. Thus, it behaves as if the cavity were *closed* – hence the narrow widths of the peaks in the stable

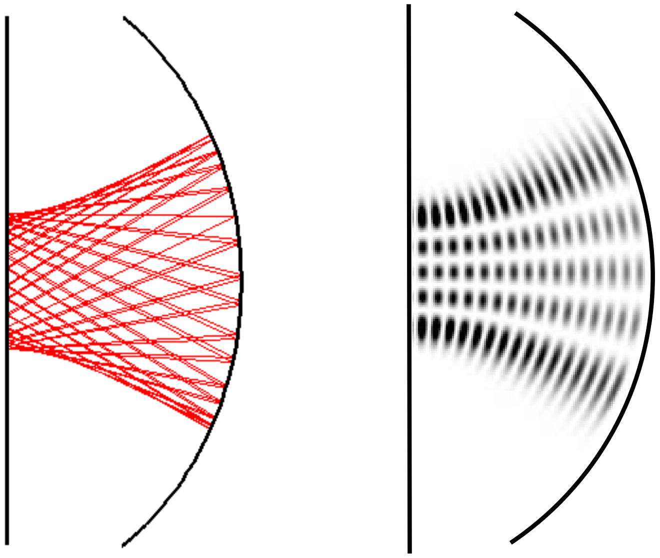

Figure 8.4: On the left, a classical trajectory starting at the QPC is shown, with the corresponding wavefunction on the right.

regime.

In the unstable regime, the transmission curve is quite different. Here, there are two types of resonances. The first type, labeled f in Fig. 8.3, is related to the horizontal orbit along the axis of symmetry, and bears some resemblance to a Fabry-Perot type resonance between two half-silvered mirrors. The second type, labeled d, is supported by diffraction off the tips of the reflector.

We verified that the d-peaks were indeed supported by diffraction by surrounding the tips of the reflector with microwave absorber and repeating the experiment, as indicated in Fig. 8.5. When this was done, the Fabry-Perot resonances were unaffected, but the diffractive peaks were entirely eliminated from the spectrum. This makes sense, because any ray coming near the tip would be absorbed and have no chance to return to the antenna.

The wavefunctions corresponding to peaks f_1 and d_1 were measured using the technique of Maier and Slater [30]. They showed that the frequency shift of a given resonance

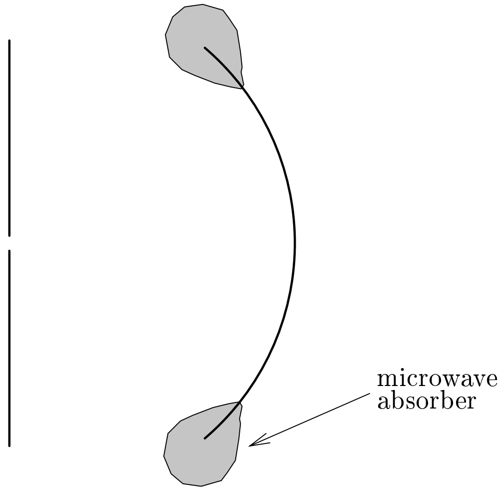

Figure 8.5: Diffractive peaks could be removed from the spectrum by placing microwave absorber near the tips of the reflector, as shown.

due to a small sphere of radius r_0 at a position (x, y) is given by

$$\frac{\omega^2 - \omega_0^2}{\omega_0^2} = 4\pi r_0^3 \left(\frac{1}{2} H_0^2(x,y) - E_0^2(x,y)\right), \tag{8.1}$$

where E_0 and H_0 are the unperturbed electric and magnetic fields. Thus, the frequency shift is proportional to the local intensity of the microwave field, and by measuring the shift as a function of the position of the sphere, the field intensity of a particular mode can be mapped out. Note that the frequency shift will be positive in regions where the magnetic field is large, and negative where the electric field is large. Also, the factor of 1/2 multiplying the magnetic field in Eq. 8.1 indicates that the sphere is a stronger perturbation to the electric field than the magnetic field. In our measurements, we found this to be the case: the shifts were predominantly negative. Appreciable positive shifts were only found at the nodes of the electric field, corresponding to maxima of the magnetic field.

Figure 8.6 shows theoretical quantum wavefunctions compared with experimentally measured frequency shifts for the resonances labeled by f_1 and d_1 in Fig. 8.3. The theoretical wavefunctions were generated using Edwards' wavelet method presented in [11]. The measured frequency shift is plotted as a function of sphere position. For these measurements, we used a steel bead of diameter 4.0 mm for the perturbation. The bead was rastered over the inside of the cavity by means of an external magnet. That way, the bead could be moved around inside the cavity without taking the cavity apart. It is important to note that the frequency shift is not proportional to E^2, but rather to $H^2/2 - E^2$. Therefore

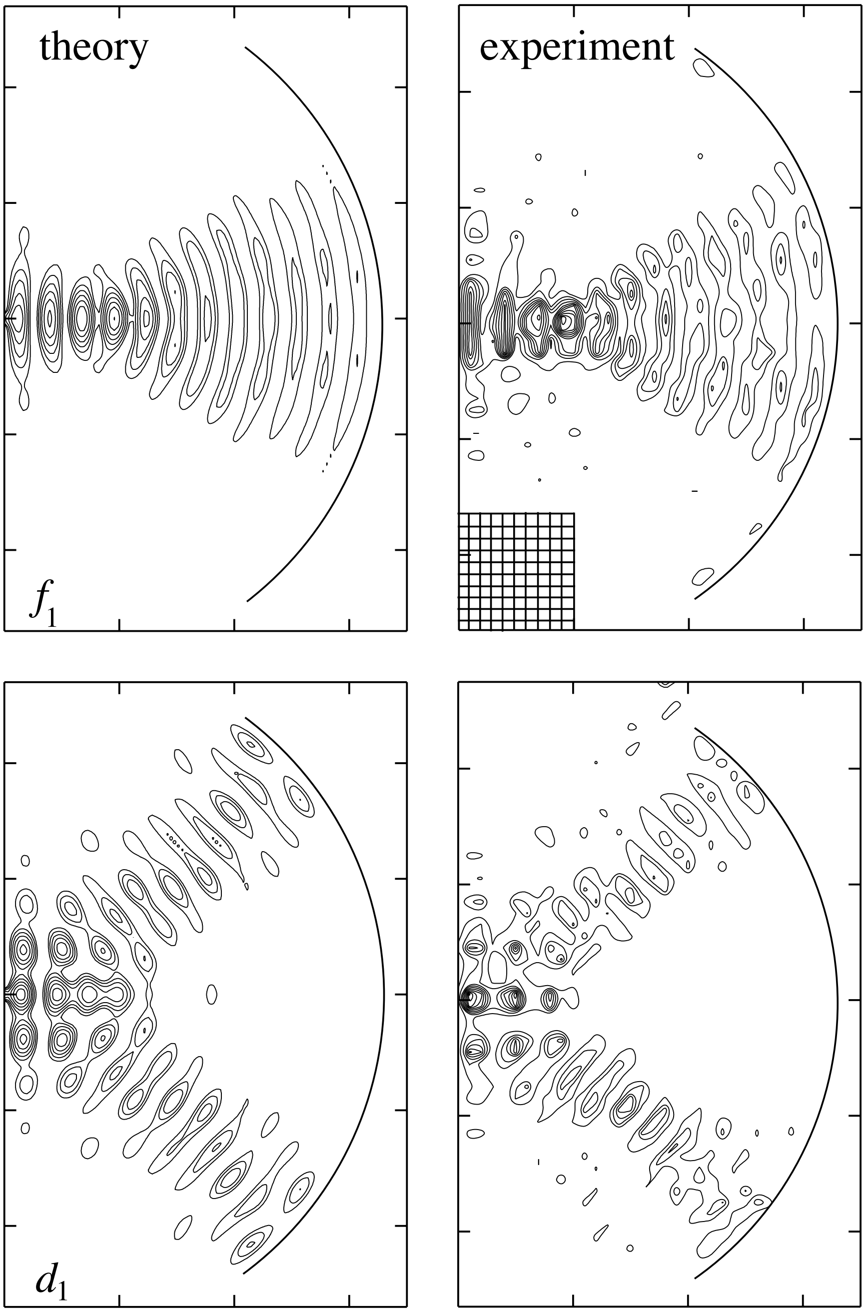

Figure 8.6: Comparison between theoretical quantum wavefunctions (left) and experimentally measured microwave frequency shifts (right). The two modes correspond to peaks f_1 and d_1, respectively, in Fig. 8.3. The wall is located on the left vertical axis in each plot, and the reflector position is indicated by the arc. The graph ticks are 10 cm apart. The fine grid indicates the spacing of the experimentally sampled points (grid spacing 1 cm).

we show only negative contour lines below 20% of the maximum negative shift, and thereby emphasize regions of strong electric field. The similarity between theory and experiment is striking.

The wavefunction labeled f_1 in Fig. 8.6 is clearly associated with the horizontal orbit along the axis of symmetry. Rays emanating from a point source located on the axis of symmetry next to the wall bounce off the reflector and come to an approximate focus about 10 cm from the source. The focus is approximate because of spherical (or in this case cylindrical) aberration.

Now we turn our attention to the state labeled d_1 in Fig. 8.6. As noted above, the only periodic orbit in the unstable regime is the horizontal orbit, along the axis of symmetry. The pictured wavefunction, however, clearly has very little amplitude along this periodic orbit. Instead the wavefunction has a band of higher amplitude running from the region of the tip of the mirror to the QPC, but in the unstable regime there is no *classical* periodic orbit that does this. Later in the chapter, it will be shown that states such as d_1 are supported by orbits that undergo *diffraction* off the tips of the reflector. One such orbit is shown in Fig. 8.1(b). Rays that hit the smooth surfaces of the reflector or wall undergo specular reflection, whereas the rays that hit near the reflector tips can be diffracted. A fraction of the wave amplitude can then return to the QPC from this region, thus setting up a *non-classical* closed orbit. All peaks labeled with a d in Fig. 8.3 are supported by such diffractive orbits.

Numerical calculations have shown that for energies off resonance, the quantum wavefunction is often intermediate between those shown for f_1 and d_1, in the sense that amplitude seems to be running from the QPC to some point between the center of the mirror and the tip [11]. This can be understood in terms of the interference of paths with each other as they “walk off” the horizontal orbit and escape the resonator. Thus diffraction does not necessarily play a major role in determining the off-resonance wavefunctions. However, diffraction *is* instrumental in determining the on-resonance wavefunctions underlying the conductance peaks d_1 and d_2 in Fig. 8.3.

Figure 8.7 shows a more global picture of the transmission properties of the resonator. Here we plot the transmission of the resonator as both the wavelength and the reflector-wall separation are varied. Each vertical slice through this figure is a frequency spectrum with fixed reflector position; the dotted line marks the classical transition from stable to unstable motion that occurs when the reflector’s center of curvature moves to the

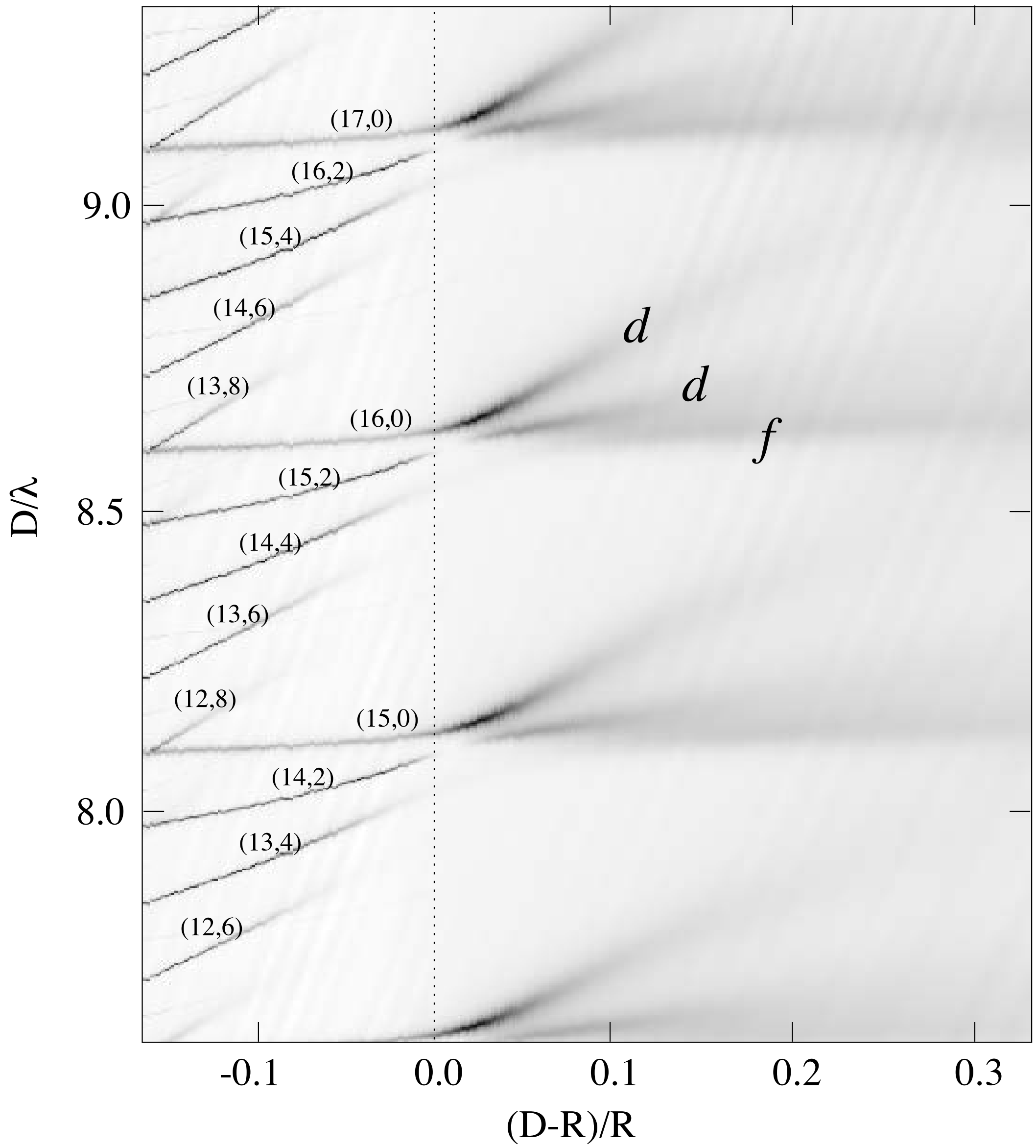

Figure 8.7: Experimental transmission versus reflector-wall separation and wavelength. High transmission regions are dark. On the left of the vertical dotted line is the stable regime, where the transmission peaks are sharp. The quantum numbers (n, m) are indicated for a few peaks. On the right is the unstable regime, where the resonances become wider and diffractive orbits become important. Transmission peaks supported by diffractive orbits are marked by d.

right of the QPC. The vertical axis indicates how many wavelengths fit along the horizontal orbit between the QPC and the reflector. The repetition of the resonance pattern every half-wavelength in the vertical direction is analogous to the half-wavelength periodicity of a Fabry-Perot cavity.

In the stable regime the peaks have been labeled with their quantum numbers, (n, m). The vertical axis is chosen to make the $m = 0$ resonance peaks approximately horizontal in this figure. As the stable/unstable transition is approached, the peaks with high m disappear one by one because their large angular sizes allow them to escape around the reflector.

At the stable/unstable transition, all of the resonances in a family would be approximately degenerate, but instead there is an avoided crossing. The level repulsion is caused by a coupling that is partly mediated by diffraction; this subject will be explored more thoroughly in Section 8.9.

In the unstable regime, the only remaining classical periodic orbit is the horizontal orbit, which itself becomes unstable. The Fabry-Perot peak (labeled f) is essentially quantized along the horizontal orbit, so its position shows a simple dependence on reflector position. It becomes broad in the unstable regime, with a lifetime given by the classical Lyapunov stability exponent of the horizontal orbit. Two diffractive resonances (labeled by d), are also visible; they separate from the Fabry-Perot type peak as the reflector is moved away from the wall.

The diffractive peaks labeled by d in Fig. 8.7 cannot be explained by semiclassical theory unless diffraction off the tips of the reflector is included. The semiclassical calculation involves launching a manifold of rays from the QPC, tracking their phases as they bounce off the reflector and cross caustics or foci, and then adding coherently the amplitudes of any orbits that return to the QPC. To include diffraction, we also allow for the fact that every ray that hits the tip of the reflector is scattered in all directions, with an angle-dependent amplitude [24, 27]. Any of the scattered rays that return to the QPC give an additional contribution to the conductance. The details of the semiclassical theory will be presented later in the chapter.

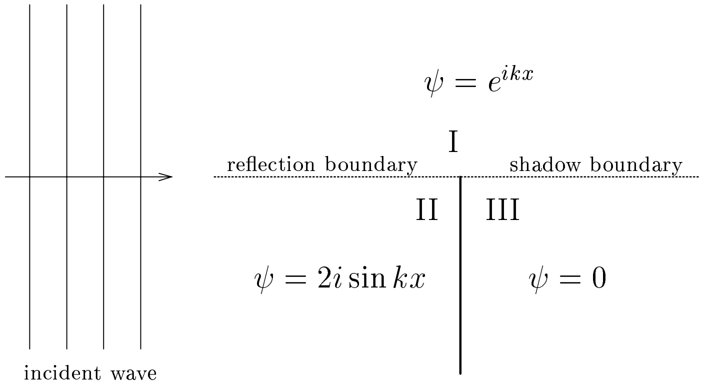

Figure 8.8: Diffraction from an infinite half-line in 2D.

8.5 Geometric theory of diffraction

Before we consider the problem of computing semiclassically the transmission properties of our resonator, let us study the simpler problem of diffraction of a plane wave off an infinite half-line in 2D. This problem will serve as a good introduction into the geometrical theory of diffraction, which will be used to include diffraction into the semiclassical propagator.

The problem is illustrated in Fig. 8.8. A plane wave e^{ikx} is normally incident on the half-line from the left. The half-line extends up from the middle of the figure, indicated by the dark line. We take the tip of the line to be our coordinate origin. Within the geometrical optics approximation, the problem is divided into three separate regions: that of transmission, reflection, and shadow, labelled I, II, and III, respectively. The values of the wavefunction in each region are indicated in the figure as well. In region I, the wave does not hit the wall and thus is unchanged within the geometric optics approximation. In region II, the wave is perfectly reflected and thus a standing sine wave is set up there. In region III, we have a perfect shadow region, which is completely dark. Along the reflection and shadow boundaries indicated, the solution is discontinuous. Of course, these discontinuities are not present in the exact solution; they are an artifact of the geometric approximation. As we shall see, it is the diffraction off the tip of the wall which corrects these discontinuities.

In 1953, Keller showed that one can think of diffraction as originating from a group of "diffracted rays" originating from the edge of the wall [26]. The idea is illustrated in Fig. 8.9. Away from the shadow and reflection boundaries, these diffracted rays have

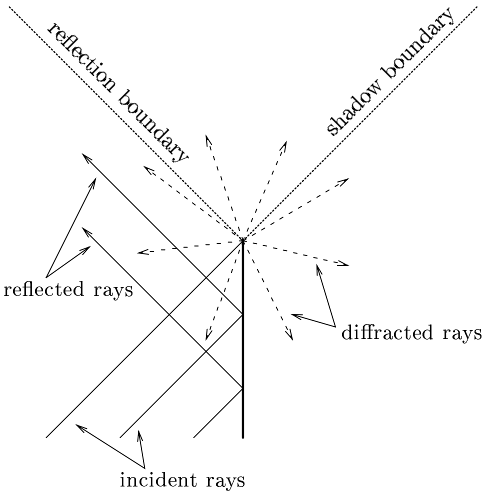

Figure 8.9: Reflected and diffracted rays from an infinite half-line. Diffracted rays are shown in dashed lines. The reflection and shadow boundaries are indicated. The wave is incident from the lower left corner of the figure, as indicated by the incident rays.

the form of an outgoing cylinder wave, multiplied by an angle dependent "diffraction coefficient." However, Keller's original theory was shown to be invalid on the reflection and shadow boundaries. A properly uniformized geometric theory of diffraction was developed by Kouyoumjian and Pathak [27]. The diffracted rays are multiplied by a suitable complex number which depends both on the angles of the incident and diffracted rays relative to the wall, as well as the distance from the edge. In this uniformized theory, the solution to the half-line is given by,

$$\psi(\boldsymbol{r}) = \psi_{\mathrm{g}}(\boldsymbol{r}) + D(\theta, \theta', r, k)e^{ikr}, \tag{8.2}$$

where $\psi_{\mathrm{g}}(\boldsymbol{r})$ is the solution given by geometrical optics, shown in Fig. 8.8. The diffraction coefficient $D(\theta, \theta', r, k)$ is given by [24, pg. 115],[1]

$$\begin{aligned} D(\theta, \theta', r, k) &= -\mathrm{sgn}(a_i)K\left(|a_i|\sqrt{kr}\right) + \mathrm{sgn}(a_r)K\left(|a_r|\sqrt{kr}\right), \\ a_{i,r} &= \sqrt{2}\cos\left(\frac{\theta \mp \theta'}{2}\right), \end{aligned} \tag{8.3}$$

and $K(x)$ is a modified Fresnel integral:

$$K(x) = \frac{1}{\sqrt{\pi}}e^{-ix^2 - i\pi/4}\int_x^\infty e^{it^2}\,dt. \tag{8.4}$$

---

[1] Note that the expression given in Ref. [24] is the complex conjugate of the expression above, because the convention for the time dependence of the fields taken in Ref. [24] is $e^{i\omega t}$, whereas we take the opposite convention, $e^{-i\omega t}$.

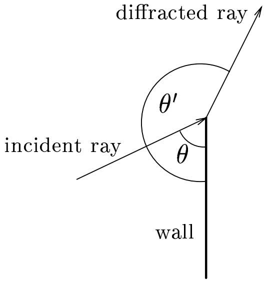

Figure 8.10: Angles of the incident and diffracted ray for use in Eq. 8.3.

The angles θ, θ' are shown in Fig. 8.10. In our case, $\theta = \pi/2$, because the incident wave is normal to the wall. In addition, in Eq. 8.2 we understand that the origin of the coordinate system is at the tip of the half-line.

In Fig. 8.11 we compare the result of Eq. 8.2 to the exact solution and to the Kirchoff approximation for the half-line (see Appendix A). The prediction of geometric optics is also shown. We find very good agreement between the exact solution, the uniform geometric theory, and Kirchoff approximation. Note especially that the discontinuities on the shadow and reflection boundaries are completely removed by the uniform theory.

8.6 Semiclassics in the energy domain

Now we turn back to the problem of calculating the transmission properties of our resonator. We need to find an expression for the Green function for the resonator, because the transmission can be easily written in terms of the diagonal part of the energy Green function [6]:

$$T(E) \propto \mathrm{Re}\left[iG(\boldsymbol{r}_{\mathrm{QPC}}, \boldsymbol{r}_{\mathrm{QPC}}, E)\right], \tag{8.5}$$

where $\boldsymbol{r}_{\mathrm{QPC}}$ is the center of the QPC. The reason only $\boldsymbol{r}_{\mathrm{QPC}}$ enters is because all waves enter our resonator at that point. Now, the complex number $G(\boldsymbol{r}_{\mathrm{QPC}}, \boldsymbol{r}_{\mathrm{QPC}}, E)$ is just the amplitude for returning to $\boldsymbol{r}_{\mathrm{QPC}}$, having launched a point source of waves beginning at $\boldsymbol{r}_{\mathrm{QPC}}$ at energy E. If a significant fraction of the rays making up this point source return to $\boldsymbol{r}_{\mathrm{QPC}}$ in phase, then $G(\boldsymbol{r}_{\mathrm{QPC}}, \boldsymbol{r}_{\mathrm{QPC}}, E)$ will be appreciable, and significant buildup of a wavefunction in the resonator will be achieved. This is the physical reason for $G(\boldsymbol{r}_{\mathrm{QPC}}, \boldsymbol{r}_{\mathrm{QPC}}, E)$ appearing in Eq. 8.5.

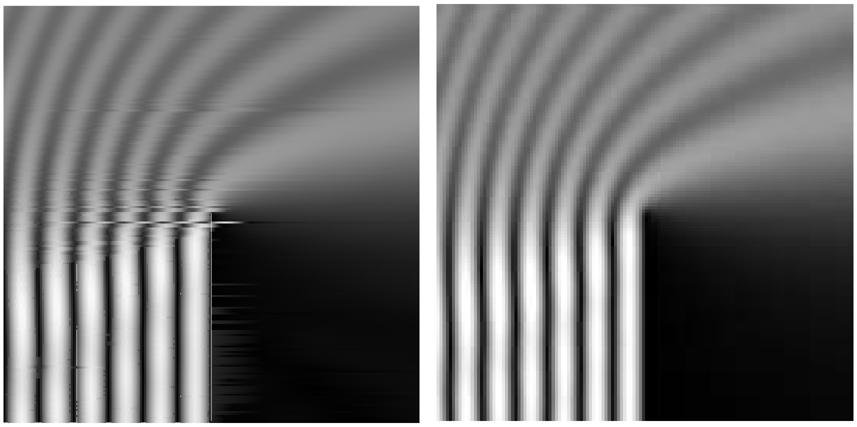

Exact solution Uniform geometric theory

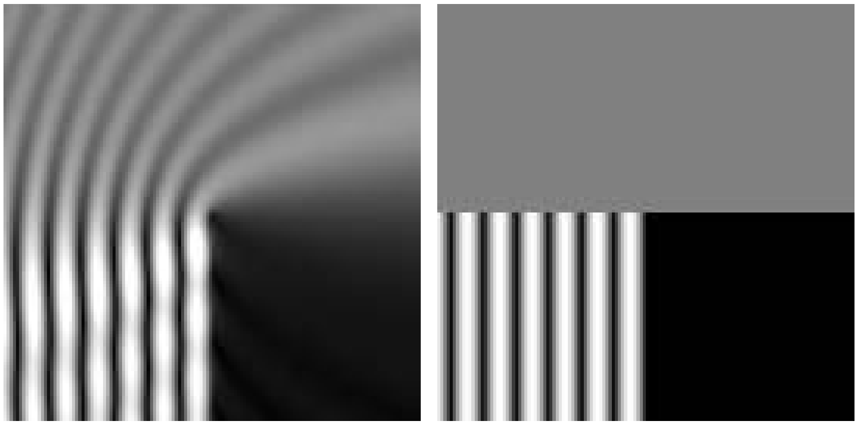

Kirchoff approximation Geometric optics

Figure 8.11: Comparison of the exact solution, the uniform geometrical theory, the Kirchoff approximation, and the geometric optics approximation for the diffraction of quantum particle off an infinite half-line screen. The screen extends from the lower center to the center of the picture. Plotted is the norm of the wavefunction, $|\psi|$. Note the stark discontinuities on the shadow and reflection boundaries in the geometric optics approximation. Regions of high probability amplitude are light.

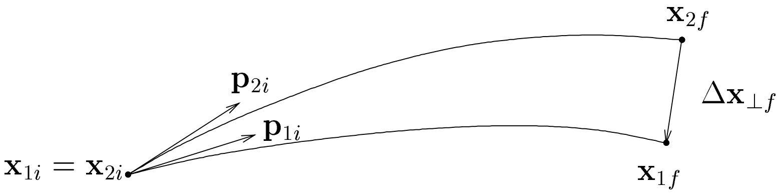

$$\Delta\mathbf{x}_{\perp f} = \mathbf{x}_{2f} - \mathbf{x}_{1f}$$
$$\Delta\mathbf{p}_{\perp i} = \mathbf{p}_{2i} - \mathbf{p}_{1i}$$

Figure 8.12: Two trajectories launched from the same point with slightly different momenta $\boldsymbol{p}_{1i}$ and $\boldsymbol{p}_{2i}$. Each momentum has the same magnitude; only the directions are different. This is the reason for the subscript $\perp$ in $\Delta\boldsymbol{p}_{\perp i}$. The labels i, f stand for initial and final.

Geometric orbits in the semiclassical propagator

The 2D semiclassical energy Green function $G_{\rm sc}(\boldsymbol{r}, \boldsymbol{r}', E)$ can be written as a sum over paths from $\boldsymbol{r}$ to $\boldsymbol{r}'$ thus [19],

$$G_{\rm sc}(\boldsymbol{r}, \boldsymbol{r}', E) = \frac{2\pi}{(2\pi i)^{3/2}} \sum_{\rm paths} \frac{1}{\sqrt{A}} \exp\left[iS(\boldsymbol{r}, \boldsymbol{r}') - i\pi\mu/2\right], \tag{8.6}$$

where A is a stability coefficient, $S(\boldsymbol{r}, \boldsymbol{r}')$ is the action, and μ is the Maslov index for the path. The coefficient A is given by,

$$A = \frac{\partial \boldsymbol{x}_{\perp f}}{\partial \boldsymbol{p}_{\perp i}} = \lim_{\Delta \boldsymbol{p}_{\perp i} \to 0} \frac{\Delta \boldsymbol{x}_{\perp f}}{\Delta \boldsymbol{p}_{\perp i}}, \tag{8.7}$$

where the vectors $\Delta\boldsymbol{x}_{\perp f}, \Delta\boldsymbol{p}_{\perp i}$ are indicated in Fig. 8.12. The coefficient A describes the stability of trajectories beginning from a particular point in phase space. If A is small, then the trajectories are stable. If A is large, then small changes in the initial direction of the trajectory lead to large displacements in the final positions: the trajectory is unstable. More precisely, if the distance $\Delta\boldsymbol{x}_{\perp f}$ grows exponentially with the length of the trajectories, we say that they are unstable. If $\Delta\boldsymbol{x}_{\perp f}$ grows only linearly, then the trajectories are stable.

For the case of our resonator in the unstable regime, only one type of orbit enters into the sum in Eq. 8.6: the horizontal orbit. Therefore, in order to find the contributions of the geometric orbits to the transmission spectrum, we need only to find the actions ($S = kl$, where l is the length of the orbit) and stability coefficients A for the primary horizontal orbit and its repetitions. In addition, we need to keep track of the Maslov index for each orbit. A series of such orbits, together with the associated Maslov indices, is indicated in Fig. 8.13(a). In this figure, the QPC/wall is located at the lower part of each diagram,

(a) Geometric terms

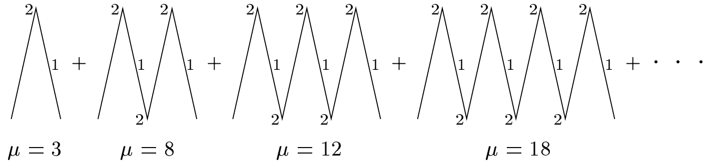

(b) Diffractive terms

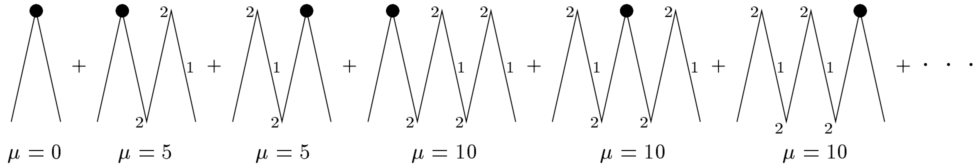

Figure 8.13: Diagrams of orbits included into the semiclassical Green function in Eq. 8.6. In (a), the horizontal orbits are shown. The upper vertices represent bounces off the reflector, while the lower vertices signify reflections off the QPC. The Maslov indices are shown for each part of each orbit, and the total index is given below each diagram. In (b), the diffractive orbits are shown. The filled circle represents a diffraction event, where the term is multiplied by the diffraction coefficient, D. After a diffractive event, the return path does not acquire a Maslov index of 1, because it is a diffracted ray; only the specularly reflected rays participate in the caustic.

while the reflector is located at the upper part. Each upward (downward) sloping line segment represents part of a trajectory from the QPC (reflector) to the reflector (QPC). Maslov indices of $\mu = 2$ are indicated for points where the wave is reflected at the wall or arc-reflector, and an index of $\mu = 1$ is acquired each time the ray passes though the focus on its return from the reflector toward the wall.

Using only the horizontal orbit, we have calculated a transmission spectrum for the resonator in the unstable regime, shown in Fig. 8.14. For this calculation, the sum in Eq. 8.6 was cut off after the 20th term, that is, orbits of up to 20 round trips were included in the sum. The half-wavelength periodicity of the spectrum is clearly seen in the figure. Upon comparison with Fig. 8.3, we see that the peak positions match very well with the experimentally measured spectrum. Note, however, the absence of the peaks corresponding to diffractive orbits which are present in Fig. 8.3. It is to the calculation of these absent resonances that we now turn.

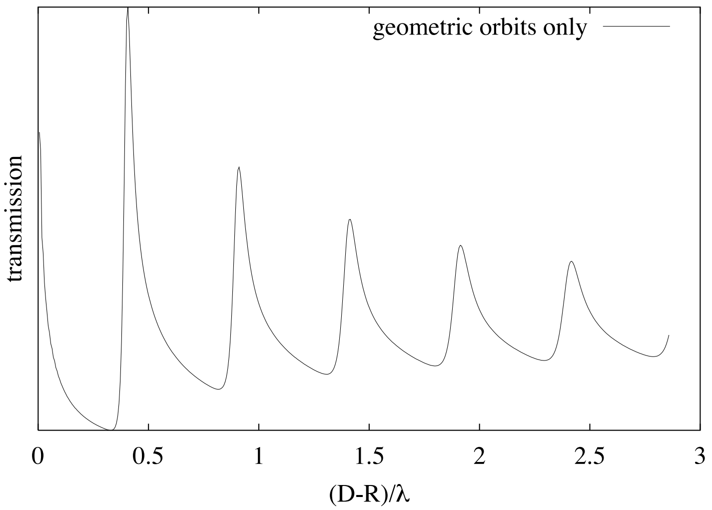

Figure 8.14: Semiclassical transmission including only the geometric orbits. The data is for fixed energy, corresponding to $kR = 40$, with the distance between the wall and reflector varied along the x-axis.

Diffractive orbits in the semiclassical propagator

So far, the Green function in Eq. 8.6 includes paths which undergo free evolution under the free particle Hamiltonian, including bounces off the wall and mirror. In order to calculate the spectral properties of the resonator semiclassically, diffractive orbits must be included into the sum over paths which form the semiclassical propagator. This problem has been studied by a number of authors [34, 39, 47]. In the literature, much attention has been focused on finding the effects of diffraction on the spectra of closed systems. However, in closed systems, diffraction generally plays a minor role. This is because of the overwhelming number of unstable periodic orbits present that do not involve diffraction in closed systems. In this section, these methods will be extended to include open systems.

For our purposes, it is sufficient to include diffraction at the level of a single diffraction event per orbit. Although multiply diffracted orbits strictly belong in the semiclassical sum, in practice they can be safely neglected. This is because of the amplitude of an incident ray on the reflector tip is subsequently sprayed in all directions, so that only a small part returns in a direction that eventually leads it back to the QPC. Therefore, we will consider only singly diffracted orbits. The Green function is the product of three amplitudes: the first for going from the starting point to the point of diffraction, the second for the

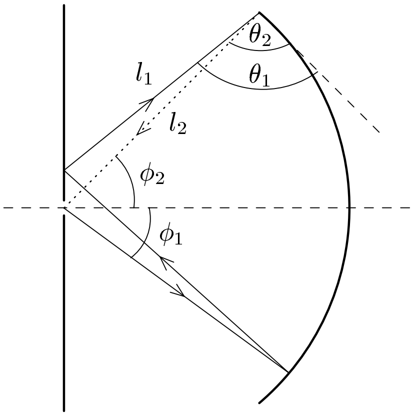

Figure 8.15: Here is shown the various angles relevant to a particular diffractive orbit entering into the semiclassical Green function in Eq. 8.8. The first leg of the orbit, l_1, is drawn with a solid line, whereas the second leg, l_2, is drawn with a dotted line. This orbit corresponds to the third term in the sum shown in Fig. 8.13(b).

diffraction event itself, and the third for going from the diffraction point to the final point, as follows:

$$\begin{aligned} G_{\text{diff}}(\boldsymbol{r},\boldsymbol{r}',E) &= G_{\text{sc}}(\boldsymbol{r},\boldsymbol{r}_d,E)D(l_1,l_2,\theta_1,\theta_2,E)G_{\text{sc}}(\boldsymbol{r}_d,\boldsymbol{r}',E) \\ &= -\frac{1}{2\pi i}\sum_{\text{paths}}\left\{\frac{D(l_1,l_2,\theta_1,\theta_2,E)}{\sqrt{A_1A_2}}\cos\phi_1\cos\phi_2\times\right. \\ &\qquad \left.\exp\left[i(S_1+S_1)-i\pi(\mu_1+\mu_2)/2\right]\right\}, \end{aligned} \tag{8.8}$$

where the diffraction event occurs at position $\boldsymbol{r}_d$, and the total path from $\boldsymbol{r}$ to $\boldsymbol{r}'$ is made up of two legs, one of length $l_1 = |\boldsymbol{r}-\boldsymbol{r}_d|$, with stability coefficient A_1, and the other of length $l_2 = |\boldsymbol{r}'-\boldsymbol{r}_d|$, with stability coefficient A_2. Each of these legs has an action $S_1 = kl_1, S_2 = kl_2$ and Maslov index μ_1, μ_2 associated with it. The factors $\cos\phi_1, \cos\phi_2$ represent the coupling of each leg to the QPC, and will be discussed in the next section. The various parameters are illustrated in Fig. 8.15 for one of the shorter orbits, corresponding to the third term in Fig. 8.13(b). In that figure, the first few terms entering into Eq. 8.8 are shown, where diffraction events are represented by filled circles.

The diffraction coefficient $D(l_1,l_2,\theta_1,\theta_2,E)$ depends on the lengths of each leg as well as the angles that the incident and diffracted ray make with the surface at the tip of the obstacle. These various lengths and angles are shown in Fig. 8.15. The diffraction coefficient in the sum above is similar to that appearing in our study of the half-line, differing only in

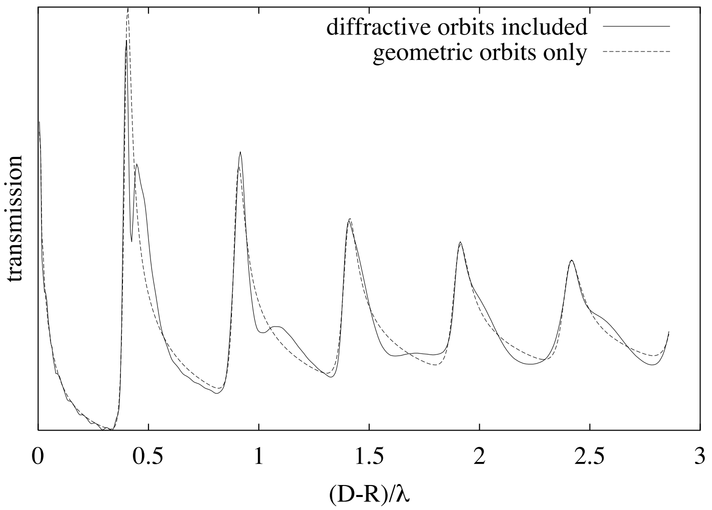

Figure 8.16: Semiclassical transmission including both the geometric and diffractive orbits. The data is for fixed energy, corresponding to $kR = 40$, with the distance between the wall and reflector varied along the x-axis. The result without diffraction is shown with a dashed line for comparison.

the argument of the Fresnel integral.[2] It is given by,

$$\begin{aligned} D(\theta_1, \theta_2, l_1, l_2, k) &= -\mathrm{sgn}(a_i) K\left(|a_i|\sqrt{\frac{kl_1l_2}{l_1+l_2}}\right) + \mathrm{sgn}(a_r) K\left(|a_r|\sqrt{\frac{kl_1l_2}{l_1+l_2}}\right), \quad (8.9) \\ a_{i,r} &= \sqrt{2}\cos\left(\frac{\theta_1 \mp \theta_2}{2}\right), \end{aligned}$$

where, as before, $K(x)$ is a modified Fresnel integral:

$$K(x) = \frac{1}{\sqrt{\pi}} e^{-ix^2 - i\pi/4} \int_x^\infty e^{it^2}\, dt. \tag{8.10}$$

The effect of the diffractive terms in the sum is shown in Fig. 8.16. For this calculation, all orbits with a single diffractive event up to 20 round trips between the wall and mirror were included in the sum. We see that the effect of the diffractive terms is to modulate the geometric result, with new peaks appearing to the right of the geometric peaks. The theoretical curve appearing in Fig. 8.16 is overlaid with the experimental data in Fig. 8.3; the agreement between theory and experiment is quite good, both in the peak positions and widths of the geometric and diffractive peaks. We emphasize here that the

---

[2] The reason for the difference in the argument of the Fresnel integral is that in the half-line case the incident wave was plane ($l_1 \to \infty$), whereas in the present case the incident wave is a cylindrical wave emanating from the QPC.

semiclassical prediction breaks down for reflector/wall separations near $D = R$, because there the focus approaches the point where the Green function is evaluated, so that the semiclassical prediction diverges. This is the reason for the large transmission calculated at $D = R$.

In Fig. 8.17, we plot the semiclassically calculated transmission of the resonator in the unstable regime versus both reflector/wall separation and wavelength. The data uses an identical parameter set as that of the experimental data shown in Fig. 8.7. The separation of the diffractive peaks from the Fabry-Perot peaks with increasing reflector/wall separation is quite clear. Two diffractive peaks per geometric peak are visible. The half-wavelength periodicity is also apparent. The similarity between theory and experiment in these two figures is impressive.

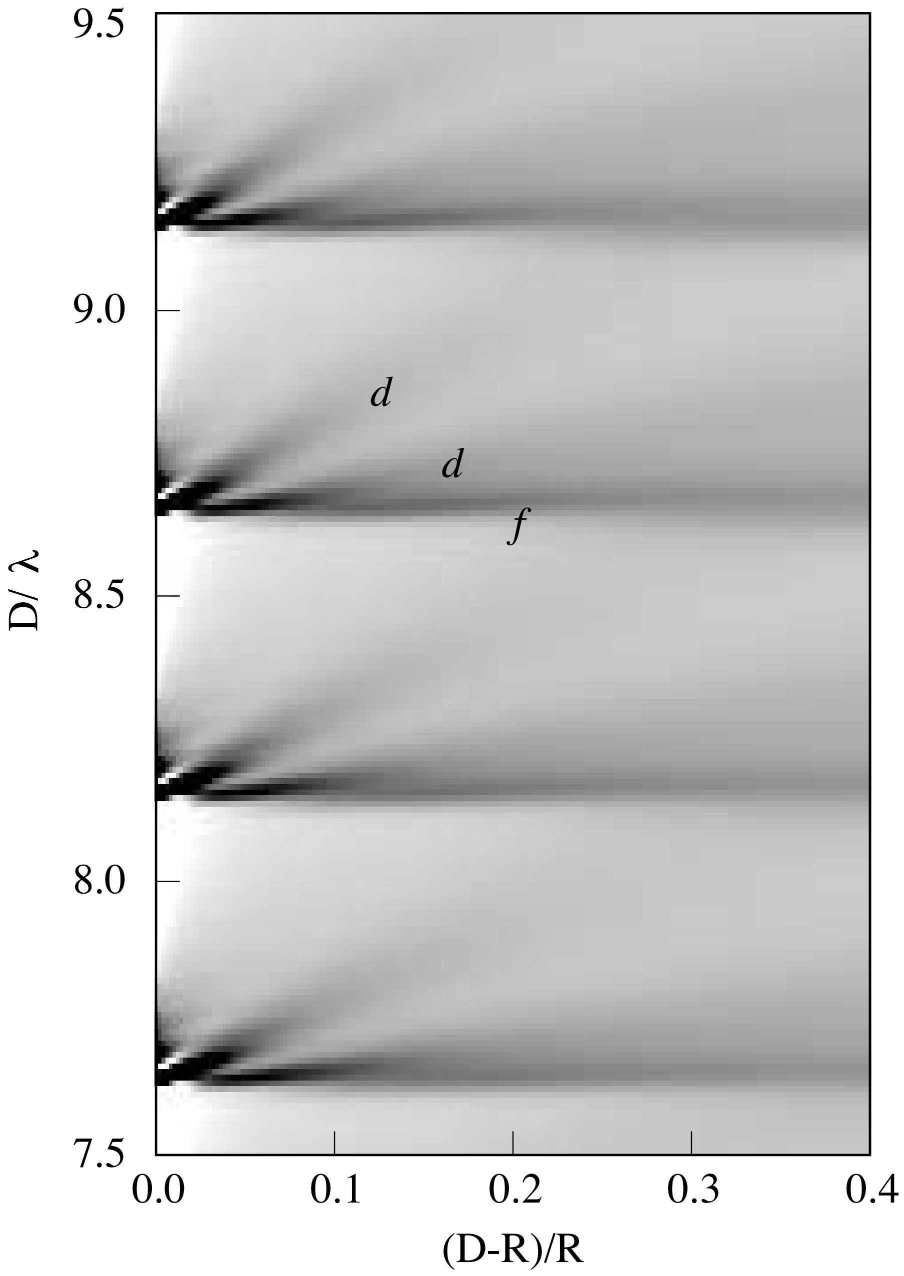

Figure 8.17: Semiclassical conductance plot of the resonator versus wavelength and reflector position in the unstable regime. The plot is exactly analogous to the experimental data shown on the right side of Fig. 8.7. Note that the semiclassical prediction is not valid near $D = R$ (see text).

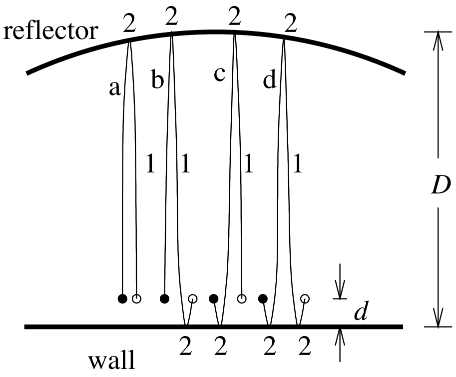

Figure 8.18: Four orbits associated with the shortest horizontal orbit when the antenna is displaced from the wall. The trajectories start from the filled circles and end on the closed circles. These circles are really the same point, namely the antenna position. They are displaced from each other in the figure so that the four distinct paths are visible. The Maslov indices acquired on each segment of each orbit are indicated. The antenna is a distance d away from the wall, and the horizontal distance from the wall to the reflector is D.

Family of horizontal orbits		
orbit	length	Maslov index
a	$2(D-d)$	3
b	$2D$	5
c	$2D$	5
d	$2(D+d)$	7

Table 8.1: Lengths and Maslov indices for the orbits shown in Fig. 8.18.

8.7 Maslov indices

In the experiment, the antenna is placed very close to, but not exactly at the wall. This means there are in fact *four* orbits associated with each single orbit in the billiard when the source is placed exactly at the wall. These four orbits for the shortest horizontal orbit are shown in Fig. 8.18. Each orbit in this family has a different total Maslov index and length, which are summarized in Table 8.1 We can find the effect of grouping these four orbits into a single orbit by computing the following sum,

$$Ae^{iS_{\text{eff}}-i\pi\mu_{\text{eff}}/2} = \sum_{n=a,b,c,d} e^{iS_n - i\pi\mu_n/2}, \tag{8.11}$$

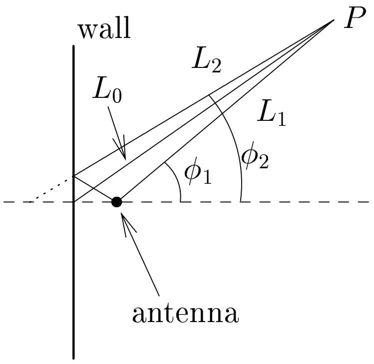

Figure 8.19: Two trajectories arriving at the antenna from slightly different angles. The antenna is a distance d from the wall, as in the previous discussion.

where the sum is over the four orbits as $d \to 0$. The coefficient A will be found by doing the sum. We expect the effective action for the orbit, S_{eff}, to be just the distance $2kD$, and the effective Maslov index, μ_{eff}, will be found by doing the sum. We have,

$$\begin{aligned} Ae^{iS_{\text{eff}}-i\pi\mu_{\text{eff}}/2} &= e^{2ik(D-d)-3\pi i/2} + 2e^{2ikD-5\pi i/2} + e^{2ik(D+d)-7\pi i/2} \\ &= e^{2ikD-5\pi i/2}\left(2 - e^{2ikd} - e^{-2ikd}\right) \\ &= e^{2ikD-5\pi i/2}\left(2 - 2\cos(2kd)\right) \\ &\approx (2kd)^2\, e^{2ikD-5\pi i/2}. \end{aligned} \tag{8.12}$$

Thus we have that $A = (2kd)^2$, $\mu_{\text{eff}} = 5$, and $S_{\text{eff}} = 2kD$, as expected.

We can do a similar analysis on orbits coming to the antenna at an angle in order to prove that the coupling to the antenna varies as $\cos\phi$, as stated in Eq. 8.8. Referring to Fig. 8.19, we have a source of rays beginning at the point P, which find their way to the antenna. There are two paths leading to the antenna. The direct path has length L_1 and Maslov index $\mu_1 = 0$. The second path first bounces off the wall before arriving at the antenna, and has length L_2 and Maslov index $\mu_2 = 1$. We want to combine these two paths into a single trajectory, by doing a sum over the two trajectories as was done above, in order to find the effective action and Maslov index for the trajectory. We further define the length L_0, which is the distance between P and the intersection of the wall with the axis of symmetry. The two lengths L_1 and L_1 are given by,

$$\begin{aligned} L_1 &= \sqrt{(L_0\cos\phi - d)^2 + (L_0\sin\phi)^2} \\ &\approx L_0 - d\cos\phi, \end{aligned} \tag{8.13}$$

and,

$$\begin{aligned} L_2 &= \sqrt{(L_0\cos\phi + d)^2 + (L_0 \sin\phi)^2} \\ &\approx L_0 + d\cos\phi, \end{aligned} \tag{8.14}$$

where ϕ is the angle between the trajectory L and the x-axis. Our sum over orbits is then,

$$\begin{aligned} e^{iS_{\text{eff}} - i\pi\mu_{\text{eff}}/2} &= e^{iS_1} + e^{iS_2 - i\pi} \\ &= e^{ik(L_0 - d\cos\phi)} + e^{ik(L_0 + d\cos\phi) - i\pi} \\ &= e^{ikL_0} e^{-i\pi/2}\left(e^{-ikd\cos\phi + i\pi/2} + e^{ikd\cos\phi - i\pi/2}\right) \\ &= 2\sin(kd\cos\phi) e^{ikL_0} e^{-i\pi/2} \\ &\approx 2kd\cos\phi e^{ikL_0} e^{-i\pi/2}. \end{aligned} \tag{8.15}$$

As expected, the effective action for the two paths is just $S_{\text{eff}} = kL_0$, and the Maslov index is $\mu_{\text{eff}} = 1$. The factor $\cos\phi$ appearing above is exactly the angular dependent coupling coefficient appearing in Eq. 8.8. This is just the simple angular dependence of a p-wave point source.

8.8 Semiclassics in the time domain

Further evidence of diffractive orbits in the transmission spectrum can be obtained by analyzing the spectrum in the time domain. The two representations are related by the Fourier transform:

$$g(t) = \int_{-\infty}^{\infty} S_{11}(\omega) e^{i\omega t}\, dt. \tag{8.16}$$

Here $g(t)$ represents the amplitude for a pulse launched from the QPC at time $t = 0$ to return at time t. That is, if a short pulse were emitted from the antenna at time $t = 0$, echos would return to the antenna at certain later times. These echos are indicated by peaks in the return spectrum. In Fig. 8.20, we plot the amplitude $|g(t)|$ as a function of time for the resonator in the stable and unstable regimes, where the time has been normalized into units of the radius of curvature of the reflector via $t \to L/c$, where L is the length of the orbit, and $c \equiv 1$. In the stable regime, the echos persist for hundreds of bounces, indicating that indeed the dynamics is stable in this regime. However, in the unstable regime, the echos are significantly reduced in amplitude after only a few returns. We have verified that the decay of the return peak amplitudes $|g(t)|^2$ in the unstable regime is accurately predicted

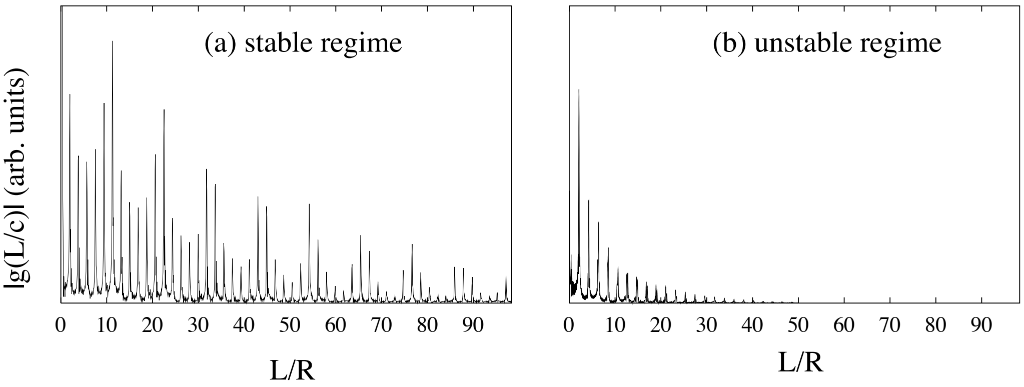

Figure 8.20: Experimental return spectra in the (a) stable and (b) unstable regime. Time has been converted to the ratio L/R, where L is the length of the orbit. For these plots the opening angle was 115°, and the reflector-wall separation was 28.5 cm and 32.5 cm, respectively.

by $e^{-\lambda ct/L}$, where c is the speed of light, λ is the Lyapunov exponent, and L is the length of the horizontal orbit.

In Fig. 8.21, we show an expanded view of some of the return peaks shown in Fig. 8.20(b). Of importance here is the splitting of the return peaks which is visible on echos 5-9. This splitting is due to the coexistence of orbits which slightly different periods. The longer of these orbits is just the horizontal orbit, which appears on the right of each group. The left peak of each group is made up of a family of diffractive orbits of nearly the same length. We have done a quantitative study of the lengths of the closed orbits and find excellent agreement with the observed splitting. The calculated lengths of the orbits appear in the plot as vertical bars above the peaks. The horizontal orbit length is marked with a longer bar. The lengths of all the orbits in units of the radius of curvature appear in Table. 8.2 The presence of this splitting in the return spectrum is strong evidence in support of the claim that diffraction off the edges of the reflector supports other closed orbits, which lead to resonances in the transmission spectra. Note that for the long orbits, the diffractive peaks are even stronger than the peaks from the geometric orbit. This is because the number of diffractive orbits increases linearly with the length of the orbit, whereas there is always only one geometric orbit, regardless of length.

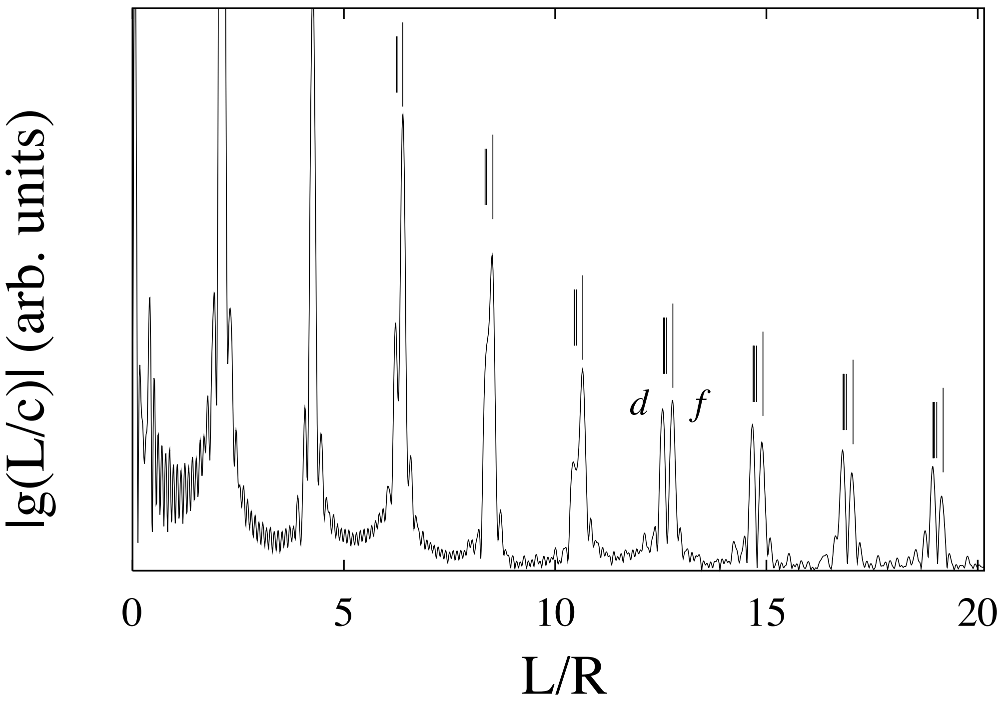

Figure 8.21: Experimental return spectra for the unstable regime. Time has been converted to the ratio L/R, where L is the length of the orbit. The splitting of the peaks clearly demonstrates the influence of both Fabry-Perot type orbits (marked f) and diffractive orbits (marked d), which are slightly shorter. The calculated lengths of the orbits are shown by vertical bars; short bars for the diffractive orbits, and longer bars for the horizontal orbit. For these plots the opening angle was 115°, and the reflector/wall separation was 32.5 cm.

Lengths of diffractive orbits							
N	N_1	N_2	L_1	L_2	L_{tot}	L_{hor}	Δ
2	1	1	1.03658	1.03658	2.07316	2.13114	0.0580
4	3	1	3.12029	1.03658	4.15687	4.26228	0.1054
6	3	3	3.12029	3.12029	6.24058	6.39342	0.1528
	5	1	5.22441	1.03658	6.26099		0.1324
8	5	3	5.22441	3.12029	8.34470	8.52456	0.1799
	7	1	7.34315	1.03658	8.37973		0.1448
10	5	5	5.22441	5.22441	10.4488	10.6557	0.2069
	7	3	7.34315	3.12029	10.4634		0.1923
	9	1	9.47048	1.03658	10.5071		0.1486
12	7	5	7.34135	5.22441	12.5677	12.7868	0.2193
	9	3	9.47048	3.12029	12.5908		0.1961
	11	1	11.6009	1.03658	12.6375		0.1494
14	7	7	7.34315	7.34315	14.6863	14.9180	0.2317
	9	5	9.47048	5.22441	14.6949		0.2231
	11	3	11.6009	3.12029	14.7212		0.1968
	13	1	13.7309	1.03658	14.7675		0.1505
16	9	7	9.47048	7.34315	16.8136	17.0491	0.2355
	11	5	11.6009	5.22441	16.8253		0.2238
	13	3	13.7309	3.12029	16.8512		0.1979
	15	1	15.8622	1.03658	16.8988		0.1503
18	9	9	9.47048	9.47048	18.9410	19.1803	0.2393
	11	7	11.6009	7.34315	18.9441		0.2362
	13	5	13.7309	5.22441	18.9553		0.2250
	15	3	15.8622	3.12029	18.9825		0.1978
	17	1	17.9946	1.03658	19.0312		0.1491
20	11	9	11.6009	9.47048	21.0714	21.3114	0.2400
	13	7	13.7309	7.34315	21.0741		0.2373
	15	5	15.8622	5.22441	21.0866		0.2248
	17	3	17.9946	3.12029	21.1149		0.1965
	19	1	20.1231	1.03658	21.1597		0.1517
22	11	11	11.6009	11.6009	23.3018	23.4425	0.2407
	13	9	13.7309	9.47048	23.2014		0.2411
	15	7	15.8622	7.34315	23.2054		0.2371
	17	5	17.9946	5.22441	23.2190		0.2235
	19	3	20.1231	3.12029	23.2434		0.1991
	21	1	22.2548	1.03658	23.2914		0.1511

Table 8.2: Lengths of the diffractive orbits. The columns are: N = number of half-bounces in orbit; N_1 = number of half-bounces in first leg; N_2 = number of half-bounces of second leg; L_1 = length of first leg; L_2 = length of second leg; $L_{\text{tot}} = L_1 + L_2$; L_{hor} = length of horizontal orbit; $\Delta = L_{\text{hor}} - L_{\text{tot}}$. The configuration of the resonator for this data was $D = 1.0656R, \alpha = 115°$. All numbers are given in terms of the radius of curvature of the reflector, which is taken to be unity.

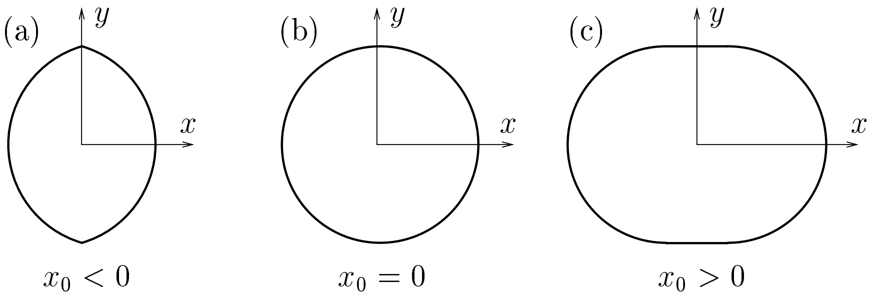

Figure 8.22: The lemon (a), circle (b), and stadium (c) billiards. We are interested only in states of these billiards which are even about x, and odd about y.

8.9 The avoided crossing

We now turn our attention to the avoided crossing that appears in Fig. 8.7 near $(D - R)/R = 0$. We have mentioned earlier that the level repulsion at this point is in part mediated by diffraction. In the interest of showing this, we solved for the energies and eigenstates of three closed systems that are closely related to our resonator: the lemon, circle, and stadium billiards, each shown in Fig. 8.22. In these closed systems, there are no sharp corners so we expect diffraction to play a minor role in the energies and wavefunctions[3].

The lemon billiard is made up of two circular walls of the same radius of curvature, placed so that the center of curvature of each wall is on the opposite side of the y-axis from the wall associated with it. The shape of the billiard is determined by the parameter x_0, which describes how far away the center of curvature of one wall is from the y-axis, in units where the radius of curvature is unity. We take this parameter to be negative since the center of curvature is on the opposite side of the y-axis when referred back to its associated curved wall. A value $x_0 = 0$ corresponds to the center of curvature being in the center of the billiard, i.e., a circle, as shown in Fig. 8.22(b). As x_0 is further increased to $x_0 > 0$, we form the stadium billiard, formed out of two semicircular walls joined by straight lines, as shown in Fig. 8.22(c).

The similarity between these closed systems and our resonator is especially great in the stable regime. In this regime, the states of the resonator are essentially the same as the states of the lemon billiard that are even about the x-axis, and odd about the y-

---

[3] Strictly speaking, there *is* diffraction in the lemon and stadium billiards, although it is of a completely different nature than in the corresponding open system. In the lemon billiard, it occurs at the point where the two arcs meet. In the stadium, it occurs at the point where the arcs meet the straight wall sections. Here it is a higher order effect, because only the second derivative of the boundary is discontinuous at that point, whereas the slope is continuous.

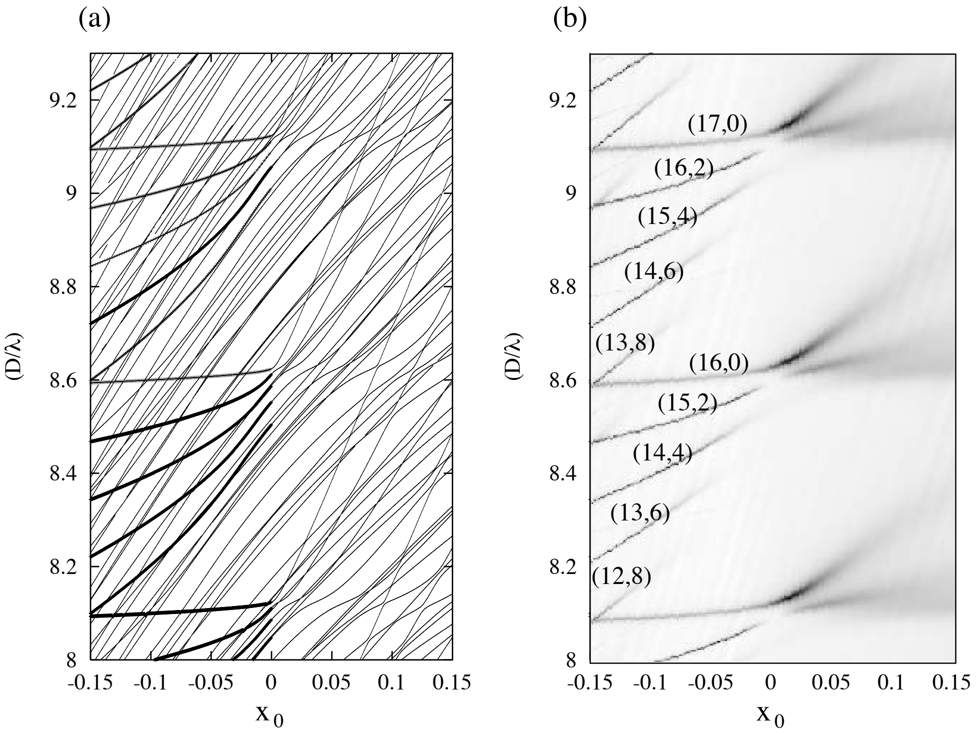

Figure 8.23: On the left, the states of a closed billiard are shown, as the parameter x_0 is swept. For $x_0 < 0$, the billiard is a lemon billiard; for $x_0 = 0$, it is a circle; for $x_0 > 0$ it is a stadium. For $x_0 < 0$, we have darkened the lines corresponding to the allowed states of the corresponding open system (see Fig. 8.24 for the corresponding eigenfunctions). On the right, the experimental transmission spectra for the open system are shown for the same parameter range. Note the similarity of the figures in the range $x_0 < 0$, where the open system exhibits stable classical dynamics.

axis. Here we imagine that the straight wall in the resonator corresponds to the y-axis, thus enforcing a node there, and the reflector corresponds to the curved right wall of the lemon billiard. We are only interested in the states even about the x-axis because of the symmetric position of the antenna in our resonator. As the reflector position is varied, we correspondingly change the parameter $x_0 < 0$ of the lemon billiard, and compare the states of each system. In the experiment, we see an avoided crossing at x_0. To investigate this, we can follow the states of the lemon/stadium billiard, as the parameter x_0 is swept slowly through zero.

In Fig. 8.23(a) we plot the (even-about-x, odd-about-y) levels of the lemon/stadium billiard as a function of the parameter $x_0 = (D - R)/R$ and wavelength. On the right, the corresponding experimental transmission spectra for the open system are shown. Notice the exact matching of the transmission peaks with the lemon billiard states in the stable regime. This excellent agreement is an artifact of the fact that, while our resonator is a geometrically *open* system, it is classically *closed*, in the sense that almost all trajectories beginning at the QPC that hit the reflector are doomed to forever remain in the region between the wall and the reflector. We only begin to notice the "openness" of our resonator for the peaks corresponding to large numbers of angular nodes. As we shall see, such states have a large angular spread, and it grows with decreasing x_0, so that eventually the caustics of the classical orbits supporting these states touch the tip of the reflector. When this happens, the states broaden and disappear. For example, this is apparent for the peak with quantum numbers (13,8) at around $x_0 = -0.1$. The wavefunction corresponding to this peak has 13 radial nodes between the y-axis and the reflector, and 8 angular nodes. The states with fewer angular nodes do not have such a wide angular extent, and therefore they do not disappear from the spectra until the reflector is farther from the wall.

It is apparent that there are many states in the closed lemon billiard that do not appear at all in the analogous open system. All such states have considerable amplitude near the corners of the lemon billiard – therefore they cannot exist in the corresponding open system. This is why they are absent in the experimental transmission spectra.

At $x_0 = 0$, there is an avoided crossing in both the open and closed systems. However, we see that the level repulsion is stronger in the open system. For example, observe the level repulsion of the states (17,0) and (16,2). The distance of closest approach of these two levels is four times greater in the open system compared to the closed system. For the open system, we judge the distance between the "levels" as the distance between the peak maxima. Now, the major difference between the two systems as far as the eigenstates are concerned is the presence of diffractive orbits in the open case. Therefore, we say that the avoided crossing is in large part mediated by *diffraction* in the open system.

For $x_0 > 0$, the correspondence between the open and closed systems comes to a somewhat abrupt halt. This is apparent in Fig. 8.23. The reason for this is as follows. In the open system, nearly all trajectories leave the system after a relatively small number of bounces. Therefore, even if we are looking at *long* periodic orbits, there are relatively few orbits that are of importance in determining a particular resonance. However, in the closed system, the number of periodic orbits necessary to build a particular state is much greater, and most will be of a completely different character than those of the open system. Therefore, we cannot expect that a state in the unstable closed system will have anything to do with a state in the unstable open system. Below, we will estimate the range of x_0 for which we expect there to be correspondence between the open and closed systems in the unstable regime.

The reason for the large number of orbits involved in a particular state for the closed system is as follows. In order to resolve a state semiclassically, one must follow trajectories for a time t_H, which is inversely proportional to the mean level spacing. This time is known as the Heisenberg time. To leading order in E, the density of states is a constant function with respect to the energy, given by Weyl's theorem [19],

$$\rho(E) = \frac{A}{2\pi}, \tag{8.17}$$

where A is the area of the (2D) billiard. Therefore, t_H will be a constant as a function of energy. Now, at low energies, the particle is moving slowly, so that in time t_H it has not moved very far. This means that only a small number of periodic orbits must be kept in order to build the state semiclassically. For higher energies, however, the particle is moving faster, so that a given trajectory could bounce many times off the walls of the billiard in a time $t = t_H$. Therefore one must include periodic orbits of increasing length to get reasonable semiclassical results as the energy increases. This is true for a closed system. If the system is open, however, this problem is not encountered, because only a very small fraction of the long orbits remain in the system up to the time t_H.

The necessity of following long orbits has important consequences for the semiclassical analysis of a classically chaotic system. In a chaotic system, it is well known that the number of periodic orbits increases exponentially with the length of the orbit. This means that it becomes exponentially harder to do semiclassical analysis of chaotic systems as the energy increases, because it involves a sum over an exponentially increasing number of periodic orbits.

Using the 2D density of states, we can estimate the range of x_0 for which we may expect rough correspondence between the eigenstates of the closed system with the resonances of the open system in the unstable regime. There is another characteristic time, t_λ, which we will call the Lyapunov time, which is the characteristic time that it takes for a trajectory to "fall off" a particular unstable periodic orbit. This time is,

$$t_\lambda = \frac{L}{k\lambda_{\mathrm{Lyap}}}, \tag{8.18}$$

where L is the length of the periodic orbit, λ_{Lyap} is the Lyapunov exponent of the orbit, and k is the wavenumber (L/k is the period of the orbit). We will focus on the horizontal orbit, for the case where the system is just barely unstable, so that $L \approx 2R$. The Lyapunov exponent for the horizontal orbit is given by the logarithm of the largest eigenvalue of the monodromy matrix, linearized about the horizontal orbit [11],

$$M = \begin{pmatrix} 1+2x_0 & 2x_0(1+x_0) \\ 2 & 1+2x_0 \end{pmatrix}. \tag{8.19}$$

The largest eigenvalue of this matrix is given by,

$$\begin{aligned} m_+ &= 1+2x_0+2\sqrt{x_0(1+x_0)} \\ &\approx 1+2\sqrt{x_0}, \end{aligned} \tag{8.20}$$

for small x_0. Thus the Lyapunov exponent is,

$$\begin{aligned} \lambda_{\mathrm{Lyap}} &\approx \ln(1+2\sqrt{x_0}) \\ &\approx 2\sqrt{x_0}. \end{aligned}$$

Therefore, the Lyapunov time for the horizontal orbit is approximately,

$$t_\lambda \approx \frac{R}{k\sqrt{x_0}}. \tag{8.21}$$

This must be compared with the Heisenberg time, which is $t_H = A/2\pi = R^2/8$ (the effective area of the billiard is $A = \pi R^2/4$ because of symmetry – we only take one quarter of the area of a full circle). We expect the correspondence between the open and closed systems to break down when these times are of the same order. That is, we look for the value of x_0 for which we have equality:

$$\frac{R^2}{8} = \frac{R}{k\sqrt{x_0}}, \tag{8.22}$$

or,

$$x_0 = \left(\frac{8}{kR}\right)^2. \tag{8.23}$$

Now, in our energy range we have approximately 9 wavelengths across one radius of the circle: $kR = 18\pi$. Thus we have for the value of x_0 at which correspondence ceases to hold,

$$x_0 = \left(\frac{8}{18\pi}\right)^2 \approx 0.02 \ll \frac{\lambda}{R}. \tag{8.24}$$

As indicated, this value of x_0 is much less than a wavelength, scaled to the radius of the billiard. This means that the states of the closed billiard already have mixed through a number of avoided crossings by the time the circle has been “stretched” by one wavelength. This is apparent from Fig. 8.23: we see that the first avoided crossings are happening already near $x_0 = 0.02$, corresponding to our rough estimate.

A sampling of states for the closed system of the lemon/stadium billiard are shown in Fig. 8.24. In this figure, the states corresponding to the series of quantum numbers $(17, 0) \rightarrow (13, 8)$ are shown, as the transition from a lemon to a stadium is made. The corresponding values of $k = \sqrt{2E}$ for each state shown are given in Table 8.3. For each column, the value of x_0 is given at the top of the column. We see that for the lemon billiard states, their angular extent increases with the number of angular nodes, as claimed previously. As x_0 approaches zero, the angular extent of each state is fully developed and covers the entire billiard, as is required by the rotational symmetry of the circle billiard states. The transition from the first to the second column is *diabatic*, that is, from left to right we track the states with the same character.

In the third column, we have plotted the states after x_0 has been *adiabatically* increased to the small value $x_0 = 0.02$, such that they still bear some resemblance to the states of the circle. This parameter value was chosen to be just before the first avoided crossing in the closed system, in accordance with the discussion above. This effectively means that the periodic orbits are not too different from those of a circle billiard, i.e. the periodic orbits are only weakly unstable. This means that one may still draw analogies between the closed and open systems in this regime, although the character of a particular resonance in the open system may be shared by several states in the corresponding closed system. For example, note that the first two states in the third column have angular lobes which are qualitatively similar to the diffractive state shown in Fig. 8.6. On the other hand, the third and fourth states in that column have amplitude running from the center out along the x-axis, qualitatively similar to the Fabry-Perot type state in Fig. 8.6. There is even the appearance of a focus just to the right and left of the center of the billiard in these two states, analogous to the focus seen in the Fabry-Perot state for the open system.

In the last column, we plot the five wave functions after the parameter x_0 has been adiabatically increased to $x_0 = 0.2$, or 20% of the radius of curvature. Now we see that the states no longer have anything to do with the states of the open system, exactly for the reasons given above.

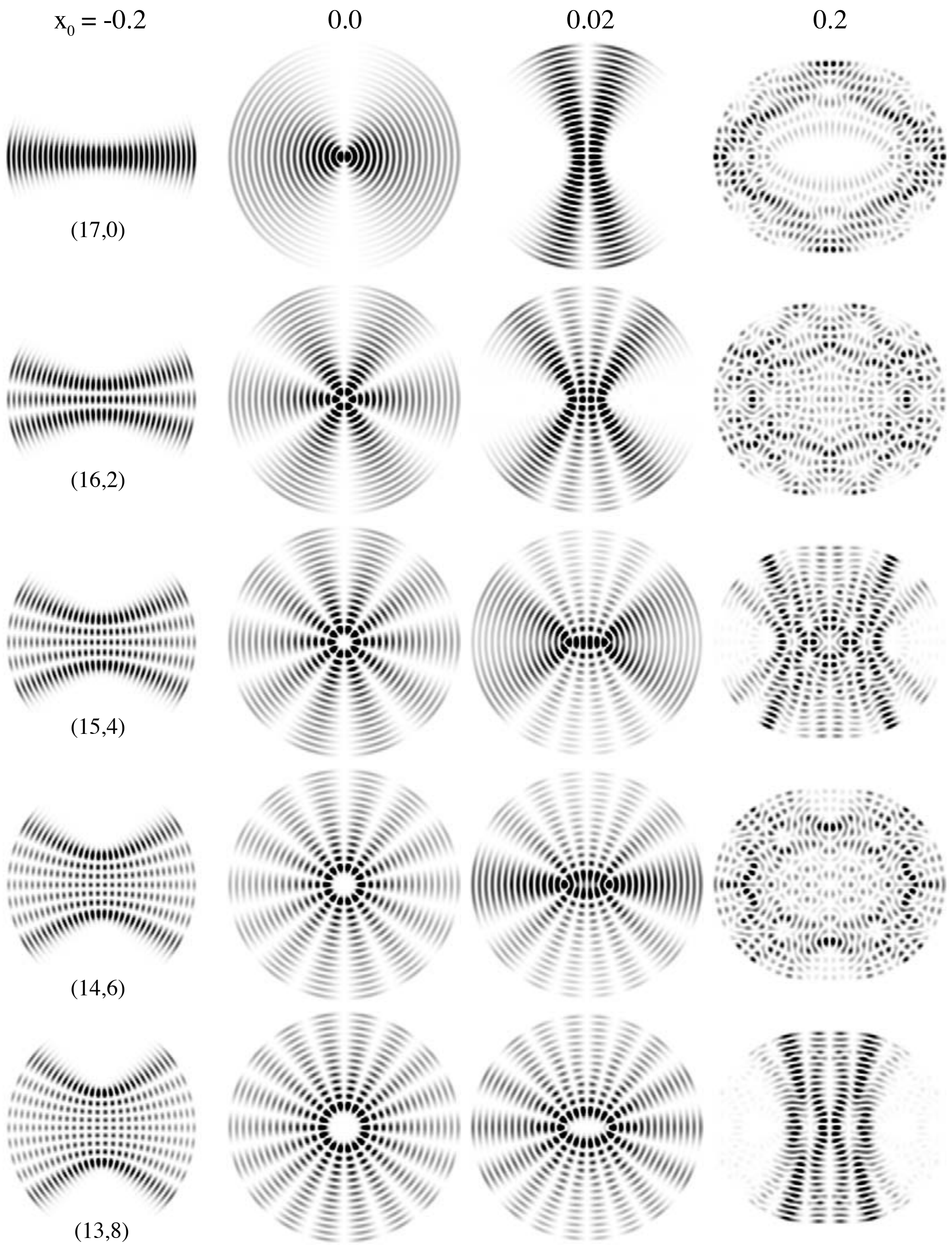

Figure 8.24: Eigenfunctions of the lemon/stadium billiard. On the top line is shown the parameter x_0, which describes how far the billiard is from a circle. On the left, we show some lemon billiard eigenfunctions, together with their quantum numbers. To the right, we show the eigenfunctions associated with each lemon state, as the parameter x_0 is varied adiabatically to $x_0 = 0, 0.02, 0.2$.

Eigenstates of the closed system		
x_0	(n,m)	$k=\sqrt{2E}$
-0.2	(17,0)	71.3806
-0.2	(16,2)	70.2283
-0.2	(15,4)	69.0855
-0.2	(14,6)	67.9527
-0.2	(13,8)	66.8308
0.0	(17,0)	57.3275
0.0	(16,2)	57.2577
0.0	(15,4)	57.1173
0.0	(14,6)	56.9052
0.0	(13,8)	56.6196
0.02	(17,0)	56.8273
0.02	(16,2)	56.4768
0.02	(15,4)	56.2240
0.02	(14,6)	56.1205
0.02	(13,8)	55.8705
0.2	“(17,0)”	51.8407
0.2	“(16,2)”	51.6105
0.2	“(15,4)”	51.3391
0.2	“(14,6)”	50.2602
0.2	“(13,8)”	50.7444

Table 8.3: Eigenvalues $k = \sqrt{2E}$ for each state shown in Fig. 8.24. The quantum numbers in the second column are only good in the regular regimes when x_0 is negative or a small positive number. In the stadium regime, the classical dynamics is chaotic and there are no longer any good quantum numbers; hence the quotations around the quantum numbers for $x_0 = 0.2$. The quantum numbers are only given there so that the connection may be made for each state to its adiabatic ancestor for smaller values of x_0. Note also that in the quantum numbering system, we do not count the angular node along the y-axis. This is to keep the analogy with the open system, where that node trivial as it is forced by the position of the wall.

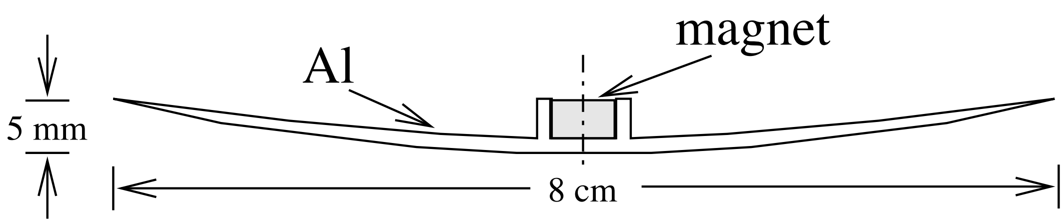

Figure 8.25: A cross section down a diameter of the coarse probe used for measuring the microwave field. It has cylindrical symmetry about the center axis.

8.10 Imaging wavefunctions with a coarse probe

The viability of measuring pure state wavefunctions in the context of microwave billiard systems has been demonstrated by many authors [17, 41, 42, 43]. However, the imaging of a pure state wavefunction in a *real* quantum system has not yet been achieved. We believe a technique similar to the method used here could be applied in clean mesoscopic systems to obtain images of pure state two dimensional wavefunctions in a 2DEG. In such systems, the fermi wavelength λ of the electrons is on the order of 50 Å. In analogy to the steel ball used in the microwave experiments, an AFM tip held close to the surface of the heterostructure could serve as a perturbation to measure the frequency shifts. However, the perturbation due to a nearby AFM tip on the electron wavefunction is a smooth potential disturbance 50-100 Å in size, comparable or greater than λ. One might expect that it would be difficult to measure the nodal lines of a wavefunction with such a coarse probe. To investigate this problem, we tried measuring a microwave mode with a coarse probe. Instead of a small steel ball, we used a probe 8 cm in size, corresponding to 1.5 wavelengths. The probe is shown in Fig. 8.25. It was formed by a "chord" of a sphere. The probe could be moved around the upper surface of the top plate of the cavity by means of an external magnet, in a manner similar to the steel ball perturbation.

The results of a wavefunction measurement of the peak *d1* with the coarse probe are displayed in Fig. 8.26. Only half of the wavefunction was measured. For comparison, the same state measured with the 4 mm ball is shown as well. Note that far from the QPC, the nodal lines in the two measurements match very well. For the coarse measurement, data near the wall and mirror were unavailable because of the large size of the probe. The level of detail obtained with the coarse probe is surprising, considering that it was over *three* wavefunction maxima in diameter. This result indicates that it should be possible to

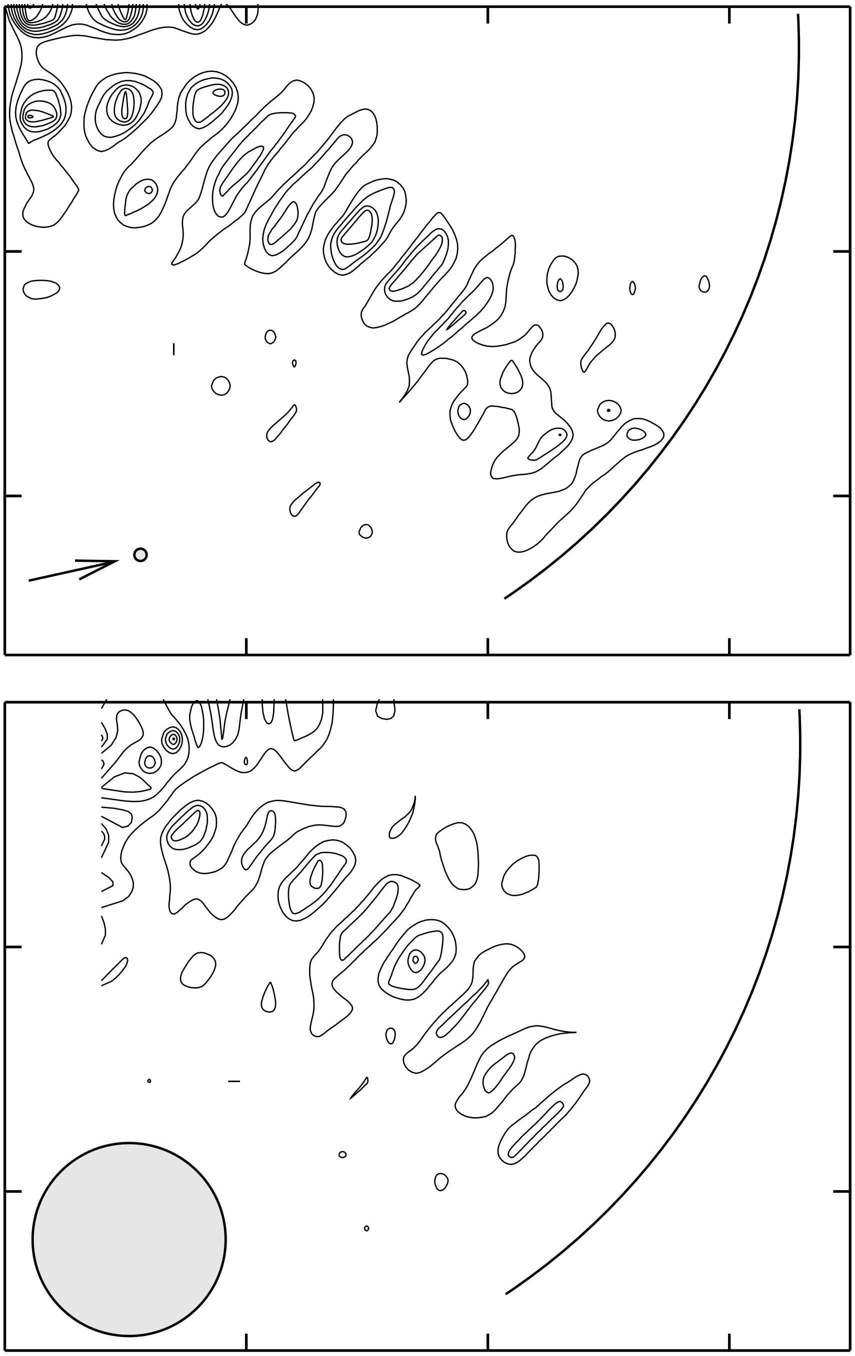

Figure 8.26: A comparison between fine and coarse measurement probes. The sizes of the probes are indicated by circles in the lower left corner of each graph. In the upper plot, an arrow marks the probe. The tics on all axes are 10 cm apart.

directly image an pure state electron wavefunction in a 2DEG.

8.11 Conclusion

In summary, we have demonstrated the existence of diffractive orbits in an open microwave billiard, which give rise to resonances and wavefunctions that would not be predicted by a simple semiclassical theory. Such orbits are of importance in open, unstable systems where the number of unstable classical periodic orbits is small. In such systems, diffraction can play a major role in determining the spectrum of the system. Further, we have shown that it may be possible to measure the pure state wavefunction of an elecctron in a 2DEG, by using a a coarse AFM tip as a probe.

I am grateful to the Hewlett Packard Corporation for the loan of a network analyzer that was used in these experiments.

Appendix A

The Kirchoff approximation

In this appendix we illustrate the method of the Kirchoff approximation by the example of scattering on an infinite half-line in 2D. The essence of the Kirchoff approximation lies in assuming that the wave scattered by the obstacle is made up of a continuous distribution of point sources located along the line. The amplitude of the sources is determined by first solving the problem of the infinite line, subject to the condition that there be a perfect shadow on the dark side of the line, and a perfect standing wave on the illuminated side. We will take our incident wave as incident from the left: a traveling plane wave of the form e^{ikx}. For the case of the infinite line, the obstruction will be located on $\{x = 0, -\infty < y < \infty\}$. For the half-line, $\{x = 0, -\infty < y < 0\}$.

The Kirchoff approximation states that the solution to infinite line problem is,

$$\psi(\boldsymbol{r}) = e^{ikx} + C \int_{-\infty}^{\infty} H_0^{(1)}(k|\boldsymbol{r} - s\hat{\boldsymbol{y}}|)\ ds. \tag{A.1}$$

For the half-line, the solution is,

$$\psi(\boldsymbol{r}) = e^{ikx} + C \int_{-\infty}^{0} H_0^{(1)}(k|\boldsymbol{r} - s\hat{\boldsymbol{y}}|)\ ds. \tag{A.2}$$

To find the constant C, we evaluate Eq. A.1 by stationary phase, and require that the solution be zero for $x > 0$. In particular, many wavelengths from the wall the solution must also be zero, so we are justified in replacing the Hankel function with its asymtotic value. Furthermore, since there is translational symmetry along y for the infinite line, the argument of the Hankel function may be replaced by,

$$|\boldsymbol{r} - s\hat{\boldsymbol{y}}| = \sqrt{x^2 + s^2}. \tag{A.3}$$

With these substitutions, Eq. A.1 becomes,

$$\psi(\boldsymbol{r}) = e^{ikx} + Ce^{-i\pi/4}\sqrt{\frac{2}{\pi k}}\int_{-\infty}^{\infty} \frac{e^{ik\sqrt{x^2+s^2}}}{(x^2+s^2)^{1/4}}\, ds. \tag{A.4}$$

The integral can be evaluated by stationary phase. This states,

$$\int_{-\infty}^{\infty} f(x)e^{i\phi(x)} \approx \sum_i f(x_i)\sqrt{\frac{-2\pi}{i\phi''(x_i)}}e^{i\phi(x_i)}, \tag{A.5}$$

where x_i are the points where $\phi'(x) = 0$. In our case, $\phi(s) = k\sqrt{x^2+s^2}$, which is stationary at $s = 0$. Thus we find,

$$\int_{-\infty}^{\infty} \frac{e^{ik\sqrt{x^2+s^2}}}{(x^2+s^2)^{1/4}}\, ds \approx \sqrt{\frac{-2\pi}{ik}}e^{ikx}. \tag{A.6}$$

Using this value for the integral, Eq. A.4 becomes,

$$\psi(\boldsymbol{r}) = e^{ikx} + \frac{2}{k}Ce^{ikx}, \tag{A.7}$$

so that if the solution is to be zero on the right hand side, we must require that,

$$C = -\frac{k}{2}. \tag{A.8}$$

Now, to solve the half-line problem within the Kirchoff approximation, we use the above value for C in Eq. A.2. The true solution would allow for some dependence on s of the "constant" $C \to C(s)$. Neglecting this dependence by assuming that the amplitudes for sources in the half-line case are everywhere the same as for the full line is the approximation made by Kirchoff. We have then for the half-line,

$$\psi(x,y) = e^{ikx} - \sqrt{\frac{k}{2\pi i}}\int_{-\infty}^{0} \frac{e^{ik\sqrt{x^2+(y-s)^2}}}{(x^2+(y-s)^2)^{1/4}}\, ds. \tag{A.9}$$

This integral cannot be evaluated by stationary phase because its upper limit is cut off at zero. In fact, the abrupt cutoff of this oscillatory integral is one way of viewing diffraction: since the integral is highly oscillatory, contributions from a particular point s will be cancelled by a nearby point $s + \delta s$. Near the endpoint $s = 0$, there will be contributions which would have otherwise been cancelled by points at $s > 0$. However, these contributions will not be cancelled, because the integral is abruptly cut off at $s = 0$. Thus we see that diffraction arises from a small region of sources in the integral near the tip. This region will be of the order of a wavelength in size.

Because the integral in Eq. A.9 cannot be evaluated by stationary phase, it must be computed numerically. Therefore, we cannot take the lower limit to $-\infty$ in practice, and it must be cut off at some large value of s. However, this arbitrary cutoff will produce unwanted contributions in much the same way as that near $s = 0$. Therefore, we multiply the integrand by a gentle Gaussian in s, so that the rapid oscillations are killed off and we may then safely cut off the integral at large s, as long as the cutoff point is far into the tail of the Gaussian. Our solution thus reads,

$$\psi(x,y) = e^{ikx} - \sqrt{\frac{k}{2\pi i}} \int_{-\alpha}^{0} \frac{e^{ik\sqrt{x^2+(y-s)^2}} e^{-s^2/\beta^2}}{(x^2+(y-s)^2)^{1/4}}\, ds, \tag{A.10}$$

where β is a large number such that $k\beta \gg 1$, and the lower limit $\alpha \gg \beta$, such that integrand is negligible at the point where the integral is cut off at the lower limit.

The function in Eq. A.10 is shown in Fig. 8.11. We see that the result is in good agreement with both the exact result and the prediction of the uniform geometric theory of diffraction presented in Chapter 8.

Appendix B

Picture Gallery

In this appendix, some interesting pictures which were borne out of the work in this thesis are presented.

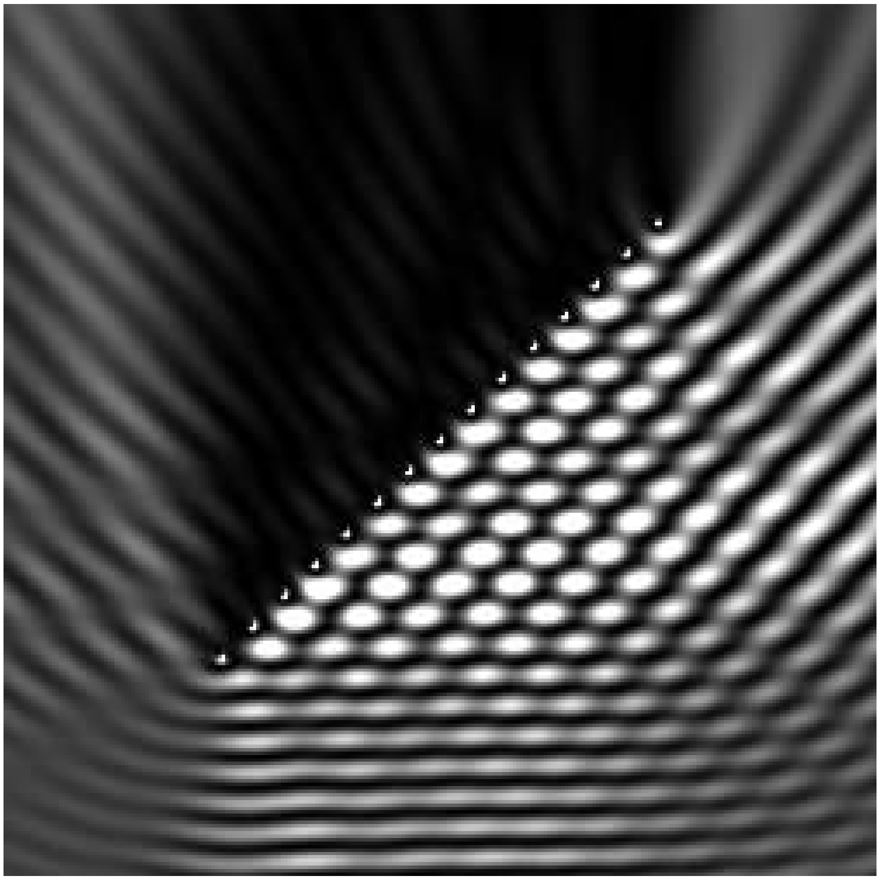

Figure B.1: Here we see a wave being scattered off a diagonal array of 15 hard disc scatterers in 2D. Both s- and p-waves are being scattered, using the method presented in Chapter 6. The wave is incident from below. The dimensions are: $ka = 1$, $kL = 45$, where a is the disc radius and L is length of the array. The array is behaving like a bumpy mirror, with a good shadow behind the mirror and a reflected wave to the right. The checkerboard standing wave pattern is due to interference between the incident and reflected wave. Regions of high probability are light.

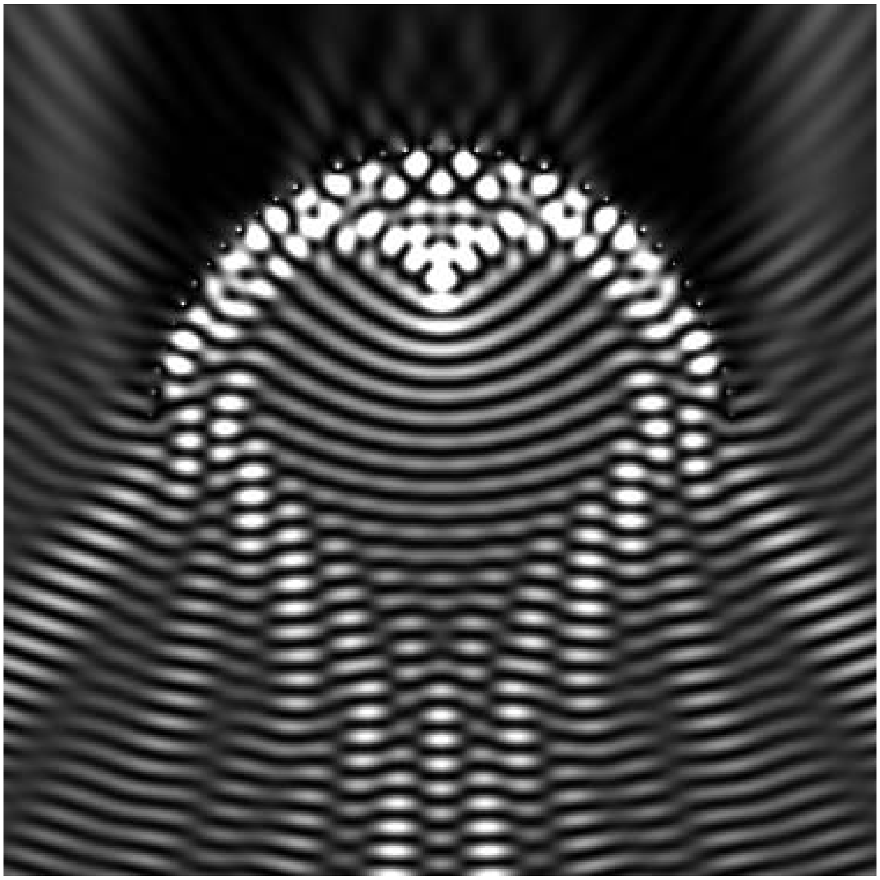

Figure B.2: Here a wave is scattered off a semicircular array of 40 hard disc s-wave scatterers in 2D. The wave is incident from below. The dimensions are: $ka = 1$, $kR = 40$, where a is the disc radius and R is the radius of the semicircle. Note the focus at half the radius of curvature of the semicircle, as predicted by geometrical optics for spherical mirrors.

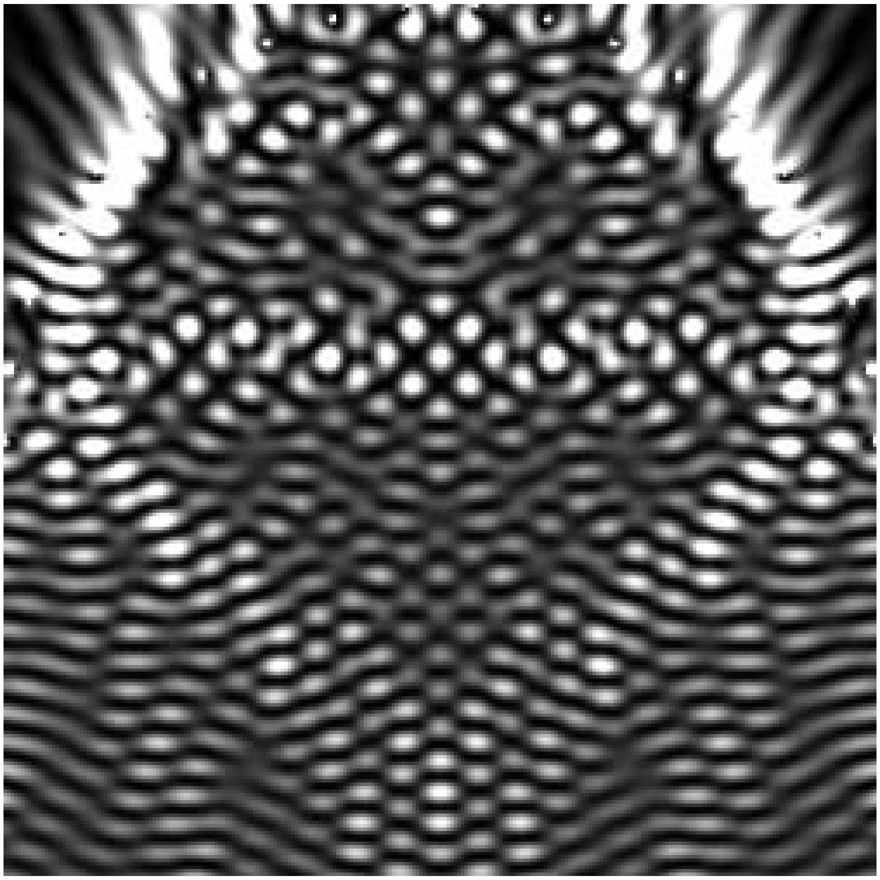

Figure B.3: Sometimes a wayward calculation turns out pretty.

Figure B.4: Here is a nicely scarred state of the stadium billiard. The unstable periodic orbit associated with the scar is an isosceles triangle with base parallel to the y-axis, and its mirror image.

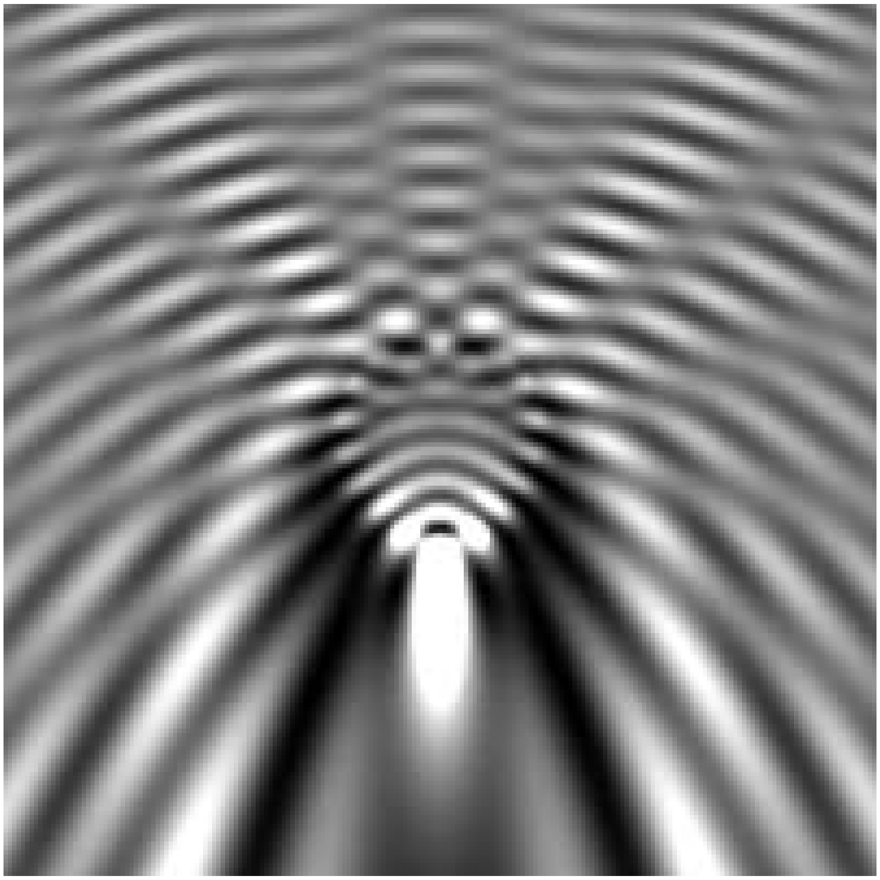

Figure B.5: This is an intensity plot of a light wave scattering off a thick lens which has in index of refraction $n = 1.34$. Notice the strong cylindrical aberration which causes the focus to be stretched out. An plane wave is incident from above.

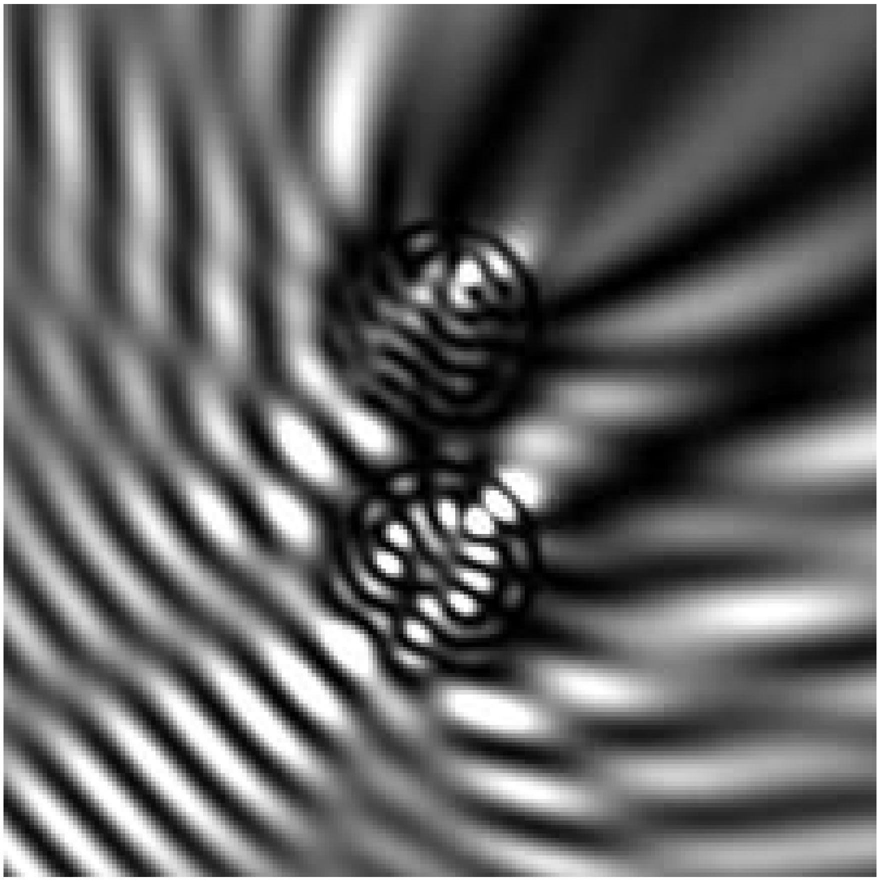

Figure B.6: This is an intensity plot of a light wave scattering off two thick lenses which has a higher index of refraction: $n = 2.24$. Now, the focus in the lower lens is actually *inside* the lens. An plane wave is incident from the lower left corner. The intensity in the upper lens is irregularly shaped because it is partly in the shadow of the lower lens. This picture was generated using the methods presented in Chapter 4.

Bibliography

[1] M. Abramowitz and I. A. Stegun, editors. *Handbook of Mathematical Functions.* Dover, London, 1965.

[2] S. K. Adhikari, A. Delfino, T. Frederico, I. D. Goldman, and L. Tomio. Efimov and Thomas effects and the model dependence of three-particle observables in two and three dimensions. *Physical Review A*, 37:3666, 1988.

[3] V. F. Agekyan, L. G. Gerchikov, and V. A Kharchenko. New mechanism of formation of discrete luminescence spectra of excitons localized at point defect clusters. *Soviet Physics JETP*, 65:5, 1987.

[4] S. Albeverio, F. Geszetsky, R. Høegh-Krohn, and H. Holden. *Solvable models in quantum mechanics.* Springer-Verlag, Berlin, 1988.

[5] B. H. Bransden and C. J. Joachain. *Introduction to Quantum Mechanics.* Longman Scientific and Technical, Essex, England, 1989.

[6] S. Chan and E. J. Heller. Stm surface state electron scattering: two-tip results from one tip data. *Physical Review Letters*, 78:2570, 1997.

[7] C. Cohen-Tannoudji, B. Diu, and F. Laloë. *Quantum Mechanics.* Wiley, New York, 1977.

[8] Yu. N. Demkov and V. N. Ostrovskii. *Zero-range Potentials and their Applications in Atomic Physics.* Plenum Press, New York, 1988.

[9] R. H. Dicke. Coherence in spontaneous radiation processes. *Physical Review*, 93:99, 1954.

[10] G. Drukarev. The zero-range potential model and its application in atomic and molecular physics. *Advances in Quantum Chemistry*, 11:251, 1978.

[11] J. D. Edwards. *Wavelet analysis of two dimensional quantum scattering.* PhD thesis, Harvard University, 1998.

[12] V. Efimov. Energy levels arising from resonant two-body forces in a three body system. *Physics Letters*, 33B:563, 1970.

[13] V. Efimov. Energy levels of three resonantly interacting particles. *Nuc. Phys.*, A210:157, 1973.

[14] C. Feuillade. Scattering from collective modes of air bubbles in water and the physical mechanism of superresonances. *Journal of the Acoustical Society of America*, 98:1178, 1995.

[15] D. G. Fried, T. C. Killian, L. Willmann, D. Landhuis, S. C. Moss, D. Kleppner, and T. J. Greytak. Bose einstein condensation of atomic hydrogen. *Physical Review Letters*, 81:3811, 1998.

[16] J. E. Goell. A circular harmonic computer analysis of rectangular dielectric waveguides. *Bell Systems Technichal Journal*, 48:2133, 1969.

[17] S. Gokirmak, D. H. Wu, J. S. A. Bridgewater, and S. M. Anlage. Scanned perturbation technique for imaging electromagnetic standing wave patterns of microwave cavities. *Review of Scientific Instruments*, 69:3410, 1998.

[18] G. H. Golub and C. F. Van Loan. *Matrix Computations.* Johns Hopkins University Press, Baltimore, 1996.

[19] M. C. Gutzwiller. *Chaos in Classical and Quantum Mechanics.* Springer-Verlag, Berlin, 1990.

[20] E. J. Heller. Quantum proximity resonances. *Physical Review Letters*, 77:4122, 1996.

[21] J. S. Hersch and E. J. Heller. Observation of proximity resonances in a parallel-plate waveguide. *Physical Review Letters*, 81:3059, 1998.

[22] K. Huang. *Statistical Mechanics.* Wiley, New York, 1987.

[23] J. D. Jackson. *Classical Electrodynamics.* Wiley, New York, 1975.

[24] G. L. James. *Geometrical theory of diffraction for electromagnetic waves.* Peregrinus, Stevenage, England, 1976.

[25] J. A. Katine, M. A. Eriksson, A. S. Adourian, R. M. Westervelt, J. D. Edwards, A. S. Lupu-Sax, E. J. Heller, K. L. Campman, and A. C. Gossard. Point contact conductance of an open resonator. *Physical Review Letters*, 79:4806, 1997.

[26] J. B. Keller. Geometrical theory of diffraction. *Journal of the Optical Society of America*, 52:116, 1962.

[27] R. G. Kouyoumjian and P. H. Pathak. A uniform geometrical theory of diffraction for an edge in a perfectly conducting surface. *Proceedings of the IEEE*, 62:1448, 1974.

[28] L. D. Landau and E. M. Lifshitz. *Quantum Mechanics.* Pergamon Press, Elmsford, NY, 3rd edition, 1977.

[29] T. K. Lim and P. A. Maurone. Nonexistence of the Efimov effect in two dimensions. *Physical Review B*, 22:1467, 1980.

[30] L. C. Maier and J. C. Slater. Field strength measurements in resonant cavities. *Journal of Applied Physics*, 23:68, 1954.

[31] M. O. Mewes, M. R. Andrews, N. J. van Druten, D. M. Kurn, D. S. Durfee, and W. Ketterle. Bose einstein condensation in a tightly confining dc magnetic trap. *Physical Review Letters*, 77:416, 1996.

[32] P. M. Morse and H. Feshbach. *Methods of Theoretical Physics.* McGraw Hill, New York, 1953.

[33] M. Olshanii. Atomic scattering in the presence of an external confinement and a gas of impenetrable bosons. *Physical Review Letters*, 81:938, August 1998.

[34] N. Pavloff and C. Schmit. Diffractive orbits in quantum billiards. *Physical Review Letters*, 75:61, 1995.

[35] W. H. Press, S. A. Teukolsky, W. T. Vetterling, and B. P. Flannery. *Numerical recipes in C: the art of scientific computing.* Cambridge University Press, New York, 1992.

[36] E. M. Purcell and C. R. Pennypacker. Scattering and absorption of light by nonspherical dielectric grains. *Astrophysical Journal*, 186:705, 1973.

[37] L. S. Rodberg and R. M. Thaler. *Introduction to the quantum theory of scattering.* Academic Press, Inc., New York, 1970.

[38] J. J. Sakurai. *Modern Quantum Mechanics.* Addison Wesley, 1st edition, 1985.

[39] M. Sieber, N. Pavloff, and C. Schmit. Uniform approximation for diffractive contributions to the trace formula in billiard systems. *Physical Review E*, 55:2279, 1997.

[40] S. Sridhar. Experimental observation of scarred eigenfunctions of chaotic microwave cavities. *Physical Review Letters*, 67:785, 1991.

[41] S. Sridhar, D. Hogenboom, and B. A. Willemsen. Microwave experiments on chaotic billiards. *Journal of Statistical Physics*, 68:239, 1992.

[42] J. Stein and H. J. Stöckmann. Experimental determination of billiard wave functions. *Physical Review Letters*, 68:2867, 1992.

[43] H. J. Stöckmann and J. Stein. Quantum chaos in billiards studied by microwave absorption. *Physical Review Letters*, 64:2215, 1990.

[44] R. Szmytkowski and C. Szmytkowski. Quantum proximity resonances. *Physics Letters A*, 235:217, 1997.

[45] L. H. Thomas. The interaction between a neutron and a proton and the structure of H^3. *Physical Review*, 47:903, 1935.

[46] H. C. van de Hulst. *Light Scattering by Small Particles.* Wiley, New York, 1957.

[47] G. Vattay, A. Wirzba, and P. E. Rosenqvist. Periodic orbit theory of diffraction. *Physical Review Letters*, 73:2304, 1994.

[48] R. M. Westervelt. private communication.